

ISSN en trámite



Geofísica Internacional

Revista Trimestral Publicada por el Instituto de Geofísica de la
Universidad Nacional Autónoma de México



México

Volume 55 Number 2
April - June
2016

— Geofísica Internacional —

Dr. Arturo Iglesias Mendoza
Director of Instituto de Geofísica

Dra. Xyoli Pérez Campos
President of Unión Geofísica Mexicana

Editor Chief

Dr. Servando De la Cruz-Reyna
Instituto de Geofísica, UNAM
sdelacrr@geofisica.unam.mx

Technical Editor

Mtra. Andrea Rostan Robledo
Instituto de Geofísica, UNAM
arostan@igeofisica.unam.mx

Editorial Board

Donald Bruce Dingwell
Earth and Environment
Ludwig Maximilian University of Munich,
Germany

Eric Desmond Barton
Departamento de Oceanografía
Instituto de Investigaciones Marinas, Spain

Jorge Clavero
Amawta Consultores, Chile

Gerhardt Jentzsch
Institut für Geowissenschaften
Friedrich-Schiller-Universität Jena, Germany

Peter Malischewsky
Institut für Geowissenschaften
Friedrich-Schiller-Universität Jena, Germany

François Michaud
Géosciences Azur
Université Pierre et Marie Curie, France

Olga Borisovna Popovicheva
Scobeltzine Institute of Nuclear Physics
Moscow State University, Rusia

Jaime Pous
Facultad de Geología
Universidad de Barcelona, Spain

Joaquín Rui
UA Science
University of Arizona, United States

Angelos Vourlidas
Solar Physics Branch
NASA Goddard Space Flight Center, United States

Théophile Ndougsa Mbarga
Department of Physics
University of Yaounde I, Cameroon

Associate Editors
José Agustín García Reynoso
Atmospheric Science Centro de Ciencias de la
Atmósfera UNAM, Mexico

Tereza Cavazos
Atmospheric Science
Departamento de Oceanografía Física CICESE,
Mexico

Dante Jaime Morán-Zenteno
Geochemistry
Instituto de Geología, UNAM, Mexico

Margarita López
Geochemistry
Instituto de Geología UNAM, Mexico

Avto Gogichaisvili
Geomagnetism And Paleomagnetism
Instituto de Geofísica UNAM, Mexico

Jaime Urrutia-Fucugauchi
Geomagnetism And Paleomagnetism
Instituto de Geofísica, UNAM, Mexico

Felipe I. Arreguín Cortés
Hydrology
Instituto Mexicano de Tecnología del Agua IMTA,
Mexico

William Lee Bandy
Marine Geology And Geophysics
Instituto de Geofísica UNAM, Mexico

Fabian García-Nocetti
Mathematical And Computational
Modeling
Instituto de Investigaciones en Matemáticas
Aplicadas y en Sistemas UNAM, Mexico

Graciela Herrera-Zamarrón
Mathematical Modeling
Instituto de Geofísica, UNAM, Mexico

Ismael Herrera Revilla
Mathematical And Computational
Modeling
Instituto de Geofísica UNAM, Mexico

Rene Chávez Segura
Near-Surface Geophysics
Instituto de Geofísica UNAM, Mexico

Juan García-Abdeslem
Near-Surface Geophysics
División de Ciencias de la Tierra CICESE, Mexico

Alec Torres-Freyermuth
Oceanography
Instituto de Ingeniería, UNAM, Mexico

Jorge Zavala Hidalgo
Oceanography
Centro de Ciencias de la Atmósfera UNAM,
Mexico

Shri Krishna Singh
Seismology
Instituto de Geofísica, UNAM, Mexico

Xyoli Pérez-Campos
Seismology
Servicio Sismológico Nacional, UNAM, Mexico

Blanca Mendoza Ortega
Space Physics
Centro de Ciencias de la Atmósfera, UNAM,
Mexico

Inez Staciari Batista
Space Physics
Pesquisador Senior Instituto Nacional de Pesquisas
Espaciais, Brazil

Roberto Carniel
Volcanology
Laboratorio di misure e trattamento dei segnali
DPIA - Università di Udine, Italy

Miguel Moctezuma-Flores
Satellite Geophysics
Facultad de Ingeniería, UNAM, Mexico

Assistance

Elizabeth Morales Hernández,
Management
eliedit@igeofisica.unam.mx



GEOFÍSICA INTERNACIONAL, Año 55, Vol. 55, Núm. 2, abril - junio de 2016 es una publicación trimestral, editada por la Universidad Nacional Autónoma de México, Ciudad Universitaria, Alcaldía Coyoacán, C.P. 04150, Ciudad de México, a través del Instituto de Geofísica, Circuito de la Investigación Científica s/n, Ciudad Universitaria, Alcaldía Coyoacán, C.P. 04150, Ciudad de México, Tel. (55)56 22 41 15. URL: <http://revistagi.geofisica.unam.mx>, correo electrónico: revistagi@igeofisica.unam.mx. Editora responsable: Andrea Rostan Robledo. Certificado de Reserva de Derechos al uso Exclusivo del Título: 04-2022-081610251200-102, ISSN: en trámite, otorgados por el Instituto Nacional del Derecho de Autor (INDAUTOR). Responsable de la última actualización Saúl Armendáriz Sánchez, Editor Técnico. Fecha de la última modificación: 31 de marzo 2016, Circuito de la Investigación Científica s/n, Ciudad Universitaria, Alcaldía Coyoacán, C.P. 04150, Ciudad de México.

El contenido de los artículos es responsabilidad de los autores y no refleja el punto de vista de los árbitros, del Editor o de la UNAM. Se autoriza la reproducción total o parcial de los textos siempre y cuando se cite la fuente completa y la dirección electrónica de la publicación.



Esta obra está bajo una Licencia Creative Commons Atribución-NoComercial-SinDerivadas 4.0 Internacional.

Contents

Relocation and seismotectonic interpretation of the seismic swarm of August - December of 2012 in the Linares area, northeastern Mexico.
Carmen M. Gómez-Arredondo, Juan C. Montalvo-Arrieta, Arturo Iglesias-Mendoza, Victor H. Espíndola-Castro

95

Geophysical modeling of the manganese deposit for Induced Polarization method in Itapira (Brazil).
Leandro B. Vieira, César A. Moreira, Ariane R. P. Côrtes, George L. Luvizotto

107

Comparative analyzes among electrical resistivity tomography arrays in the characterization of flow structure in free aquifer.
César Augusto Moreira, Marcelo Montenegro, Alan Carrara

119

Site Response of the NARS-Baja and RESBAN Broadband Networks of the Gulf of California, México.
Lenin Ávila-Barrientos, Raúl R. Castro

131

Relationship between the minima of the horizontal magnetic component measured in Mexico and the Dst and SYM-H indices for geomagnetic storms with $Dst \leq -100nT$ during the descending phase of solar cycle 23
Julia Lénica Martínez-Bretón, Blanca Mendoza Ortega, Esteban Hernández-Quintero

155

Relocation and seismotectonic interpretation of the seismic swarm of August – December of 2012 in the Linares area, northeastern Mexico

Carmen M. Gómez-Arredondo, Juan C. Montalvo-Arrieta*, Arturo Iglesias-Mendoza and Víctor H. Espíndola-Castro

Received: January 27, 2015; accepted: November 27, 2015; published on line: April 01, 2016

Resumen

En este trabajo relocalizamos 52 sismos en el rango de $2.5 \leq M_c \leq 3.6$ de una secuencia sísmica de más de 250 eventos que ocurrió al suroeste de la ciudad de Linares, N.L., durante los meses de julio – diciembre de 2012, en el noreste de México. Para estudiar este enjambre se instalaron cuatro estaciones sismológicas en la región de interés, las cuales operaron durante diferentes periodos entre septiembre y diciembre. La relocalización de la secuencia demostró que las profundidades hipocentrales fueron de $8 (\pm 5)$ km, y los residuales de los tiempos de arribo tuvieron valores ≤ 0.38 s. Se generaron soluciones del plano de falla para sismos individuales, así como a través de la técnica de mecanismos compuestos. La solución de los mecanismos focales encontrada corresponde con fallamiento inverso con rumbo NNW-SSE y buzamiento hacia el SW para el plano nodal inferido (rumbo $\sim 150^\circ$, buzamiento $\sim 50^\circ$ y ángulo de deslizamiento $\sim 67^\circ$), el cual revela que el esfuerzo horizontal máximo predomina en el área de estudio ($S_{Hmax} > S_{Hmin} > S_v$).

Palabras clave: Esfuerzo horizontal máximo, estado de fuerza actual, mecanismo focal, Sierra Madre Oriental, sismicidad intraplaca.

Abstract

We relocated 52 events of $2.5 \leq M_c \leq 3.6$ from a seismic sequence of over 250 events that occurred during July-December 2012 southwest of the Linares area, northeastern Mexico. To examine this swarm four seismic stations were installed in the region and operated during different time periods from September to December. Relocation of the swarm showed that the earthquake hypocentral depths were at $8 (\pm 5)$ km, and the time residuals had values ≤ 0.38 s. The fault plane solutions were generated for individual earthquakes and through the use of the composite mechanism technique. The focal mechanism solutions show pure reverse faulting; the SW dipping NNW – SSE trending nodal plane is the inferred fault plane (strike $\sim 150^\circ$, dip $\sim 50^\circ$ and rake $\sim 67^\circ$), which reveals that maximum horizontal stress ($S_{Hmax} > S_{Hmin} > S_v$) predominates in the area.

Palabras clave: Maximum horizontal stress, current stress field, focal mechanism, Sierra Madre Oriental, intraplate seismicity.

C. M. Gómez-Arredondo
Facultad de Ciencias de la Tierra
Universidad Autónoma de Nuevo León
Ex-Hacienda de Guadalupe km 8.
Carr. Linares, Cerro Prieto, 67700
Linares, N.L., México

J. C. Montalvo-Arrieta
Facultad de Ciencias de la Tierra
Universidad Autónoma de Nuevo León
Ex-Hacienda de Guadalupe km 8.
Carr. Linares, Cerro Prieto, 67700
Linares, N.L., México
Corresponding author: jmontalvoa87@gmail.com

A. Iglesias-Mendoza
Departamento de Sismología
Instituto de Geofísica
Universidad Nacional Autónoma de México
Circuito de la Investigación Científica s/n
Ciudad Universitaria, 04510
México, D.F.

V. H. Espíndola-Castro
Servicio Sismológico Nacional
Universidad Nacional Autónoma de México
Circuito de la Investigación Científica s/n
Ciudad Universitaria, 04510
México, D.F.

Introduction

In recent years, the increase of temporary and permanent seismic networks in the interior of continents has allowed the study of the deformation processes in stable continental regions. The recording data have been used to improve the accuracy in location, obtain focal mechanism, and determine the current stress fields. According to Zoback and Zoback (1980) knowing the pattern of the stress field and its variations are useful to understanding the tectonics of a region. Northeastern Mexico has had a complex geological history characterized by several tectonic events. These have produced the irregular morphology of the crust that has been revealed through gravity data (e.g., Mickus and Montana, 1999; Bartolini and Mickus, 2001). Intraplate seismicity can be correlated with pre-existing faults (e.g., associated with ancient suture zones) which are optimally-oriented for reactivation in the current stress field (Hurd and Zoback, 2012; Ramos-Zuñiga *et al.*, 2012a). Although large intraplate earthquakes are rare, these infrequent events can be extremely devastating because the cities in stable continental region are seismically poorly prepared. These earthquakes can also cause widespread damage because the attenuation of seismic energy is relatively low in plate interiors (Hanks and Johnston, 1992; Crone *et al.*, 2003; Montalvo-Arrieta *et al.*, 2015).

A seismic sequence occurred from July through December 2012, southwest of the city of Linares. This is the first sequence reported in northeastern Mexico since the installation of two permanent broadband seismological stations (LNIG in 2006; and MNIG in 2012) in the region by the Mexican National Seismological Service (Servicio Sismológico Nacional, SSN) in collaboration with the Facultad de Ciencias de la Tierra (FCT) of the Universidad Autónoma de Nuevo León (UANL). The SSN reported 85 earthquakes with $2.9 \leq M_c \leq 3.6$ during this time period. Some of these events were felt by inhabitants of small communities near the epicentral area. In this work we present an analysis of the earthquake sequence that occurred southwest of the Linares area, using a temporal broadband seismic network. This allowed us to relocate the seismic activity, obtain focal mechanisms, and provide a seismotectonic interpretation of the seismic clustering.

Tectonic setting

The morpho-tectonic features located in northeastern Mexico have been generated

by the results of several geological processes that occurred in the past. Moreover, the main tectonic events that have affected this area have been related to: (a) the separation of supercontinent Rodinia in Neoproterozoic-early Paleozoic (Torsvik, 2003) that generated the Iapetus Ocean in the southeast continental margin of North America (Stewart, 1988). (b) The collision of the Gondwana and Laurasia landmasses during the Paleozoic that shaped the Pangea Supercontinent (Sedlock *et al.*, 1993). (c) The split of Pangea that was initiated in late Triassic in Northeast Mexico (Goldhammer, 1999; Padilla y Sánchez, 1985). This was the starting point for the rifting process which formed the Gulf of Mexico (Padilla y Sánchez, 1982; Goldhammer *et al.*, 1991; Goldhammer, 1999). (d) The beginning of the Laramide Orogeny in the Late Cretaceous and Early Tertiary with the development of the detachment of the Mesozoic sedimentary sequence. This created the Sierra Madre Oriental (SMOr; Padilla and Sánchez, 1982; 1985; Eguiluz de Antuñano *et al.*, 2000). (e) The Cenozoic is represented by extensive deformation along normal faults, which are part of Llanura Costera del Golfo Norte de Mexico (LICGNM) (Echánove, 1986; Ortiz Ubilla and Tolson, 2004). As Mickus and Montana (1999) mentioned, the geologic and tectonic framework of northeastern Mexico is known from numerous geological studies and compilations. The region's general crustal structure, particularly the deeper crustal structure, remains relatively unknown due to the lack of published deep drill holes and geophysical studies. These authors determined a general crustal structure of the region by processing gravity data and correlating it to the regional geological and tectonic information of northeastern Mexico.

Historic seismicity

Northeastern Mexico has been considered a tectonically stable region, characterized by low seismicity (Galván-Ramírez and Montalvo-Arrieta, 2008), that according to Johnston *et al.* (1994) represents the southern limit of Eastern North America (ENA). Recent studies show that seismic activity has existed in the area (García Acosta and Suárez Reynoso, 1996; Casasús, 2003). Galván-Ramírez and Montalvo-Arrieta (2008) compiled a catalog of 144 earthquakes for the region from 1787 to 2006 (Figure 1) with magnitudes ranging from 2.3 to 4.8, and three major earthquakes: (1) Parral, Chihuahua in 1928, (M_w 6.5, Doser and Rodríguez, 1993), (2) Valentine, Texas in 1931 (M_w 6.4, Doser, 1987), and (3) Alpine, Texas 1995 (M_w 5.7, Xie, 1998; Frohlich and Davis, 2002). On the

other hand, Rodríguez-Cabo (1946) studied a "swarm" of small earthquakes which took place in August 1944, and which was felt within a 10 km radius from General Terán township, approximately 50 km north of city of Linares. This author proposed that the seismic swarm was originated by the collapse of caverns in the subsoil. It is noteworthy that the conclusions obtained by Rodríguez-Cabo (1946) were not based on seismic stations, but were obtained from what people felt. This can be taken as the first reported evidence of seismic sequences within this region. With the installation of seismological station LNIG in the Linares area (Montalvo-Arrieta *et al.*, 2006; Ramos-Zuñiga *et al.*, 2012b), the recording of seismic activity has increased drastically in northeastern Mexico, increasing from 13 earthquakes reported in the 1981 - 2005 period, to more than 104 quakes in the last six years (2006 - 2012). Approximately 85% of this seismicity took place during a seismic swarm from July to December 2012. Some of these earthquakes have caused minor structural damage near the epicenters in some localities of the state of

Nuevo León, see Ramos-Zuñiga *et al.* (2012a, b) for more details.

Seismic sequence July – December 2012

During July - December 2006, a sequence of small earthquakes ($M_c \leq 3.6$) occurred near the Linares area. Most of the earthquake activity was recorded by the permanent station LNIG of the SSN. The preliminary location of events in the seismicity cluster showed a diffuse image of the seismicity distribution (Figure 2). Several low magnitude earthquakes were felt southwest of city of Linares. Minor damage in houses was reported from some villages near the epicentral area, as well as extensive concern among the population in the region. Small landslides and rockfalls in the SMOr mountain range southwest of Linares were reported. Some preliminary epicentral locations by SSN with the LNIG station suggested the earthquakes occurred northeast of LNIG (Figure 2) but it was necessary to obtain more data to verify the locations of these events.

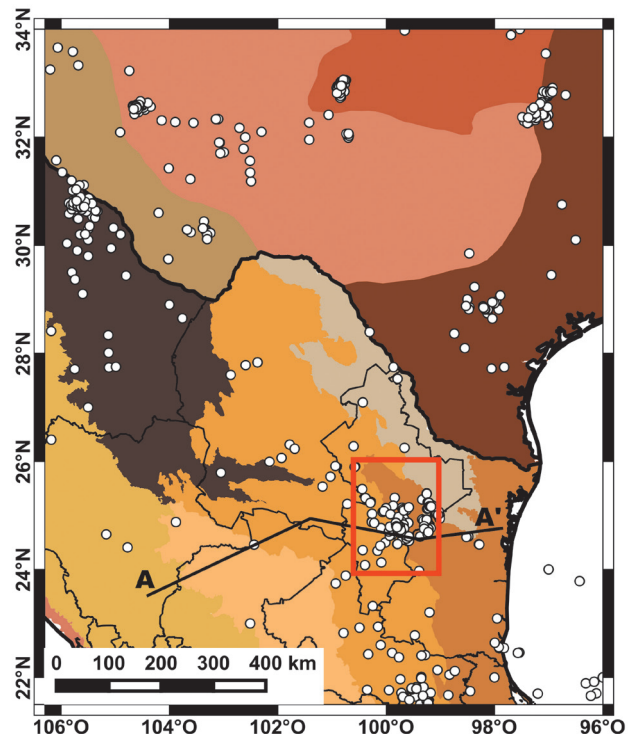


Figure 1. Distribution of seismicity for the 1847-2012 period for the northeastern Mexico and southern Texas. The physiographic provinces of central USA and northern Mexico are indicated by the different colors. The red rectangle is the study area. The solid line A - A' corresponds to the profile of the gravity model proposed by Bartolini and Mickus (2001) used in Figure 10.



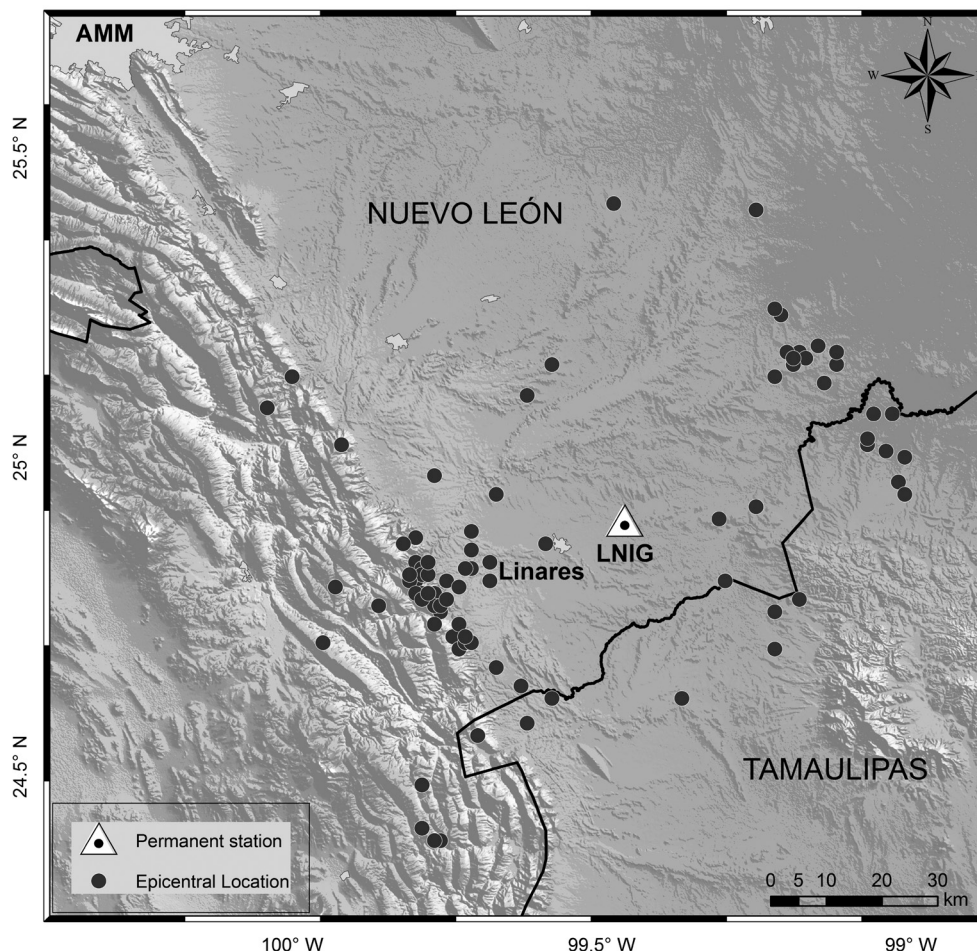


Figure 2. Preliminary epicentral locations obtained using a single station method (LNIG station) for the seismic sequence of July-December 2012 in the state of Nuevo Leon.

Permanent and temporal seismic network

In order to obtain more accurate data for the location of the seismic swarm, the FCT-UANL and the Geophysical Institute, UNAM, installed two temporary seismic stations TAU and BB3 during September-December 2012. The temporary stations were located southwest of the city of Linares near the epicentral area. The permanent LNIG station consists of a STS-2 seismometer, an FBA-23 accelerometer, and a 24 bit Quanterra digitizer. The MNIG stations consist of a Guralp CMG-40T seismometer, a FBA-23 accelerometer and a Reftek digitizer. The temporary stations had a 120 s triaxial Trillium sensor and a 24 bit Taurus digital seismograph. Although these stations were installed during September-December, for various reasons the four stations only recorded simultaneously during November. Otherwise,

in the months of September, October, and December only three seismic stations were simultaneously working.

Relocation

The locations of local earthquakes have been recorded since 2006 by SSN in Northeast Mexico. The data have been obtained from a single 3-component station (one station method, e.g. Alessandrini *et al.*, 1994; Agius and Galea, 2011). This location method has been proved reliable in the absence of more than one seismic station (Frohlich and Pulliam, 1999). With the installation of MNIG, along with two temporary broadband seismic stations, we performed the relocation of 49 events previously reported by the SSN and the location of 3 events not reported previously.

Processing

Earthquake location

Manual picking of P - and S -wave arrival times and measurements of signal duration were performed for events recorded by one or all stations (Figure 3). The velocity model (Table 1) employed by the SSN was used for location. This model is composed of six layers, where the first layer is 16 km thick with $V_p = 6$ km/s, and the V_p/V_s ratio is assumed to be 1.78. We relocated the earthquakes with the program Hypocenter (Lienert and Havskov, 1995) from the Seisan software package (Otemöller *et al.*, 2013). We compared epicenters relocated using the one-station and multiple-station methods. For some locations there was a change in the azimuth direction (of $\sim 45^\circ$ to $\sim 240^\circ$) of the epicenters related to station LNIG as compared to preliminary locations by SSN. This can be attributed to a better station coverage. The epicenters are now located to the west of the

network instead of to the east, although their distance from station LNIG has not changed. Additionally, this work allowed us to show that the difference of one second in the arrival of the phases can create an error in location of 10 km due to the geological structure of the region. The relocated epicenters (Figure 4) show good correspondence with the area of maximum shaking intensity. Many people in the epicentral area reported having heard underground noise previous to feeling the ground shake.

The spatial distribution of stations TAU and BB3 around the cluster helps improve the quality of epicentral locations. The relocation process collapsed the event locations in a northwest-southeast trending cluster along the SMOr mountain range front. The root mean square (*rms*) travel time error values obtained were less than 0.38 s (Figure 5). MNIG was the farthest station, and a distance-based weight was applied to take account of the lower amplitudes of arrivals observed at this station.

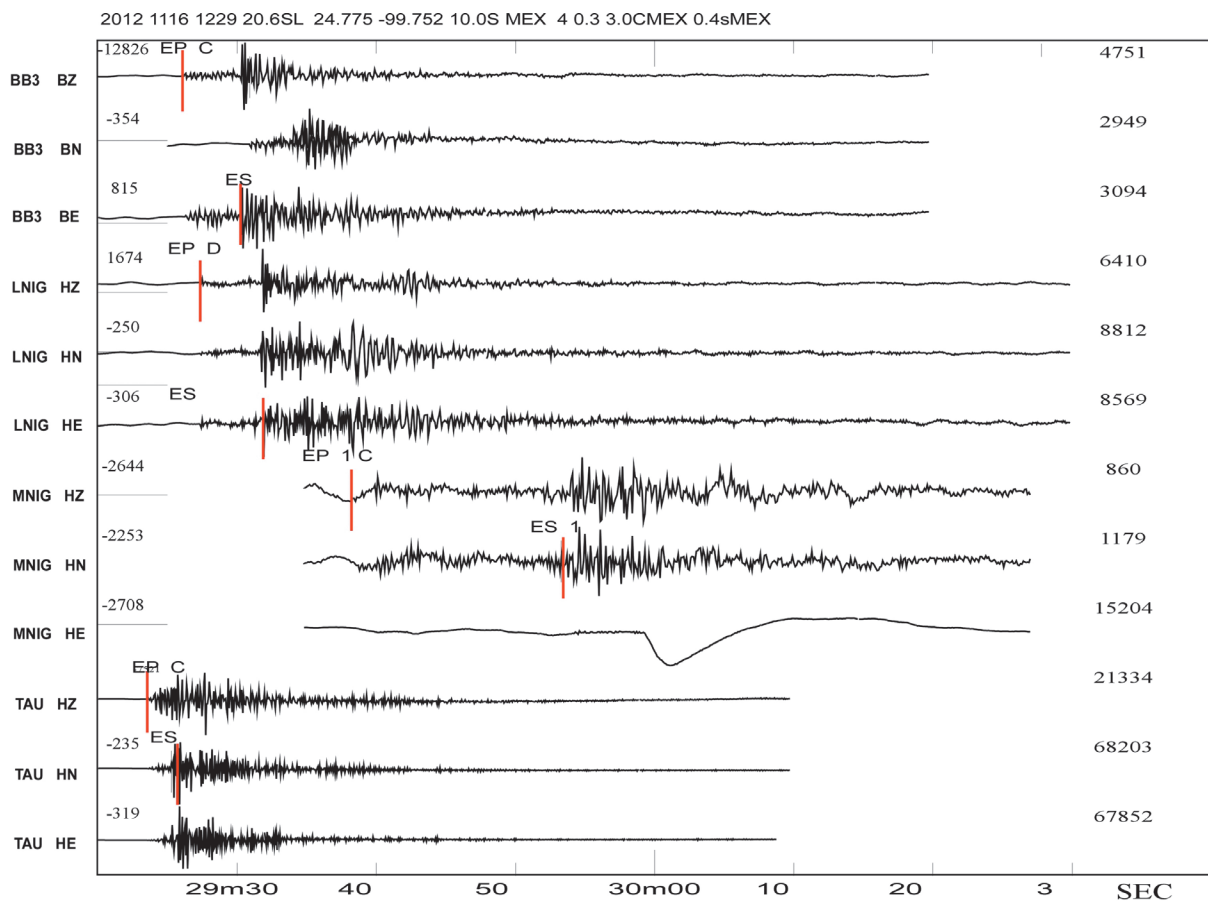


Figure 3. Seismograms for the event of 16 November, 12:29, $M_c 3.0$. The HE component of MNIG was not well recorded due to instrumental problems.

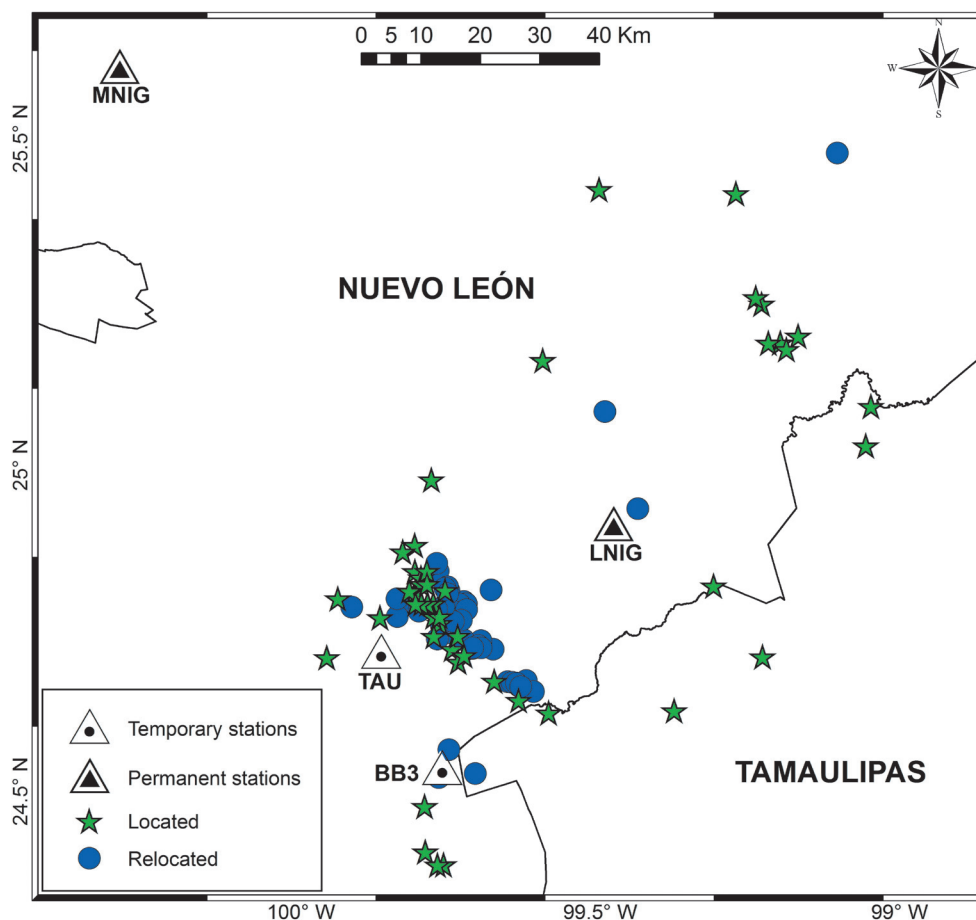


Figure 4. Epicentral comparison between the relocated events using the temporal seismic network (blue dots) and by the one station method using the LNIG (green stars). The new epicentral locations are concentrated to the southwest of LNIG.

The seismic records show similar waveforms between events of the cluster which suggests that the earthquakes come from the same seismic source (Figure 6). The well relocated hypocenters obtained by three or four stations define a focal depth of $8 (\pm 5)$ km for the seismic cluster, while the hypocenters obtained with less than three stations had higher uncertainty (depths varying from 15 to 30 km). Figure 5 (upper right) depicts the residuals obtained for the hypocentral determination of the November 16 (12:29 local time) earthquake ($M_c 3.0$), and the error ellipses of the other three relocations that were obtained with use of the entire four-station network.

To determine the coda magnitude, the seismograms were bandpass filtered between 1 and 5 Hz, and the end of the coda was assumed to occur where the coda wave amplitude had a factor of 2 above the noise amplitude. A

total of 52 well-relocated earthquakes in the magnitude range of 2.6 – 3.6 were obtained from the seismic sequence of more than 250 earthquakes. The rest of the events could not be relocated due to the poor signal-noise levels making it impossible to identify the first P arrive-time.

Focal mechanism

Four of the well relocated earthquakes were used to obtain fault plane solutions that were generated using FOCMEC and HASH. The FOCMEC program uses the first arrival polarities of the P and SH waves and a grid search technique (Snoke *et al.*, 1984). HASH computes double-couple earthquake focal mechanisms from P -wave first motion polarity observations and S/P amplitude ratios (Hardbeck and Shearer, 2003).

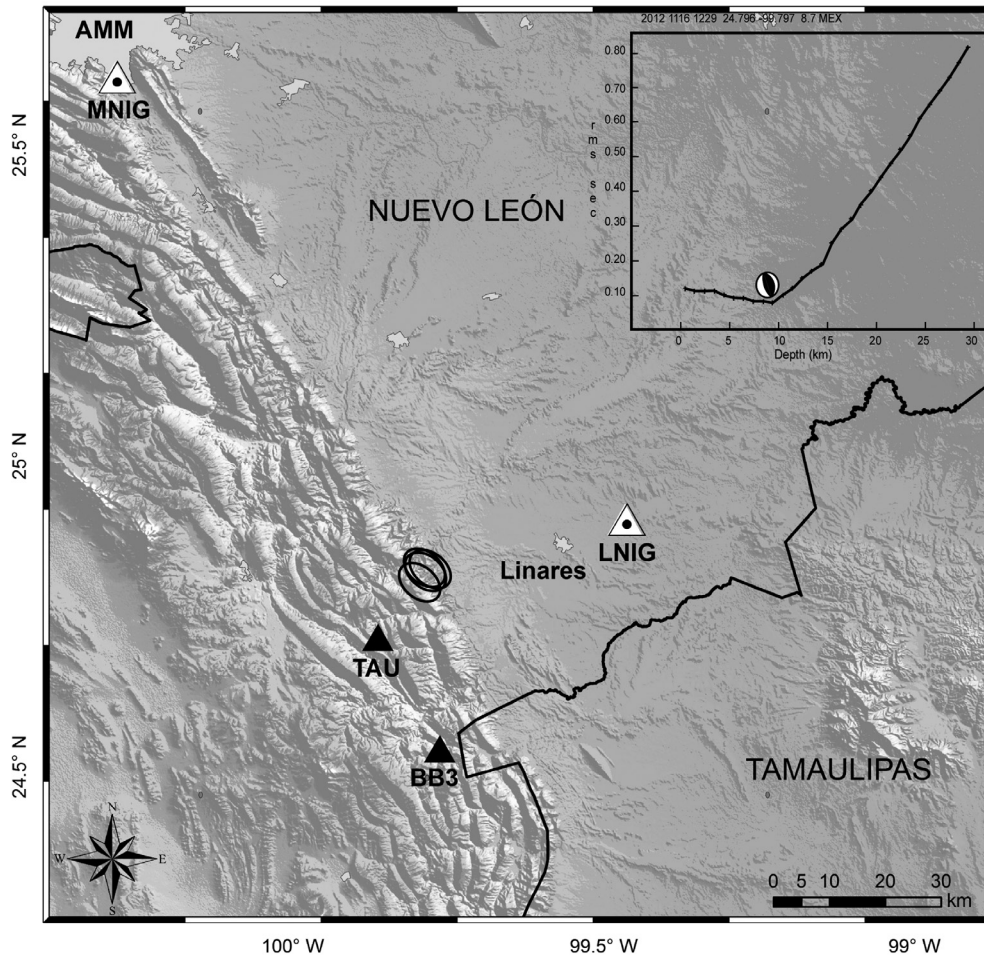


Figure 5. Error ellipses of the four best relocate earthquakes that used the complete four-station network. The upper right corner shows the change of the rms of travel time errors as a function of the focal depth for the 16 November 2012 earthquake.

The solutions obtained for the four earthquakes by FOCMEC and HASH show reverse faulting, and the southwest dipping NNW-SSE trending plane is the inferred fault-plane (Figure 7). Since there is a similarity in the waveforms of the events (Figure 6), it is possible to compute a composite fault plane solution using the 52 best-located earthquakes ($2.5 \leq M_c \leq 3.6$). A composite focal mechanism will give a robust and more general estimate of the stress field orientation. We obtained the composite focal mechanism solutions using SEISAN's FOCMEC program. The results of composite fault plane solution (Figure 8) for the seismic swarm is consistent with individual solutions. The preferred fault's strike was (ϕ) = 150° , dip (δ) = 50° and rake (λ) = 67° , which reveals that maximum horizontal stress $S_{H_{\max}} > S_{h_{\min}} > S_v$ is predominant in the area.

Discussion and conclusions

A good knowledge of the intraplate seismicity that occurs in northeastern Mexico is critical to understanding the actual stress field of the region. The pressure (P) and tension (T) axes derived from earthquake focal mechanisms are one of the most commonly used indicators of tectonic stress (Zoback and Zoback, 1980). The reverse focal mechanism obtained for the 2012 sequence reveals that maximum horizontal stress ($S_{H_{\max}} > S_{h_{\min}} > S_v$) predominates in the area (Figure 9).

As mentioned in the introduction, this region has a complex geological evolution that is manifested through the morphotectonic landscapes at surface (Ramos-Zuñiga *et al.*, 2012a), and by the series of geological features interpreted from geologic information, drill-

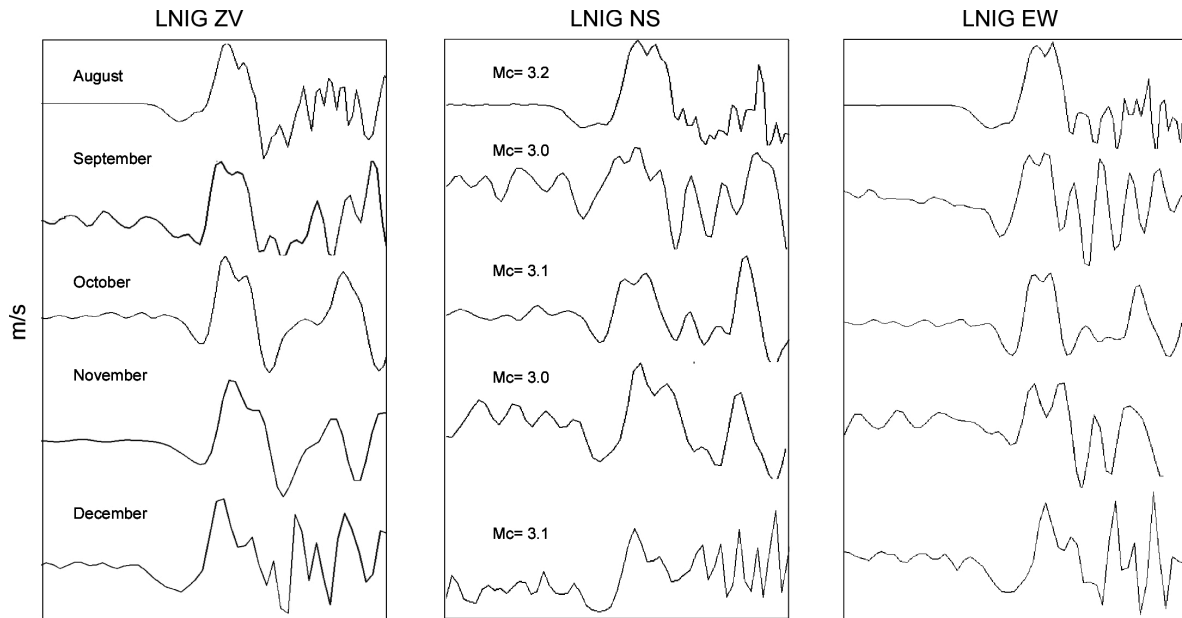


Figure 6. Similarities between waveform for some representative earthquakes of the seismic swarm recorded in LNIG.

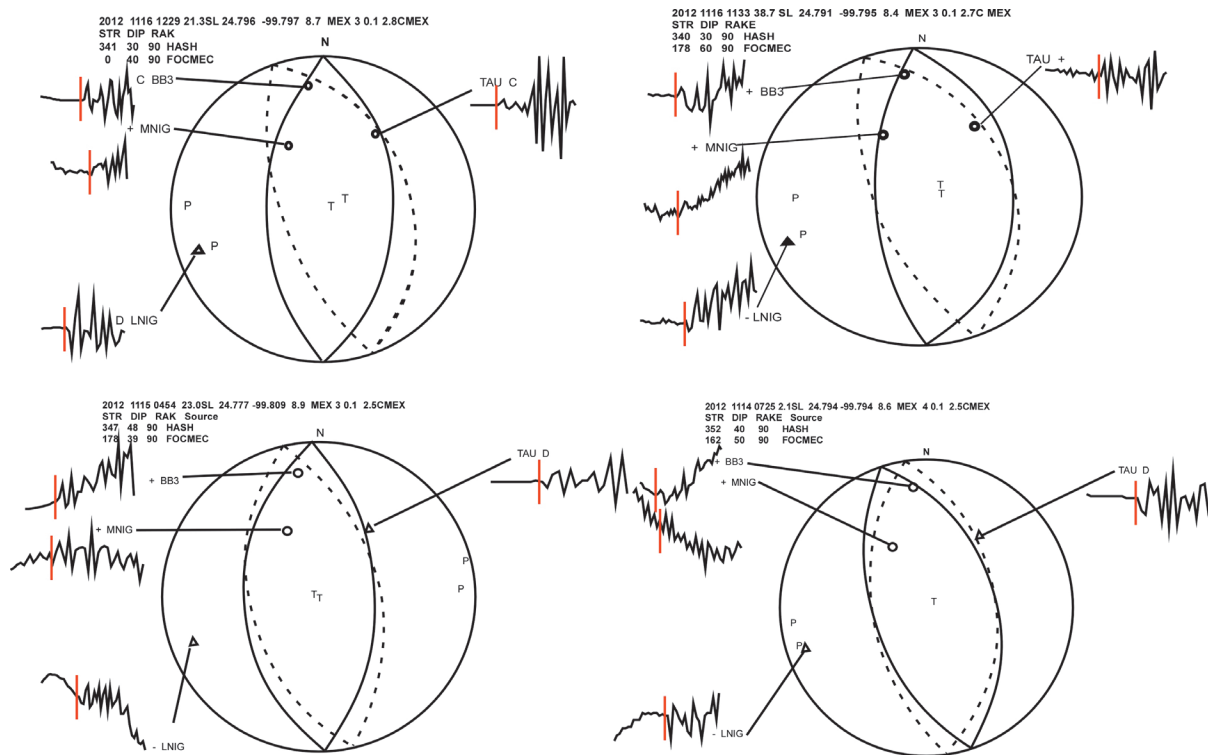


Figure 7. Focal mechanisms from earthquakes recorded by four stations. The seismogram shows the *P*-wave arrival “+” and “-” depict emergent compression and dilatation first motions, respectively; “C” and “D”, corresponding impulsive first motions. The solid line is the solution obtained from FOCMEC, and the dashed line represents the solution from HASH.

Figure 8. Composite focal mechanism obtained from the relocated 52 events of seismic sequence from July to December 2012 using the FOCMEC routine. Solid green dots are compressional and the open blue dots are dilatational first motions.

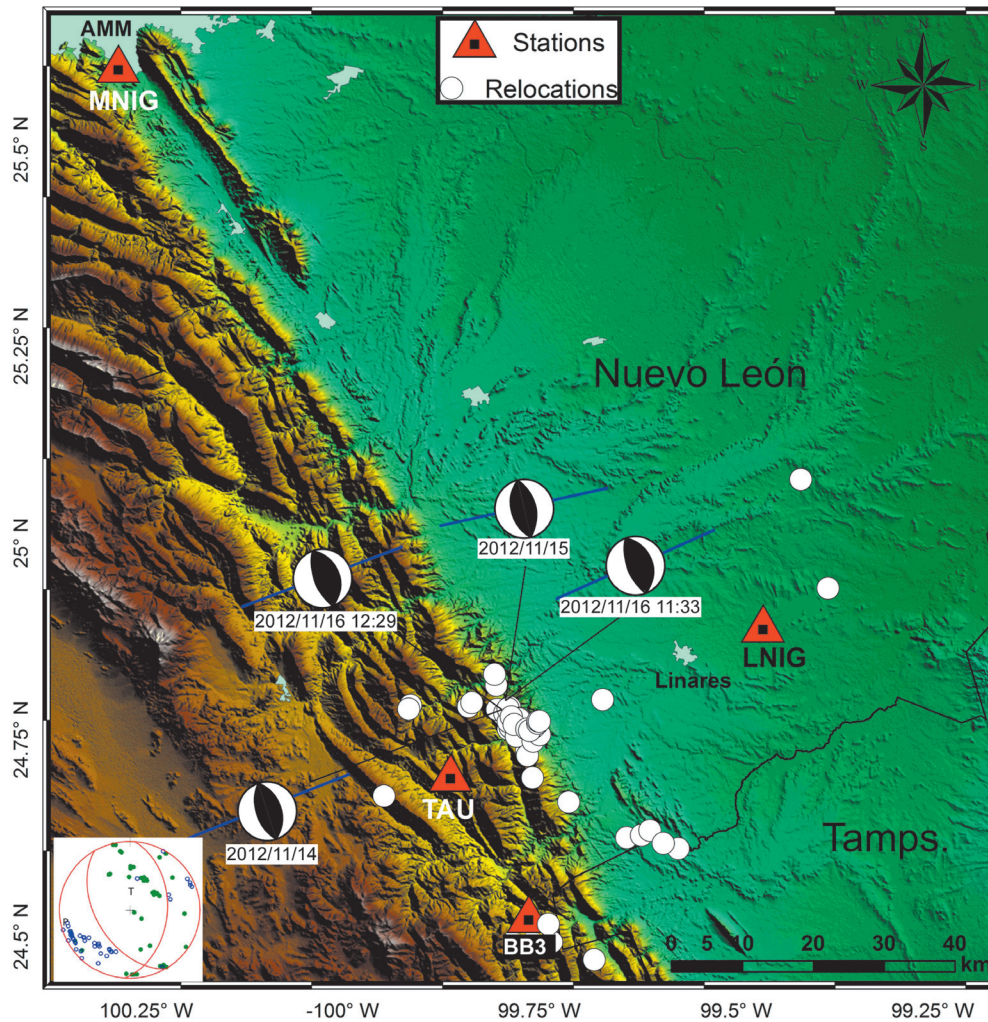
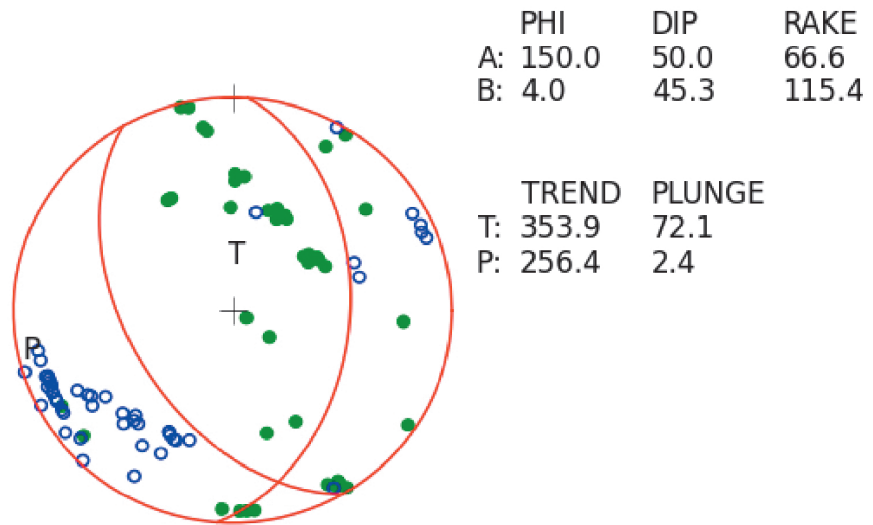


Figure 9. Comparison of relocations and focal mechanisms for the seismic sequence from July to December 2012 in the Nuevo León state. The composite focal mechanism is shown at the bottom left corner.

holle data and gravity models at the crust and upper mantle by Bartolini and Mickus (2001). These authors present a gravity model that crosses the tectonic provinces of Northeastern Mexico. In their gravity profile A-A' (Figure 1) they suggest a crustal boundary composed of two volcanic arcs of Paleozoic and Mesozoic ages, respectively, located approximately at 450 - 480 km from the western edge of their model which coincides with the SMOr and LICGM provinces boundary (Figure 10). The well relocated hypocenters appear to lie at the edge of an upper crustal sequence of Jurassic-Cretaceous strata and lie about 20 km east of the modeled Triassic-Jurassic arc.

On the other hand, at surface, the seismic swarm had an epicentral distribution parallel to the SMOr mountain range front (Figure 9). The fault-plane solution obtained shows a pure reverse faulting, being the SW dipping NNW - SSE trending nodal plane the inferred fault plane.

According to some authors, the current stress field in northeastern Mexico is extensional. Suter (1991) mentions that

the S_{Hmax} direction in the states of Coahuila and Nuevo Leon in the area of the Laramide Coahuila foldbelt is parallel to the Rio Grande rift and Quaternary faults in west Texas and northeast Chihuahua. This parallelism suggests a stress field with $S_V > S_N > S_E$ direction. In the same way, Márquez-Azúa and DeMets (2003) used observations of continuous GPS stations in Mexico to suggest that sites located in northern Mexico (Chihuahua, Tampico, and Monterrey) show residual velocities varying between 1.5 and 3.0 mm/year oriented in a southeast direction, following the present pattern of extension of the Basin and Range provinces. In this sense, the compressional stress field obtained from the 2012 seismic sequence could be considered as contradictory. However, this compressional behavior is the outcome of the deformation caused by push (movement to the East) and possible overthrust of a less dense block A (composed of Jurassic-Cretaceous strata, Triassic-Jurassic arc rocks, and Paleozoic-Jurassic upper crust) that is locked by a denser block B (composed of Permian granite, and Precambrian-Paleozoic upper crust) located just east of the SMOR

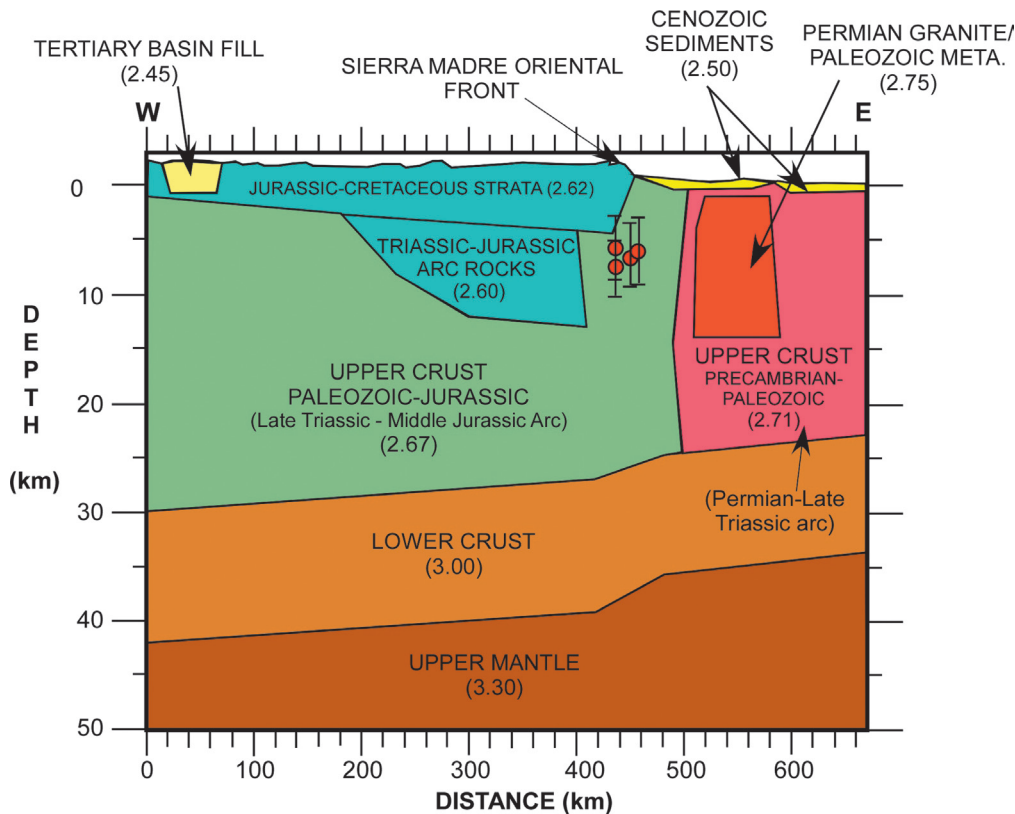


Figure 10. 2.5-D gravity model along profile A - A' (Figure 1) from Bartolini and Mickus (2001) that crosses the southern part of the state of Nuevo León. The numbers in parentheses represent the bodies' average density in gm/cc. We have projected the locations of the four best-recorded earthquakes from the seismic sequence of July to December 2012 on to the section. The error bars indicate depth uncertainty.

front (Figure 10). This results in a compressive stress field that triggers the reactivation of reverse faulting in the area near the mountain front (where the pre-existing faults zones are associated with ancient suture zones). Therefore, the lateral variations in crustal densities and thickness documented in this region can be considered to be the factor that changes the current extensional stress field proposed for northeastern Mexico into a pattern of compressional stress ($S_{Hmax} > S_{Hmin} > S_v$). The same effect is suggested to occur at the limit between the Southern Great Plains and the Mid-Continent provinces north of this region within the United States of America (Zoback and Zoback, 1980).

Aknowledgements

We are grateful to Xyoli Pérez-Campos (Associate Editor) and two anonymous reviewers for their critical comments on the manuscript that helped improve it. Thanks to M. M. González-Ramos for the critical reading of the manuscript and various useful remarks. The MSc Carmen M. Gómez-Arredondo received a scholarship from CONACYT and support by the *Programa Integral de Fortalecimiento Institucional de la Secretaría de Educación Pública*. Rocío L. Sosa-Ramírez helped with Figure 1. SSN data was obtained by the Servicio Sismológico Nacional (México) and acquisition and distribution was thanks to its personnel.

References

- Agius M.R., Galea, P., 2011, A Single-Station Automated Earthquake Location System at Wied Dalam Station, Malta. *Seismol. Res. Lett.*, 82, 545-559.
- Alessandrini B., Cattaneo M., Demartin M., Gasperini M., Lanza V., 1994, A simple, P-wave polarization analysis its application to earthquake Location. *Annals of Geophysics* 37, 883-897.
- Bartolini C., Mickus K., 2001, Tectonic Blocks, Magmatic Arcs, and Oceanic Terrains: A Preliminary Interpretation Based on Gravity, Outcrop, and Subsurface Data, Northeast-central Mexico. *American Association of Petroleum Geologists, Memoirs* 75, 29-44.
- Casasús F.R., 2003, Monterrey 407 trozos de su historia. Creatividad Editorial, 188 pp.
- Crone A.J., De Martini P.M., Machette M.N., Okumura K., Prescott, J.R., 2003, Paleoseismicity of Two Historically Quiescent Faults in Australia: Implications for Fault Behavior in Stable Continental Regions. *Bull. Seism. Soc. Am.*, 93, 1913-1934.
- Doser D.I., 1987, The 16 August 1931 Valentine, Texas, earthquake: evidence for normal faulting in west Texas. *Bull. Seism. Soc. Am.*, 77, 2005-2017.
- Doser D.I., Rodríguez J., 1993, The seismicity of Chihuahua, Mexico, and the 1928 Parral earthquake. *Phys. Earth Planet In.*, 78, 97-104.
- Echánove E.O., 1986, Geología petrolera de la Cuenca de Burgos. Parte I. Consideraciones Geológico-petroleras. *Boletín de la Asociación Mexicana de Geólogos Petroleros*, 38, 3-39.
- Eguiluz de Antuñano S., Aranda-García M., Marrett R., 2000, Tectónica de la Sierra Madre Oriental, México. *B. Soc. Geol. Mex.*, 53, 1-26.
- Frohlich C., Pulliam J., 1999, Single-station location of seismic events: A review plea for more research. *Phys. Earth Planet In.*, 113, 277-291.
- Frohlich C., Davis S.D., 2002, Texas earthquakes. Springer, 277 pp.
- Galván-Ramírez I.N., Montalvo-Arrieta J.C., 2008, The historical seismicity and prediction of ground motion in Northeast Mexico. *J. S. Am. Earth Sci.*, 25, 37-48.
- García Acosta V., Suárez Reynoso G., 1996, Los sismos en la historia de México, Universidad Nacional Autónoma de México, 718 pp.
- Goldhammer R.K., Lehmann P.J., Todd R.G., Wilson J.L., Ward W.C., Johnson C.R., 1991, Sequence Stratigraphy and Cyclostratigraphy of the Mesozoic of the Sierra Madre Oriental, Northeast Mexico: a Field Guidebook, Gulf Coast Section, *Society of Economic Paleontologists and Mineralogists*, 85 p.
- Goldhammer, R.K., 1999, Mesozoic sequence stratigraphy and paleogeographic evolution of northeast Mexico, in Bartolini, C., Wilson, J.L., and Lawton, T.F. (eds.), Mesozoic sedimentary and tectonic history of North-Central Mexico. *Geological Society of America Special Paper*, 340, 1-58.
- Hanks, T.C., Johnston A.C., 1992, Common features of the excitation and propagation of strong ground motion for North American earthquakes. *Bull. Seism. Soc. Am.*, 82, 1 23.

- Hardbeck J.L., Shearer P.M., 2003, Using S/P amplitude ratio to constrain the focal mechanisms of small earthquakes. *Bull. Seism. Soc. Am.*, 93 2434–2444.
- Hurd O., Zoback M.D., 2012, Intraplate earthquakes, regional stress and fault mechanics in the Central and Eastern U.S. and Southeastern Canada. *Tectonophysics*, 581, 182–192. doi:10.1016/j.tecto.2012.04.002
- Johnston A.C., Coppersmith K.J., Kanter L.R., Cornell C.A., 1994, The earthquakes of stable continental regions: Assessment of large earthquake potential, in Schneider, J.F., ed., *Electronic Power Research Institute Report TR-102261*: Palo Alto, California, Electronic Power Research Institute, 309 p.
- Lienert B.R., Havskov J., 1995, A computer program for locating earthquakes both locally and globally. *Seismol. Res. Lett.*, 66, 26–36.
- Márquez-Azúa B., Demets C., 2003, Crustal velocity field of México from continuous GPS measurements, 1993 to June 2001: implications for the neotectonics of Mexico. *J. Geophys. Res.*, 108 (B9), 2450. doi:10.1029/2002JB002241.
- Mickus K., Montana C., 1999, Crustal structure of northeastern Mexico revealed through the analysis of gravity data. *Geological Society of America Special Paper*, 340, 357-371.
- Montalvo Arrieta J.C., De León Gómez H., Valdéz González C., 2006, LNIG: Nueva estación sísmica digital en el noreste de México. *Ingenierías*, Julio-Septiembre 2006, 9, 17-24.
- Montalvo-Arrieta J.C., Sosa-Ramírez R.L., Paz-Martínez E.G., 2015, Relationship between MMI data and ground shaking in the state of Nuevo León, Northeastern Mexico. *Seismol. Res. Lett.* 86, 1489-1495. doi: 10.1785/0220140206.
- Ortiz-Urbilla A., Tolson G., 2004. Interpretación estructural de una sección sísmica en la región Arcabuz-Culebra de la Cuenca de Burgos, NE de México. *Rev. Mex. Cienc. Geol.*, 21, 226–235.
- Otemöller L., Voss P., Havskov J., 2013, *Seisan Earthquake Analysis Software*, for Windows, Solaris, Linux and MacOSx, version 10, 402.
- Padilla y Sánchez R.J., 1982, Geologic Evolution of the Sierra Madre Oriental between Linares, Concepción del Oro, Saltillo and Monterrey, Mexico, Austin, Texas, University of Texas at Austin. Tesis Doctoral, 217 pp.
- Padilla y Sánchez R.J., 1985, Las estructuras de la Curvatura de Monterrey, Estados de Coahuila, Nuevo León, Zacatecas y San Luis Potosí. *Revista del Instituto de Geología UNAM*, 6, 1-20.
- Ramos Zúñiga L.G., Medina-Ferrusquía H.C., Montalvo-Arrieta J.C., 2012a, Patrones de Sismicidad en la curvatura de Monterrey, noreste de México. *Rev. Mex. Cienc. Geol.*, 29, 572-589.
- Ramos Zúñiga L.G., Montalvo-Arrieta J.C., Pérez-Campos X., Valdés-González C., 2012b, Seismic characterization of station LNIG as a reference site in Northeast Mexico. *Geof. Int.*, 51, 185-195.
- Rodríguez Cabo, J.R., 1946, Fenómenos geológicos en General Terán, Nuevo León. *B. Soc. Geol. Mex.*, 21, 7-43.
- Sedlock R., Ortega-Gutiérrez F., Speed R., 1993, Tectonostratigraphic terranes and tectonic evolution of México. *Geological Society of America, Special Paper*, 278-153.
- Snoke J.A., Munsey J.W., Teague A.G., Bollinger G.A., 1984, A program for focal mechanism determination by combined use of polarity and SV-P amplitude ratio data. *Earthquake Notes*, 55, 15.
- Stewart J.H., 1988, Latest Proterozoic and Paleozoic southern margin of North America and accretion of Mexico. *Geology*, 16, 186-189.
- Suter M., 1991, State of stress and active deformation in Mexico and western Central America. In: Slemmons, D.B., Engdahl, E.R., Zoback, M.D., Blackwell, D.D. (Eds.), *Neotectonics of North America*: Boulder, Colorado, Geological Society of America, Decade Map vol. 1, 401–421.
- Torsvik T.H., 2003, The Rodinia Jigsaw Puzzle. *Science*, 1379-1381.
- Xie J., 1998, Spectral inversion of Lg from earthquakes: a modified method with applications to the 1995, Western Texas earthquake sequence. *Bull. Seismol. Soc. Am.*, 88, 1525–1537.
- Zoback M.L., Zoback M.D., 1980, State of stress in the Conterminous United States. *J. Geophys. Res.*, 85, 6113 – 6156.

Geophysical modeling of the manganese deposit for Induced Polarization method in Itapira (Brazil)

Leandro B. Vieira*, César A. Moreira, Ariane R. P. Côrtes and George L. Luvizotto

Received: April 18, 2015; accepted: February 09, 2016; published on line: April 01, 2016

Resumen

Este artículo presenta la aplicación de los resultados del método geofísico de Polarización Inducida (IP) en el estudio de la ocurrencia de manganeso supergénicos en el sudeste de Brasil, con análisis de la arquitectura del depósito en subsuelo, basado en el contraste de las propiedades físicas de los minerales de mena (óxidos hidróxidos de manganeso y grafito) y la roca alrededor. El contexto geológico regional se define por la ocurrencia de tipos de roca que pertenecen al Complejo Amparo y Grupo Itapira. Este Grupo acoge la mineralización en una sucesión de cuarcitas, esquistos y gneises con porciones subordinadas. El estudio geofísico consistió en 10 líneas paralelas de calicatas eléctricas en dispositivo Wenner-Schlumberger, con una separación entre los electrodos de 10m y 50m entre líneas. Los datos de campo permitieron la generación de modelos de inversión 2D posteriormente combinan y interpolados para generar modelos de visualización 3D, de la que eran cuerpos de mineral probables delimitados en profundidad y la comparación de las dimensiones de la formación laterítica reconocidos en el campo. Se reconocieron dos cuerpos independientes de mineral en profundidad, que se caracterizan por valores de alta cargabilidad (por encima de 20mV/V) atribuida a la presencia de grafito en cantidades de hasta 5 %. Los cuerpos de mineral en profundidad mostraron área de cobertura mucho menor para la formación laterítica. Visualización 3D habilitado una estimación de la morfología de los cuerpos, sentido del buceo y la identificación de orientación transversal a la estructuración regional de plegado.

Palabras clave: calicatas eléctricas, manganeso supergénico, grafito, cargabilidad, modelamiento 3D.

Abstract

This paper presents the results of the investigation of a supergene manganese occurrence in the southeast of Brazil, using the Induced Polarization geophysical method. This study aims to characterize the surface and subsurface morphology of one of these occurrences, named São Roque, based on the contrast of the electrical properties of the ore and the host rocks. The ore, which is composed mainly of manganese oxides and hydroxides and subordinated graphite, occurs in the form of small discontinuous lenses hosted by quartzites and schists of the Itapira Group. The geophysical survey consisted on 10 lines of Induced Polarization Tomography using a Wenner-Schlumberger array, with an along-line electrode separation of 10 m for all lines. The IP data were modeled through commercial inversion software to generate 2D section models of chargeability. In order to create a 3D visualization model of chargeability, the 2D inversion models were then combined and interpolated in order to create a 3D visualization model. The 3D model revealed two independent ore bodies in both surface and subsurface, characterized for high chargeability (up to 20mV/V), instead of a single elongated orebody as suggested by the lateritic surface in the field. In addition, the model showed that the orebodies are elongated perpendicular to the area main structural trend and the regional alignment of the lateritic occurrences, which can bring new ideas in terms of local exploration strategies for manganese in this context.

Key words: electrical tomographic, lateritic manganese, graphite, chargeability, 3D modeling.

C. A. Moreira
Departamento de Geologia Aplicada (DGA)
Instituto de Geociências e Ciências Exatas (IGCE)
Universidade Estadual Paulista Júlio de Mesquita Filho
Av. 24-A, 1515, Bela Vista. CEP 13506-900,
Rio Claro, SP.

G. L. Luvizotto
Departamento de Petrologia e Metalogenia (DPM)
Instituto de Geociências e Ciências Exatas (IGCE)
Universidade Estadual Paulista Júlio de Mesquita Filho
Av. 24-A, 1515, Bela Vista. CEP 13506-900,
Rio Claro, SP.

L. B. Vieira*
A. R. P. Côrtes
Programa de Pós-graduação em Geociências
Instituto de Geociências e Ciências Exatas (IGCE)
Universidade Estadual Paulista Júlio de Mesquita Filho
Av. 24-A, 1515
Bela Vista. CEP 13506-900, Rio Claro, SP.
*Corresponding author: vieirabl@gmail.com

Introduction

The Brazilian economy is highly dependent on the mineral sector. Brazil is the owner of the biggest world reserves of niobium (98.2%), barite (53.3%) and graphite (50.7%), second biggest of tantalum (36.3%) and REE (16.1%), third biggest of nickel (13.7%) and tin (10.0%) and fourth biggest of iron (13.6%), manganese (8.8%) and vanadium (1.3%). The mineral sector employs more than one million people directly and indirectly and the sum of mineral extraction in 2013 was more than 77 billion dollars (4.1% of the Gross Domestic Product - GDP) (MME, 2014).

Manganese has great importance in steelmaking industry (to increase the steel strength and resistance to corrosion), to decolourise glass, to make fertilizers, ceramics and especially for the batteries industry (Gonçalves & Serfaty, 1976). As its internal consumption and exportation increases, also increases the necessity of finding new deposits.

Ore is a material from which minerals and metals of intrinsic economic value or interest can be economically extracted at the present time (Peters, 1987; Misra, 1999; Moon *et al.*, 2006; Guilbert & Park, 2007). A prospect is a restricted volume of ground, which is considered to have the possibility of directly hosting an ore body, selected based on some geological idea or an anomalous feature of the environment (Marjoribanks, 2010).

Once a prospect has been defined, exploration work advances through a series of progressive detailing stages where success leads to the next stage and negative results might cause the prospect to be discarded, sold or put on hold until new information, ideas or technology arrive. Exploration techniques will generally go through the main stages: target generation; target drilling; resource evaluation drilling and feasibility studies (Milsom & Eriksen, 2011; Marjoribanks, 2010).

One of the techniques used for the search and investigation of an orebody is exploration geophysics (Reedman, 1979). Its use begins in the reconnaissance stages, where airborne methods are applied in regional scales for the definition of new prospects, and continues into most detailed stages where ground methods are employed directly towards delimitating the orebodies in subsurface (Ford *et al.*, 2007). Geophysical surveys are aimed at measuring rock properties (electrical, magnetic, density, mechanical, etc.), which may reflect or have straight relationships to

economic mineralizations. Measurements that are considered anomalous (that is, above area background) are then analyzed to determine its nature, size, position and shape as a prelude for a follow-up detailed exploration stage, usually drilling (Keller & Frishknecht, 1970; Moon *et al.*, 2006; Dentith & Mudge, 2014).

Electrical methods are vastly used in mineral exploration. As they are essentially ground methods, they are mainly applied to local studies like prospect investigation for subsequent drilling (Robinson, 1988). Amongst several geoelectrical methods, the Induced Polarization Method (IP) is important in base metal exploration because it depends on the surface area of the conductive mineral grains rather than their connectivity; therefore, the method is especially sensitive to disseminated mineralization (Keller & Frishknecht, 1970). IP effects can be very strong at the surface of grains of conducting minerals such as graphite and metallic sulfides. Graphite is generally considered a drawback for the method. It is often said to be a "indicator of pyrite" due to their similar (both high) polarization responses (Moon *et al.*, 2006).

The IP method has been historically used for the search of disseminated sulfide and gold ores (and graphite in a lesser extent), in the most variable geological settings (Pelton & Smith, 1976; Moreira *et al.*, 2012; Langore & Gjovreku, 1989; Allis, 1990; Izawa *et al.*, 1990; Irvine & Smith, 1990; Locke *et al.*, 1999; Dentith & Barrett, 2003). However, few references can be found about the use of IP method in the search and investigation of manganese primary and secondary ore deposits (Moreira *et al.*, 2014; Ramazi & Mostafaie, 2013).

This paper presents the results of the IP method applied on the study of a supergene manganese occurrence in the southeast of Brazil, with the aim of analyzing the orebody architecture in subsurface based on the contrast between the ore minerals (Mn oxides, hydroxide and graphite) and host rocks.

Study area

The site of study is located in the northeast of São Paulo State, Brazil, around 6 km to the east of Itapira city (Figure 1).

The area is located in the Alto Rio Grande Fold Belt, Central Sector of Mantiqueira Province, Brazil (Hasui & Oliveira, 1984). The Alto Rio Grande Fold Belt is a Middle Proterozoic tectonic province, thrust upon fragments of a

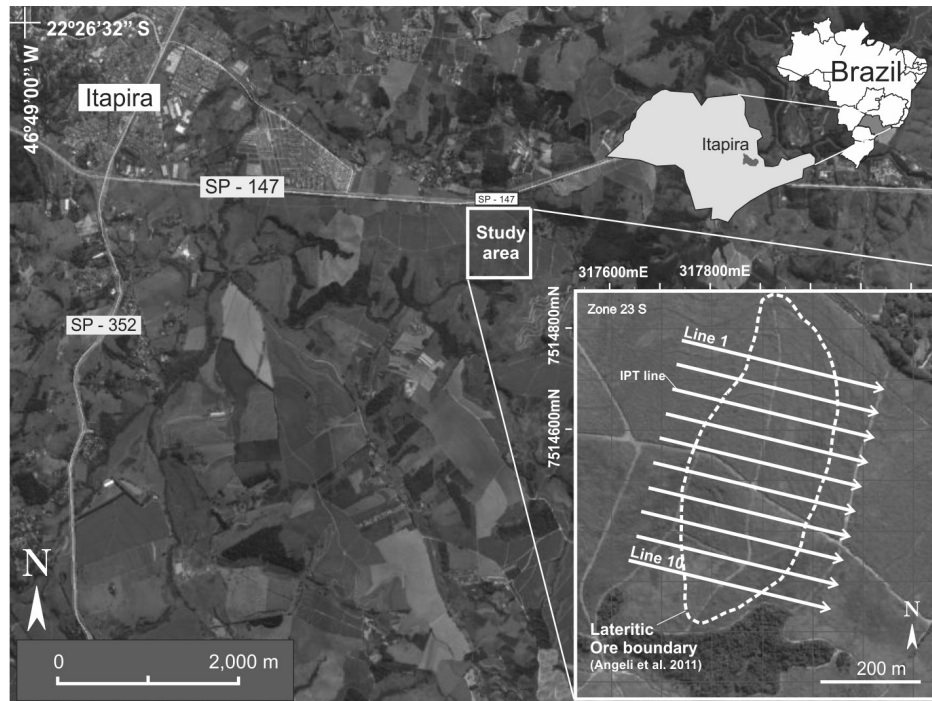


Figure 1. Map showing the location of the study area and location of the IPT survey.

microcontinent formed in successive orogenies during the Archean and Early Proterozoic. The geological and geochronological history of these terranes show subsequent metamorphic episodes of crust-forming and reworking of continental material since 3.4 Ga until 600 Ma with the Late Proterozoic Brasiliano Orogeny (Tassinari & Campos Neto, 1988; Campos Neto, 1991; Lazarini, 2000).

The surrounding geology is represented by lithotypes of the Amparo Complex (infracrustal basement rocks) and metasediments of the Itapira Group (Mesoproterozoic supracrustal rocks).

The Amparo Complex is composed of high-grade metamorphic rocks including migmatites and orthogneiss of tonalitic to granodioritic composition. The group is marked by a complex structural pattern resulting from superimposed tectono-metamorphic events that has shaped the area since Archean times (Fiori *et al.*, 1978; Artur *et al.*, 1979; Fiori *et al.*, 1980).

The Itapira Group, which hosts the manganese occurrences in the area, is an allochthonous metavolcano-sedimentary sequence, thrust over the older rocks of the Amparo Complex. The group is composed mainly by quartzites, schists, quartz

schists, silimanite-garnet paragneisses and subordinated gndites (Wernick, 1976; Arthur, 1980; Veríssimo, 1991; Angeli *et al.*, 2011). The rocks of the Itapira Group show a complex structural pattern, characterized by high angle dextral sense shear zones that are consistent with a transpressive deformation in a ductile to ductile-brittle regime. The main structures are tight folds, refolded or not and sheared folds with steeply-dipping angles in their axial portions.

Artur (1980) recognized at least three phases of regional metamorphism and deformation in the area, resulting from recurring collision events from the Palaeoproterozoic to the Neoproterozoic. The last event, the Brasiliano/Pan-African, was responsible for the reactivation of older crustal structures, folding and shearing, leading to the formation of a sequence of synforms and antiforms with fold axial plane strike NE-SW, perpendicular to the axial plane strikes of the previous deformational event, which is NW-SE.

The individualization of each unit in the field is a difficult task, due to the complex structural pattern caused by the superimposed metamorphism and deformation that affected both groups. However, it is known that the units are organized as a set of sinform-antiform

structures, where the sinforms are represented by lithologies of the Itapira Group and the antiforms are represented by the Amparo Complex (Wernick, 1976).

A few lateritic manganese occurrences are found in the area, of which some of them have been studied in terms of their mineralogical and chemical composition, genesis and ore processing (Zanardo, 2003; Veríssimo, 1991; Angeli, 2011). The occurrences are arranged in a NNE-trend, coincident with the area main structural trend and separated from each other by a few hundreds of meters (Figure 2).

The ore is residual and consists of secondary manganese oxides and hydroxides formed by the weathering of silicate and silicate-carbonate protore. Lithiophorite, cryptomelane and pyrolusite make up the highest grade ores, derived from the dissolution and redeposition of Mn from the protore.

Two different types of protore are found in the deposits: silicate protore (essentially quartz and spessartite in equal proportions) and silicate-carbonate protore (rhodochrosite, rhodonite, pyroxenes and amphyboles in addition to quartz and spessartite). Graphite is found in both ore and protore, in amounts that can reach up to 10% (Veríssimo, 1991; Angeli *et al.*, 2011). The mineralogy of the protore and the presence of graphite suggest a terrigenous source for the metal and a meta-sedimentary origin for the manganese orebodies (Veríssimo, 1991).

The formation of primary sedimentary and residual manganese ore deposits is determined by the interaction of several processes, which may include its extraction from the source rocks, its fluvial transportation and its precipitation when in favorable pH and Eh conditions. In addition, chemical weathering can lead to the development of high-grade

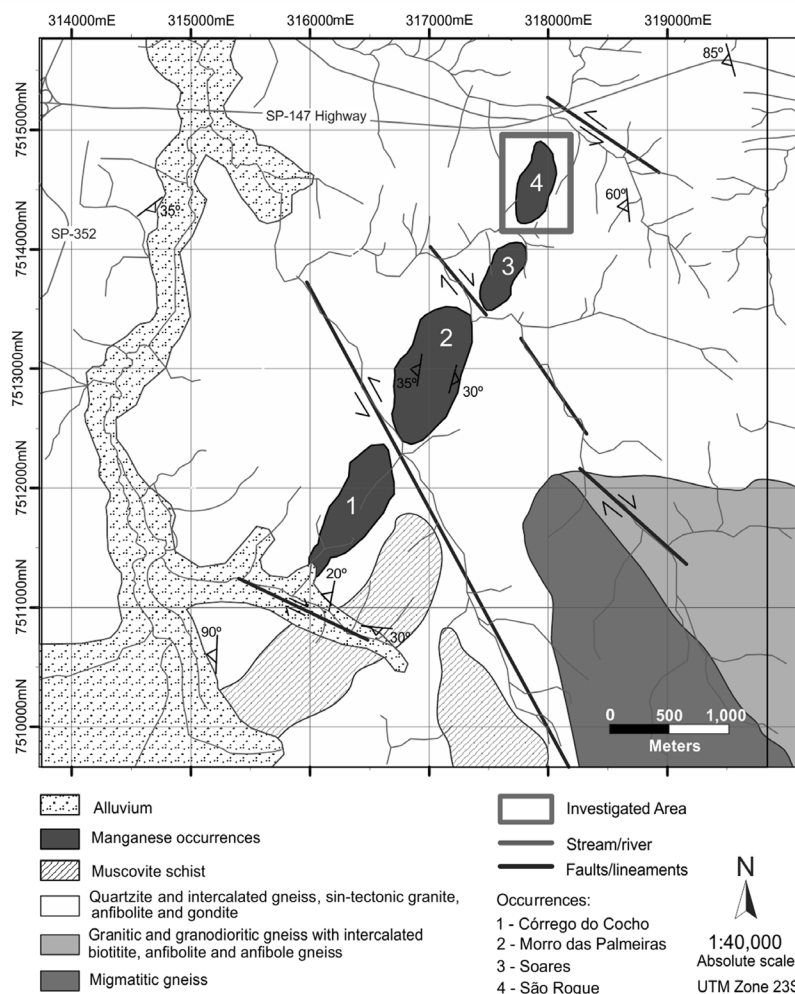


Figure 2. Simplified geological map of the study area. Modified from Angeli (2011).

residual (secondary) deposits (Stanton, 1972; Roy, 1992; Maynard, 2003; Misra, 1999; Guilbert & Park, 2007; Polgári & Gutzmer, 2012).

Gondites are metamorphosed sedimentary manganese-bearing arenaceous and argillaceous sediments with spessartine and quartz, besides rhodonite and other manganese silicates (Roy & Mitra, 1964). Eventual lateritic alteration can occur to the manganeseiferous protosols under humid tropical to subtropical conditions, causing the remobilization of Mn and its precipitation as secondary manganese minerals (Sethumadhav *et al.*, 2010).

Lateritic manganese cappings are originated from the physicochemical weathering of primary manganese deposits, including gondites. The weathering and transport of elements inside the lateritic profile modify the primary mineral content of the deposit, both vertically and horizontally (Wolf, 1976; Taylor, 2011). The leaching of manganese from higher surface levels causes them to become impoverished in that element and enriched in iron, leading to the formation of lateritic iron ore cappings on the surface and manganese enriched surfaces in the intermediate parts of the lateritic profile. As the laterization processes continue, manganese lateritic surfaces are formed in the intermediate parts of the alteration profiles, as a result of the vertical and oblique element mobilization (Wolf, 1976; Taylor, 2011). The leaching of the undesirable elements and the concentration of the manganese in the lateritic profiles might lead to the formation of high grade, economic deposits (Stanton, 1972; Park & MacDiarmid, 1975).

Lateritic ore cappings are a very important feature in terms of manganese exploration, as they are easily recognized in the field because of the characteristic black color they bring to the ground. However, their greater areal extent when compared to the primary deposits very often causes the overestimation of the concealed primary deposits.

Methods

The occurrence was studied using Induced Polarization Tomography (IPT), carried out within an area of approximately 500m by 600m. A total of 10 lines were positioned perpendicular to the local main structural trend, NNE, parallel and spaced 50 m to each other. The total length was 420 m for each line (two multi-electrode cables with 21 stations each), with an along-line electrode separation

of 10m for all lines. Were performed a total of 10280 measures, of which half the readings of electrical resistivity and half of chargeability.

Data were collected through a Wenner-Schlumberger array, multi-electrode cables (21 take-outs each) and non-polarizable porous-pot electrodes (Cu-CuSO₄). The Wenner-Schlumberger array has good signal-to-noise ratio and imaging resolution (Dahlin & Zhou, 2004), and has been successfully used in the prospecting and 2D and 3D modeling of mineral deposits (Moreira *et al.*, 2012; Moreira *et al.*, 2014). The opening and saturation of cavities for placement of the electrodes with solution of CuSO₄, resulted in minimum contact resistance and a great signal-to-noise ratio.

The equipment used was an ABEM Terrameter LS (Sweden), which consists in automatic and programmable single transmission/reception module with the capacity to acquire Spontaneous Potential (SP), DC resistivity (ER) and Induced Polarization (IP) field data. Data are then automatically registered into the equipment internal memory, in the chosen data file format, without any human interference (ABEM, 2012).

The survey acquisition parameters were: injected current = 500mA; injection time = 2s; acquisition time delay = 0.2s and a single acquisition time window of 0.1s, with the adoption of a ceiling of 3% of maximum standard deviation in relation to the average of measured values. These parameters were fixed after preliminary tests in the field, for verification and analysis of disturbances as power lines, telluric noise, EM coupling, among other.

The inverse modeling was done using the Res2dinv software (Geotomo Software, 2003), where 2D model sections of chargeability were generated, with the addition of data from topography. The Res2dinv is a 2D inversion software, which automatically defines a bi-dimensional model of the subsurface (in terms of distance versus approximate vertical depth) from resistivity and IP data, obtained from geoelectrical surveys (Griffiths & Barker, 1993).

The 2D model sections were then exported from Res2dinv and re-imported into the Oasis Montaj Platform (Geosoft), in order to create a 3D visualization model for the chargeability, without adjustment of topographic data. 3D visualization models generated from geophysical data are of great help in the understanding of complex geological structures and hydrological problems, like the flow of pollutants and modeling of ore deposits

(Chambers *et al.*, 2006; Aizebeokhai *et al.*, 2011; Moreira *et al.*, 2012). The visualization model was created interpolating the IP data from each section, using the Minimal Curvature algorithm.

Discussion

The data presented in terms of pseudosections feature areas of high chargeability in the central portion, with a tendency of continuity subvertical and reduction of values with the increase of depth (Figure 3). This pattern is accentuated in sections calculated with highlight of central areas and outlining a flank of high values toward the end of the lines are joined on-site deleted in inversion models.

The maximum depth obtained in pseudo-sections was 70m. The maximum depth after the process was 85m, defined in the form of automatic during the processing, before the unavailability of direct data for calibration, as testimonials or contacts geological outcropping.

The IP data revealed a low chargeability pattern for the investigated area as a whole. Apart from its central portion, where high chargeability values were detected in the lines 4 and 6, the average chargeability rarely overcomes 8mV/V. The lines 4 and 6, in the central portion of the area, showed significant IP anomalies in their central-eastern parts, characterized by chargeability values higher than 20mV/V, which were correlated to the manganese ore (Figures 4A and 4B).

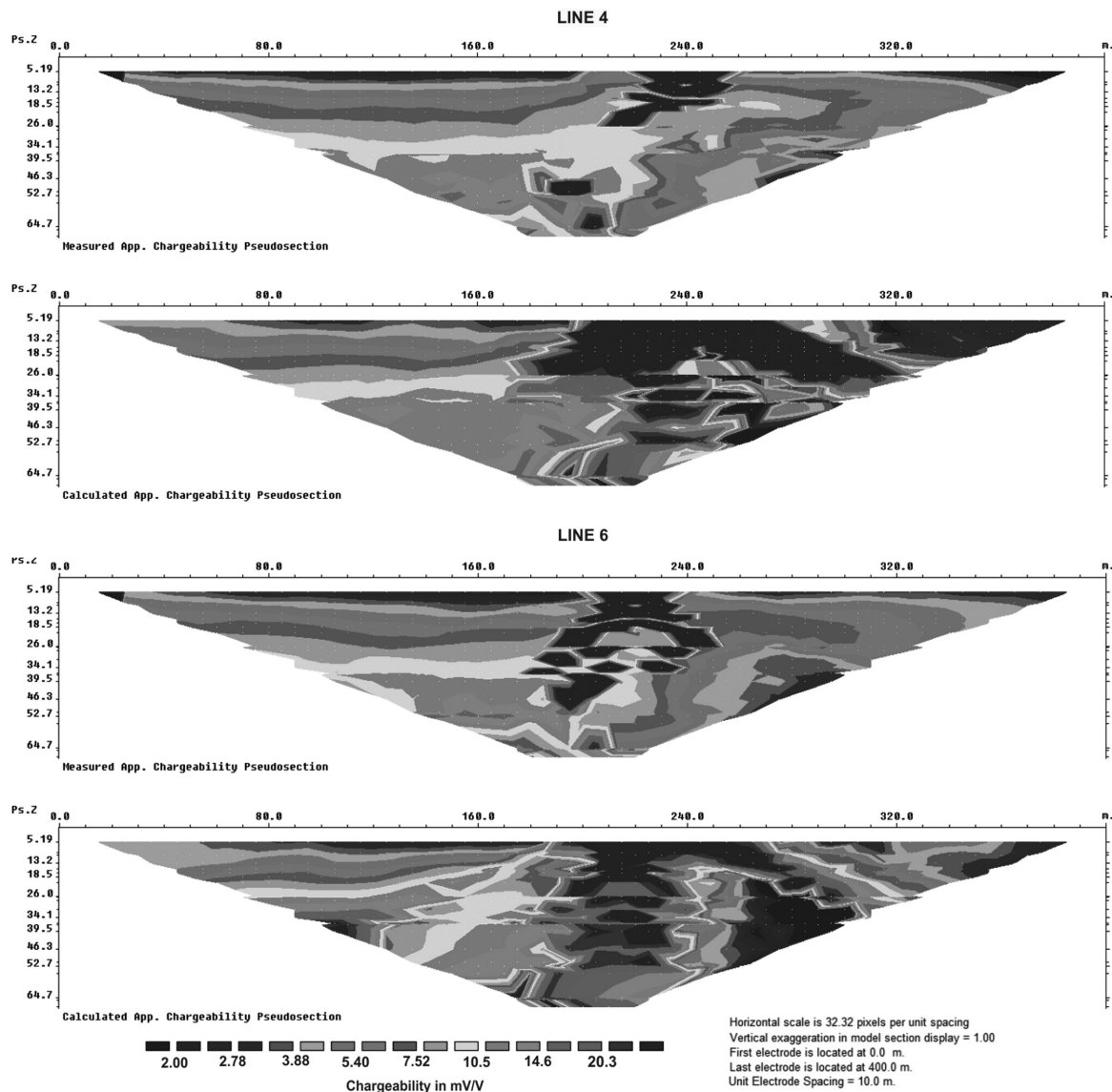


Figure 3. Pseudosections and calculated sections of the chargeability for lines 4 and 6.

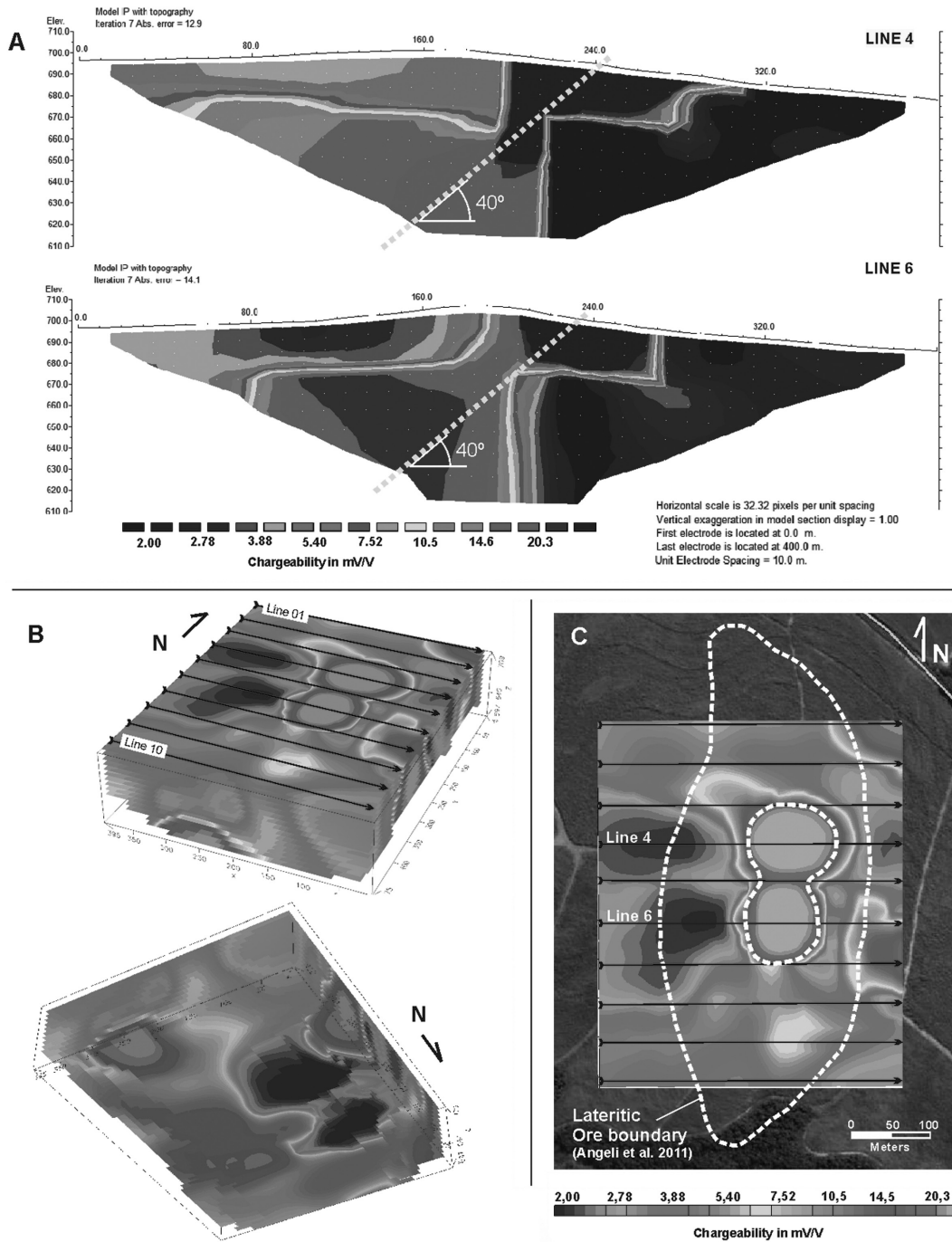


Figure 4. A) Most representative 2D model sections of chargeability; B) 3D Voxel model of chargeability, with top and bottom view for northwest; C) Discrepancy in area between the mapped lateritic ore and the near surface ore (about 3 m deep).

The errors of adjustment in both sections (12.9 and 14.1) reflect the standard deviation or variability of the data in relation to the average of the values. The high chargeability areas, presented in sections 4 and 6, have good vertical continuity into the deeper portions, with no end in sight, based on structural data

obtained in the field, although it could be considered some smoothing effect during the data processing. The anomalies, which are coincident with the manganese lateritic cover in the surface, extend at least 50 m down-plunge towards the west at angles of about 40° (Figure 4A).

When projected to the surface, the central anomalies define an area much smaller than that of the manganese ore capping mapped and recognized during the geophysical survey (Figure 4C). A possible explanation for the discrepancy between the mapped occurrence in the field and the modeled geophysical orebody can be presented in terms of survey configuration. The 10 m electrode spacing used in the data acquisition resulted in a 2D modeled section with a minimum investigation depth of about 3 m, which is possibly deeper than the lower limit of the lateritic cover, with a maximum thickness of 1m verified in the field. Therefore, the high chargeability values are possibly related to the primary ore, instead of being related to the ore capping itself.

Finally, an isosurface was created based on the IP voxel model with the aim of evaluating the morphology of the high chargeability zones (values above 20mV/V) and their correlation with the deep mineralization (Figure 5).

The chargeability isosurface revealed the existence of two independent orebodies in the subsurface, instead of a single one elongated parallel to the regional strike (NNE) as suggested by the boundaries of the lateritic cover. Also, the isosurface showed a good vertical continuity of the orebodies at least to a depth of 80 m below surface, with a dip of about 40° to the WNW direction.

The orebodies are elongated along a WNW-ESE direction, therefore roughly perpendicular to the area main structural trend and the regional alignment of the lateritic occurrences. A possible explanation for this is that the orebodies were most likely originated previously to the last deformational event that culminated with the generation of the synform and antiform structural pattern with fold axis striking NE-SW.

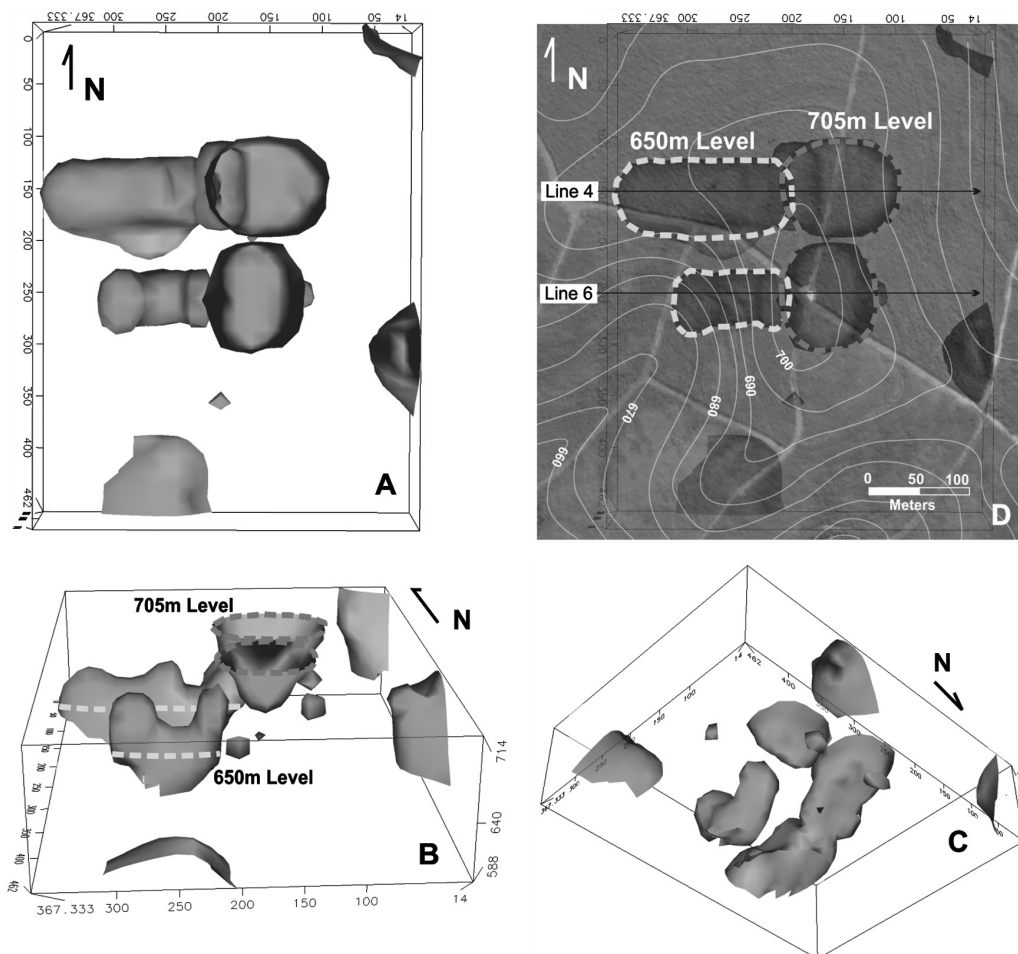


Figure 5. High chargeability isosurface models: A) View from top; B) View from side; C) View from below (the structure remain open). D) Surface projection of the underground orebodies.

Conclusion

The IP method showed good efficiency in the reconnaissance and morphological characterization of the orebodies in subsurface, mainly due to the presence of disseminated graphite (up to 5%) in the lateritic/manganese ore and protore, besides the Mn oxides and hydroxides, essentially due to the presence of graphite in the ore, because the polarization of oxides is very low.

These results demonstrate the applicability of the geophysical ground methods, specially the IP, as a support tool in the identification and selection of exploration targets for test drilling. The use of relatively inexpensive tools for the identification and selection of best drilling location can be a good strategy for saving time and money in mineral exploration projects.

Lateritic manganese ore cappings are key elements in the reconnaissance phases in regional mineral exploration, as they are easily identified in the field due to their characteristic black color. However, their great areal extent in the field as the result pedogenetic processes often lead to miscalculations on the resources and reserves of the concealed primary deposits.

The 3D visualization model was very important for delimitating both the areal extent and depth continuity of the concealed primary deposits, hidden below the lateritic surface. In addition, the 3D model was fundamental for the individualization and morphological characterization of the two orebodies in subsurface, dislocated from the central region of the lateritic cover and elongated perpendicular to the main regional structural trend.

The presence of graphite in the ore and protore was considered crucial for the success in the applicability of the IP method, due to its high polarizability in relation to the host rocks, which are quartz-feldspatic in composition. The genesis of the graphite is related to the origin of the manganese ore in a marine environment, under strong reducing conditions that allowed for the preservation of the dissolved organic matter in the sediments. Regional deformational and metamorphic events resulted in the conversion of the organic matter into graphite and in the generation of the gondites, which did supergene enrichment processes then concentrate.

The orientation of the orebodies in subsurface, contrary to the main structural trend, brings new possibilities for the revaluation of the several other manganese

occurrences in the area through geophysical investigation. The IP method revealed to be a very efficient tool for the characterization and 3D modeling of the manganese orebodies in subsurface, in aid on the target location for direct sampling and chemical analysis.

Acknowledgement

The authors are thankful to Fundação de Amparo à Pesquisa do Estado de São Paulo (FAPESP), for financial support of the project "Geophysical prospection in supergenic manganese occurrence in Natércia region, Minas Gerais Southern" (Processs FAPESP no 2013/09219-5).

References

- ABEM, 2012, Terrameter LS - Instruction Manual, 122pp.
- Allis R.G., 1990, Geophysical anomalies over epithermal systems. *Journal of Geochemical Exploration*, 36, 339-374.
- Aizebeokhai AP., Olayinka A.I., Singh V.S., Uhuegbu C.C., 2011, Effectiveness of 3D geoelectrical resistivity imaging using parallel 2D profiles. *International Journal of the Physical Sciences*, 6, 5623-5647.
- Angeli N., Khan H., Ito G.M., Carvalho S.G., Jimenez-Rueda J.R., Penha U.C., 2011, Geologia e caracterização tecnológica do minério de manganês da mina Córrego do Cocho, Itapira (SP). *Geologia USP, Série Científica*, 11, 107-130.
- Artur A.C., 1980, Rochas metamórficas dos arredores de Itapira, SP. Master of Science Dissertation, Universidade de São Paulo, São Paulo.
- Artur A.C., Wernick E., Kawashita K., 1979, Dobramentos Superimpostos na Região de Itapira (SP): Caracterização e Cronologia. Atas do II Simpósio de Geologia Regional, SBG, 58-70.
- Campos Neto M.C., 1991, A porção ocidental da Faixa Alto Rio Grande: ensaio de evolução tectônica. Doctoral Thesis, Universidade de São Paulo, São Paulo.
- Chambers J.E., Kuras O., Meldrum P.I., Ogilvy R.D., Hollands J., 2006, Electrical resistivity tomography applied to geologic, hydrogeologic, and engineering investigations at a former waste-disposal site. *Geophysics*, 71, 231-239.

- Dahlin T., Zhou B., 2004, A numerical comparison of 2D resistivity imaging with 10 electrode arrays. *Geophysical Prospecting*, 52, 379–398.
- Dentith M., Mudge S.T., 2014, Geophysics for the mineral exploration geoscientist. Cambridge University Press, New York, 516pp.
- Dentith M., Barrett D., 2003, Geophysical exploration for graphite at Uley, South Australia. ASEG Extended Abstracts, 47–57.
- Fiori A.P., Wernick E., Choudhuri A., Soares P.C., Bettencourt J.S., 1978, Evolução Policíclica na região Nordeste do Estado de São Paulo e áreas vizinhas do Estado de Minas Gerais. Anais do XXX Congresso Brasileiro de Geologia, Recife, 309–320.
- Fiori A.P., Wernick E., Choudhuri A., Soares P.C., Bettencourt J.S., 1980, Evolução Geológica da parte SW do Estado de Minas Gerais. Anais do XXXI Congresso Brasileiro de Geologia, Camboriú, 2893–2905.
- Ford K., Keating P., Thomas M.D., 2007, Overview of geophysical signatures associated with Canadian ore deposits. In: Mineral Deposits of Canada: A Synthesis of Major Deposit-Types, District Metallogeny, the Evolution of Geological Provinces, and Exploration Methods: Geological Association of Canada, Mineral Deposits Division, Special Publication, 939–970.
- Geotomo Software, 2003, RES2DINV, version 3.53, Rapid 2D resistivity & IP inversion using the least-square method - Geoelectrical Imaging 2-D & 3D, Geotomo Software, Penang, Malaysia, 129pp.
- Gonçalves E., Serfaty A., 1976, Perfil analítico do manganês. Ministério das Minas e Energia, Departamento Nacional da Produção Mineral, Rio de Janeiro, 149pp.
- Griffiths D.H., Baker R.D., 1993, Two-dimensional resistivity imaging and modeling in areas of complex geology. *Journal of Applied Geophysics*, 29, 211–226.
- Guilbert J.M., Park Jr C.F., 2007, The geology of ore deposits. Waveland Press Inc., New York, 985pp.
- Hasui Y., Oliveira, M.A.F., 1984, Província Mantiqueira – Setor Central. O Pré-cambriano do Brasil, Edgard Blücher, São Paulo, p. 308–344.
- Irvine R.J., Smith M.J., 1990, Geophysical exploration for epithermal gold deposits. *Journal of Geochemical Exploration*, 36, 375–412.
- Izawa E., Urashima Y., Ibaraki K., Suzuki R., Yokoyama T., Kawasaki K., Koga A., Taguchi S., 1990, The Hishikari gold deposit: high-grade epithermal veins in Quaternary volcanics of southern Kyushu, Japan. *Journal of Geochemical Exploration*, 36, 1–56.
- Keller G.V., Frisknecht F., 1970, Electrical Methods in Geophysical Prospecting. Pergamon Press, New York, 576pp.
- Langore L., Alikaj P., Gjovreku D.H., 1989, Achievements in Copper Sulphide Exploration in Albania with IP and EM methods. *Geophysical Prospecting*, 37, 975–991.
- Lazarini A.P., 2000, Petrologia de metabasitos e ultrabasitos da região de Águas de Lindóia. Master of Science Dissertation, Universidade Estadual Paulista, Rio Claro.
- Locke C.A., Johnson S.A., Cassidy J., Mauk J.L., 1999, Geophysical exploration of the Puhupuhi epithermal area, Northland, New Zealand. *Journal of Geochemical Exploration*, 65, 91–109.
- Loke M.H., Baker R.D., 1996, Rapid least-squares inversion of apparent resistivity pseudosections by quasi-Newton method. *Geophysical Prospecting*, 131–152.
- Marjoribanks R., 2010, Geological methods in mineral exploration and mining. 2^oed., Springer, Heidelberg, 248pp.
- Maynard J.B., 2003, Manganiferous sediments, rocks and ores. *Treatise on Geochemistry*, Elsevier, Oxford, 289–308
- Milsom J.J., Eriksen A., 2011, Field Geophysics. John Wiley & Sons Ltd, Chichester, 297pp.
- Misra K.C., 1999, Understanding mineral deposits. Kluwer Academic Publishers, Dordrecht, 864pp.
- Ministry of Mines and Energy – MME. Sumário Mineral 2014, Departamento Nacional da Produção Mineral, Brasília, 152pp.
- Moon C.J., Whateley M.K.G, Evans A.M., 2006, Introduction to mineral exploration. Blackwell Publishing, Malden, 499 pp.

- Moreira C.A., Lopes S.M., Schweig C., Seixas A.R., 2012, Geoelectrical prospecting of disseminated sulfide mineral occurrences in Camaquã Sedimentary Basin, Rio Grande do Sul State, Brazil. *Revista Brasileira de Geofísica*, 30, 169-179.
- Moreira C.A., Borges M.R., Vieira G.L., Malagutti Filho W., Fernandes M.M.A., 2014, Geological and geophysical data integration for delimitation of mineralized areas in a supergene manganese deposits. *Geofísica Internacional*, 53, 199-210.
- Park C.F.Jr., MacDiarmid R.A., 1975, Ore Deposits: 3^o edition, W.H. Freeman and Company, San Francisco, 529 pp.
- Pelton W.H, Smith P.K., 1976, Mapping porphyry copper deposits in the Philippines with IP. *Geophysics*, 41, 106-122.
- Peters W.C., 1987, Exploration and mining geology. John Wiley and Sons Inc., New York, 706pp.
- Polgári M., Gutzmer J., 2012, Manganese metallogenesis: introduction to the special issue. *Ore Geology Review*, 47, 1-4.
- Ramazi H., Mostafaie K., 2013, Application of integrated geoelectrical methods in Marand (Iran) manganese deposit exploration. *Arabian Journal of Geosciences*, 6, 2961-2970.
- Reedman J.H., 1979, Techniques in mineral exploration. Kluwer Academic Publisher, London, 533pp.
- Robinson, E.S., 1988, Basic Exploration Geophysics. John Wiley & Sons Inc., New York, 576pp.
- Roy S., Mitra F.N., 1964, Mineralogy and genesis of the gondites associated with metamorphic manganese ore bodies of Madhya Pradesh and Maharashtra, India. *Proc. Nat. Inst. Sci. India*, 30, 395-439.
- Roy S., 1992, Environmental and processes of manganese deposition. *Economic Geology*, 87, 1218-1236.
- Sethumadhav M.S., Gunnell Y., Ahmed M.M., 2010, Late Archean manganese mineralization and younger supergene manganese ores in the Anmod-Bisgod region, Western Dharwar Craton, Southern India: Geological characterisation, palaeoenvironmental history, and geomorphological setting. *Ore Geology Review*, 38, p. 70-89.
- Silva L.C., Mcnaughton N.J., Armstrong R., Hartmann L.A., 2005, Fletcher, I. R. The Neoproterozoic Mantiqueira Province and its African connections: a zircon-based U-Pb geochronologic subdivision for the Brasiliano/Pan-African systems of orogens. *Precambrian Research*, 136, 203-240.
- Stanton R., 1972, Ore Petrology. McGraw-Hill, New York, 713pp.
- Tassinari C.C.G., Campos Neto M.C., 1988, Precambrian continental crust evolution of southeastern Sao Paulo state-Brazil: based on isotopic evidences. *Geochemica Brasiliensis*, 2, 175-183.
- Taylor, R. 2011. Gossans and Leached Cappings – Fields Assessment. Springer-Verlag, Heidelberg, 165 pp.
- Veríssimo C., 1991, Evolução geológica dos corpos de protominério e mineralizações de manganês associadas, porção leste de São Paulo e Sul de Minas Gerais. Master of Science Dissertation, Universidade Estadual Paulista, Rio Claro.
- Zanardo A., 2003, Pesquisa geológica e de matérias primas cerâmicas do centro nordeste do estado de São Paulo. Doctoral Thesis, Universidade Estadual Paulista, Rio Claro
- Wernick E., Fernandes N.A., Almeida Jr N.F., 1976, Gonditos de Socorro e Itapira, SP. *Mineração e Metalurgia*, 39, 372-379.
- Wolf K.H., 1976, Handbook of strata-bound and strati-form ore deposits: principles and general studies, supergenic and surficial ore deposits. *Elsevier Science*, Amsterdam, 763pp.

Comparative analyzes among electrical resistivity tomography arrays in the characterization of flow structure in free aquifer

César Augusto Moreira, Marcelo Montenegro Lapola and Alan Carrara*

Received: May 11, 2015; accepted: November 27, 2015; published on line: April 01, 2016

Resumen

En este trabajo se hace un análisis comparativo entre los arreglos Dipolo-dipolo, Wenner e Schlumberger por medio de pruebas de Tomografía de Resistividad Eléctrica (TRE), como la sensibilidad y la resolución en la caracterización espacial de la infiltración de contaminantes en un tanque séptico y cono de depresión en el pozo de captación de agua; ambos contenidos en acuífero libre. La adquisición de datos consistió en lecturas de resistividad utilizando cinco líneas paralelas con 105 m de largo espaciado, 5 m entre los electrodos y líneas. Los datos de cada línea se sometieron a la inversión 2D, posteriormente interpolado para la generación de bloques 3D, de la cual se extrajo una isosuperficie de resistividad fija (620 Ω .m), lo que permitió el modelado de las estructuras de volúmenes de flujo relacionados. Los resultados para el arreglo Dipolo-dipolo permite el modelado de la estructura asociada con el eje cilíndrico, y un isosurface de la cavidad asociada con la deformación, pero que no permitirá que el modelado de la pluma. Los datos para la disposición Schlumberger no pueden ser reconocidos cono, pero dieron lugar a un modelo de forma de lágrima asociado con el tanque séptico, como una pluma de contaminación. El arreglo Wenner resultó en un modelo con estructura en formato de quilla alargado asociado con el cono de depresión, y uno en formato caída similar también asociado con el tanque séptico. El análisis comparativo muestra que la disposición Dipolo-dipolo se recomienda en las obras de modelado de estructuras tridimensionales de alta resistividad verticales en la zona saturada. La disposición Wenner y Schlumberger se recomiendan en estructuras de modelado en tres dimensiones verticales de baja resistividad en zona no saturada, con énfasis en la disposición Schlumberger.

Palabras clave: Dipolo-dipolo, Schlumberger, Wenner, pluma de contaminación, cono de depresión.

Abstract

This paper makes a comparative analysis between the Dipole-dipole, Wenner and Schlumberger arrays through electric resistivity tomography (ERT), about the sensitivity and resolution in the spatial characterization of infiltrating pollutants in septic tank and cone of depression in supply well, both contained in unconfined aquifer. Data acquisition consisted of electrical resistivity readings using five parallel lines with 105m long, electrode spacing and lines of 5m. The data from each line were subjected to 2D inversion and then interpolated to generate 3D blocks, which were extracted from a fixed resistivity isosurface (620 Ω .m), which enabled the modeling of volumes related to the flow structures. The results for the Dipole-dipole array allowed the modeling of the cylindrical structure associated to the supply well, and an isosurface deformation associated to the septic tank, but did not allow the modeling of the plume. The data for the Schlumberger array cannot allow for the cone recognition, but resulted in a drop shape model, associated to the septic tank and similar to a contamination plume. The Wenner array resulted in a model with structure in elongated keel format associated to the cone of depression, and another that is similar to the drop shape model, also associated to the septic tank. The comparative analysis shows that the Dipole-dipole array is recommended in works of modeling vertically integrated three-dimensional structures of high resistivity in the saturated zone. The Wenner and Schlumberger arrays are recommended for modeling vertically integrated three-dimensional structures of low resistivity in unsaturated zone, with emphasis on the Schlumberger array.

Key words: Dipole-dipole, Schlumberger, Wenner, contamination plume, cone of depression.

C. Augusto Moreira
Applied Geology Department

M. Montenegro Lapola
Graduation in Physics

A. Carrara*
Graduation in Environmental Engineering
Geoscience and Exact Science Institute
Univ. Estadual Paulista, UNESP, Rio Claro Campus
24-A Avenue, 1515, PO box 178 – ZIP 13506-900
São Paulo State, Brazil
*Corresponding autor: alancarrara05@gmail.com

Introduction

The availability of hydric resources is something that requires growing attention by public management, in face of the demand increase and the even more restrict offer in terms of quality, availability and flows enabled by superficial hydric resources.

In face of the Brazilian hydric potential, its energetic matrix is historically based in the generation of electricity in ramps enabled by dams, which, among many other aims, also represent an available resource to public service (MME, 2013). Under a context of long drought periods, as in the case of the present Southwest Region of Brazil, it is natural the emergence of a standstill about the energetic needs and public supply.

In other view, it is still incipient the adoption of measures that aim to mitigate questions like the wastage in leakages in distribution lines, clandestine connections or the reuse of water coming from the waste treatment in distribution lines in specific activities. This set of factors, allied to the present hydric crises, indicates a scenario of energetic rationing and of public supplying.

The underground hydric resource is always an alternative considered in many cases, preferably in cities where the superficial resource availability is scarce or in a way to supplement the superficial capture (Balek, 1989). Particularly relevant in economic terms, underground capture is a growing resource in the capture by industries, agriculture, and in cases of communities distant from distribution networks (Hiscock, 2005; Elgzeli *et al.*, 2013).

The absence or scarcity of collection and treatment systems of sewage and liquid effluents and their direct throwing in rivers and lakes results in a direct impact of this superficial resource. However, in places where this procedure is economically unfeasible, the use of septic tanks is a very used alternative (Nemerow *et al.*, 2009). The little visibility of this procedure and the hypothesis of depuration by filtering enabled in the geological environment, results in its indiscriminate use and not provided of any planning or technical procedures (König & Weiss, 2009).

The load of pollutants eventually present in streams and rivers is much attenuated in rainy periods, where the increase in flows enables for the dilution of liquid effluents and the increase in the outflow speed. However, the input of

this kind of pollutant in soil and aquifers be it in accidental or purposeful form, results in long-term impacts due to the resident term by the infinitely lower speed in this environment (Peirce *et al.*, 1998; Sara, 2003).

Obviously, it is essential the use of technical procedures that impair this kind of affect, besides the development and improvement of technologies that enable the diagnosis and the monitoring of ongoing situations (Lehr *et al.*, 2001; Twardowska *et al.*, 2005; Hernández-Soriano, 2014).

The use of geophysical methods is a rational possibility in this context. In face of factors like indirect measuring of physical factors that can be altered in face of the presence of pollutants in soil and underground water, wide coverage for investigation in spatial terms and the possibility of monitoring in a fast way at a relatively low cost, when compared to traditional techniques like installation and sampling of monitoring wells. (Knödel *et al.*, 2007; Sara, 2003).

In this sense, the present work presents and discusses the results of the application of the geophysical method of electro resistivity, in an area with septic well upward an underground catchment well for public service. In this place, Electrical Resistivity Tomography (ERT) essays were performed in Dipole-dipole, Wenner and Schlumberger arrays. The main aim is an analysis of the most adequate array in terms of sensibility and resolution, in the detections of pollutants infiltrated in septic tanks and the identification of the depression cone in underground capturing systems.

Area of studies

The geophysical collection data was developed in the campus of the Universidade Estadual Paulista – UNESP, in the city of Rio Claro (SP), 190 km to the southwest of the state capital. The place consists in a terrain attached to a set of three didactic buildings with about 10 years of built, from where all water coming from restrooms was piped and conducted by gravity to a septic well located in the NW end of the site. About 5 years ago, a series of drillings and the installation of a interlinked chain of underground collection wells, among all these is a well located at 40m downstream the septic well, in the SSW direction (Figure 1).

In physiographic terms, Rio Claro is included in the São Paulo Peripheral Depression, geomorphologic unit characterized by lowered

terrains and altitudes between 500 m and 700 m. The raising geological unit in the area of studies is the Rio Claro Formation, which in this region, presents an approximate thickness of 20 meters, placed beneath by siltstone of Corumbataí Formation and locally intruded by dams and sills of diabase related to the event Serra Geral (Oliva *et al.*, 2005).

The Rio Claro Formation is made up of Neocenoic deposits and is part of a set of units that cover large areas of the State, which occur in sloped levels in the relief and linked to planning phases. The work of Melo *et al.* (1997) proposes the division of this unit in four great lithofacies in the basis of granulometric and textural criteria. The laminate bed is originated from gravitational processes, gravel and sand from channels and river estuaries, fine sandstone occurring from the breaking of marginal dams and sedimented argillites in flooded plain areas. This set covers a basal horizon made up of conglomerates derived from erosion processes of the substrate during the initial phases of deposition of this unit, with emphasis to the Corumbataí Formation (Oliva & Chang, 2007).

This unit is characterized as a free aquifer in the region of Rio Claro, with high elevated transmissivity (upper 50 m²/day) and wells with outflow of between 17m³/h and 25 m³/h. A second system of confined aquifer is represented by lithotypes of the Tubarão Group, with depths over 200 m and flow between 20 m³/h and 37 m³/h (DAEE, 1981).

In the area of studies, the Rio Claro Formation is represented by soil of arenite alterations, with predominance of fine to medium sand fraction. Based on the descriptive profile of the supply well in the site of studies, the first 10 m deep are constituted by a low consolidated arenite and of silt matrix, with sandy fractions absent of fine matrix below this depth.

This well is 20 m deep and presented a groundwater level positioned at 12.3 m during the performance of the geophysical essays, with a production of 8 m³/h. The studies developed by Oliva *et al.* (2005), a few tenths of meters from the site of studies, revealed values of hydraulic conductivity for 2 m depth of $9,6 \times 10^{-3}$ cm/s and of 6×10^{-3} cm/s for 14 m depth (saturated zone).

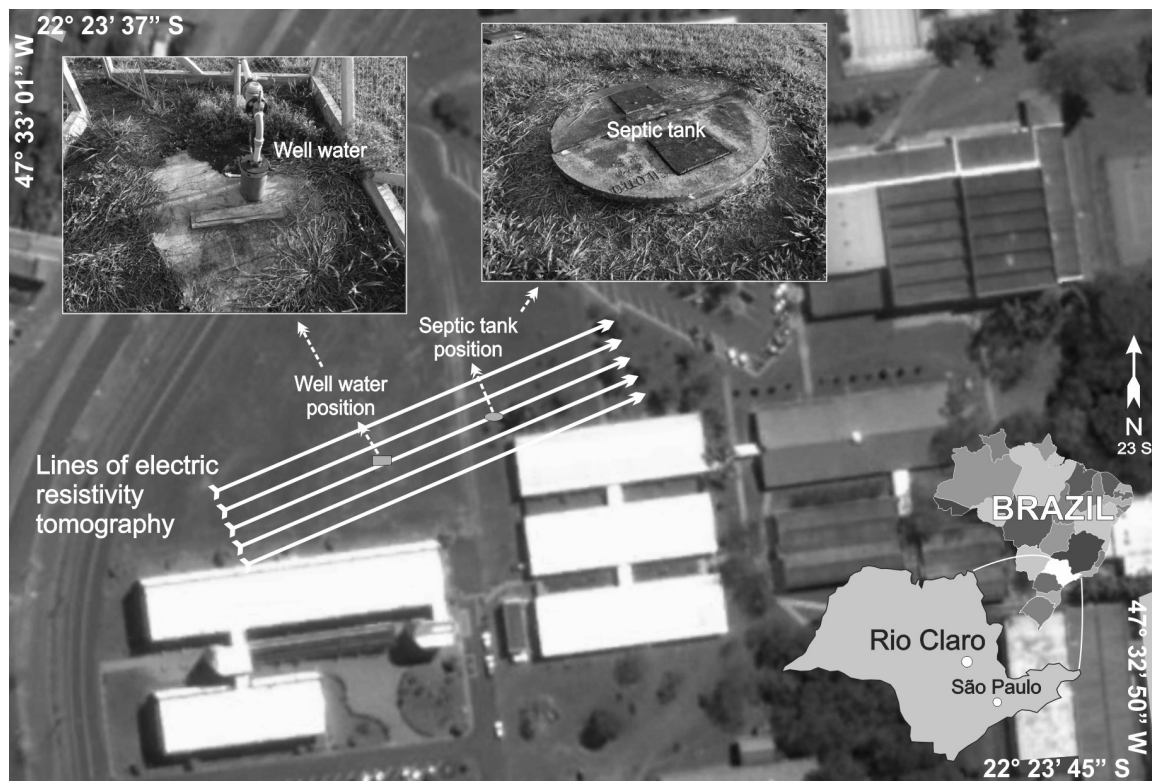


Figure 1. Location of the area of studies, with lines of the electrical resistivity tomography lines and detaching the investigated targets.

The septic tank located in the area of studies is 2 m in diameter and 3 m in depth, with a lining of concrete piping and open base, enabling the filtering of effluents directly into the soil. The area of studies has very plane topography, with a slope of approximately 1° in the SW direction of the area

Materials and methods

The acquisition of data in the field consisted in the performance of electrical resistivity readings applying the electrical tomography (ERT), in 5 lines of investigation with individual length of 105 m and spacing between electrodes of 5m, placed parallel and separated 5 m each (Figure 1).

The septic tank and the supply well, targets of the studies in this research, were placed in the center of this data acquisition scheme, with the aim of detecting eventual lateral alterations or in depth, related to the infiltration of effluents or by the artificial lowering of the aquifer, respectively.

In this work, acquisitions from Dipole-dipole, Wenner and Schlumberger arrays were performed (Figure 2), for the comparative

evaluation of the individual sensibility and possibility of modeling of the contamination plume generated by infiltration of inorganic effluents of the septic tank and of the depression cone in supply well.

The geophysical equipment used was the Terrameter LS resistivity meter, manufactured by ABEM Instrument (Sweden), which consists in a single module of transmission and reception of signals, automated from previous programming, with 250 W, resolution of 1 μV and maximum current of 2,5 A. It enables the performance of spontaneous potential essays (SP), electro resistivity (ER) and induced polarization (IP) by means of periodic cycles of transmission and reception of signals, automated calculation of the contact resistivity and standard deviation from the measurement set.

The measurements acquired in the field were processed in the Res2dinv program and resulted in sections of resistivity in terms of distance x depth, with a logarithmic graphic scale and interpolation intervals of values in colors. This is a program that automatically determines a two-dimensional model of

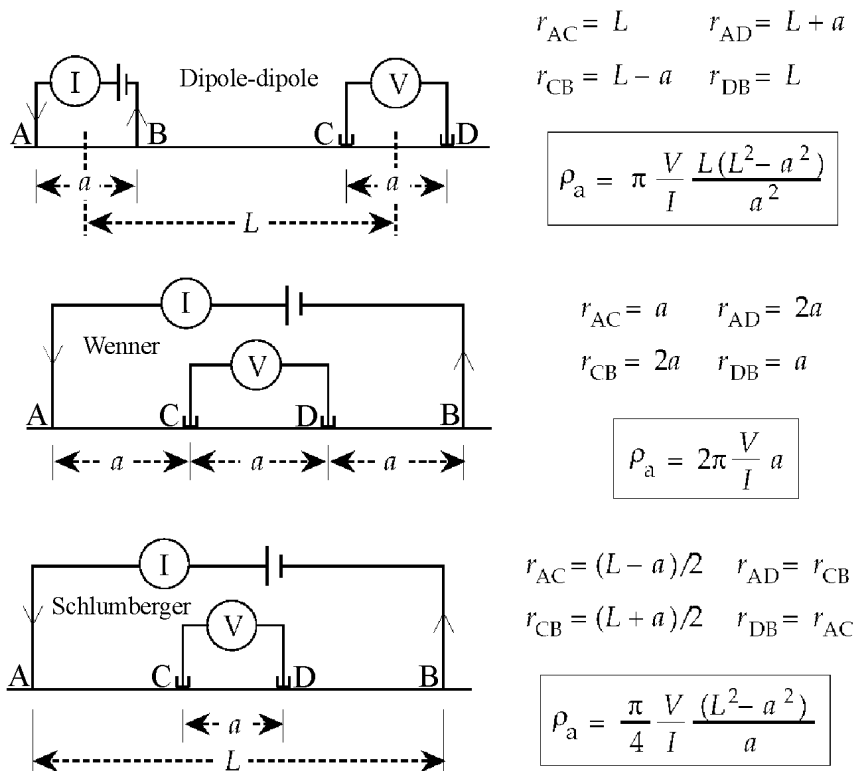


Figure 2. Dispositions of current and potential electrodes for the Dipole-dipole, Wenner and Schlumberger array (Lowrie, 2007).

subsurface, from resistivity or chargeability data acquired in electrical routing essays (Griffiths & Barker, 1993).

The 2D model used in the program divides the pseudo-section in rectangular blocks that will represent the pseudo-section by the field adjustments. This optimization aims to reduce the difference between the values of apparent resistivity, calculated and measured in the field, by the adjustment of the resistivity in the model of blocks, which difference is expressed by the RMS (Root Mean Square) error (Loke & Barker, 1996).

The numeric product of two-dimensional inversion of data of each section was gathered in a single spreadsheet, which unites the position of the readings along the lines (variable "x"), spacing among lines (variable "y"), depth modeled by the inversion (variable "z") and the value of electrical resistivity (variable "R").

This spreadsheet was used for the generation of 3D viewing models, in a routine of basic steps adopted in mineral research. In this case, the sampling plan is frequently defined from statistic, structural criteria, spatial placement of a mineral accumulation, among other (Moon *et al.*, 2006). A simple procedure consists in sampling by a set of perforations perpendicular to the main axis of the structure, followed by a parallel set of perforation lines.

The resolution of the sampling mesh is conditioned to the spacing among the perforations, among lines of perforations and among the amount of samples collected in each perforation. Anyway, the analytical result of the samples is plotted and modeled in two-dimensional terms and later interpolated in three-dimensional terms. Each point of the final 3D model is transformed in a block, with dimensions conditioned to statistical criteria and sampling mesh, to which a grade is attributed, based in chemical analysis and in an average value of density related to the rock that hosts the mineral. The relationship between content and volume enables the calculation of reserves and economic feasibility of the enterprise (Moon *et al.*, 2006).

Geophysical models of 3D viewing generated from 2D sections provide a very wide comprehension of the complexity of geological and hydrogeological structures, as the pollutant flow and the modeling of lithotypes or mineral deposits (Chambers *et al.*, 2006; Aizebeokhai *et al.*, 2011; Moreira *et al.*, 2012).

Results and discussions

Based in the principle of direct sampling in mineral research, the sampling mesh of geophysical data was planned with the aim of lateral interpolation of lines from 2D inversion models, by means of the minimum curvature, with the aid of the Oasis Montaj software, for the generation of 2D horizons or softening surfaces for several depths.

From the blocks with interpolated resistivity surfaces, isovalues resistivity surfaces were modeled for each block, representative of an acquisition array, which would reveal the structures studied in this paper (contamination plume and depression cone). The value of 620 $\Omega.m$ was adopted as the most adequate in individual terms and for comparative terms, which corresponds approximately to the capillary fringe of the free aquifer.

The analysis of resistivity models must consider the behavior of the analyzed structures in terms of contrast of resistivity in relation to the soil.

The effluent arising from the septic tank is chemically characterized in a simple form as inorganic compound, enriched in mineral salts (ammonia, nitrates) and solute organic matter (faeces) (Sara, 2003). The basal interface of the septic tank allows for the direct contact with the soil, where filtering of organic mass an infiltration of water in mineral salts occurs. Their flow into sandy material with incipient humidity results in a contrast and low resistivity values (Figure 3).

The pumping out of the water from the supply well causes a localized decrease in the groundwater level in the influence area of the well, namely depression cone (Fitts, 2002). The sandy material contained in the inner portion of this structure is relatively drier when compared to the material laterally present in the outer portion, which results in a contrast and high resistivity values (Figure 3).

The analysis of the data regarding the Dipole-dipole array clearly reveals a cylindrical structure of open upper extremity, indicating the increase in resistivity from the borders to the center, placed beneath the supply well (Figure 4). This structure shall be produced by the depletion of the aquifer level around the influence zone of the suction pumping system. Associated to the septic tank, there are also alterations in resistivity, although they do not enable the surface modeling with any

relation to the flow of liquids of low resistivity in sandy environment or something similar to a contamination plume.

The data related to the Schlumberger array do not present any structure that brings reference to the depression cone of the supply well (Figure 5). The conic structure modeled below the position of the septic tank probably reflects the infiltration of effluents of low resistivity. The upper end of the cone is closed, indicating an increase in resistivity above that depth, and coincides with a punctual source (base of the tank), whereas its lower end presents a relatively smaller diameter, a reflex of the vertical and lateral percolations of effluents until the contact with groundwater level, under the form of a drop in tridimensional terms.

The isosurface for the Wenner array resulted in the modeling of a long structure towards the data acquisition of the central line and narrow right below the supply well, tending to close in depth, indicating an increase of resistivity in its central part (Figure 3). A conic structure also occurs below the septic tank, to which the same interpretations attributed to the Schlumberger array are valid in face of the similarities, although in this case the structure is less pronounced vertically.

Intrinsic characteristics in terms of electric field and potential propagation produced by the use of each array can be used to understand the comparatively discrepant results in relation to the same targets investigated.

The Dipole-dipole array of characterized by the increasing separation between electrodes or dipoles of current and potential (Mussetti & Khan, 2000). Several papers describe its applicability in the study of organic and inorganic contaminations in saturated zone conditions, proved by chemical analysis (Moreira *et al.* 2006; Arango-Galván *et al.*, 2011; Belmonte-Jiménez *et al.*, 2012; Delgado-Rodríguez *et al.*, 2014).

In Nyquist *et al.* (2007), the authors demonstrate the lack of sensibility in the Dipole-dipole array by means of 2D sections, in the detection of a zone of verticalized fault filled with water, later confirmed by probing. This array was very susceptible to noises in detailed study performed by Furman *et al.* (2003), due to its high sensibility in shallow levels, where spacing below 1m was adopted between electrodes.

Something inherent to this array is the lateral distortion in the field and potential propagation under small separations of

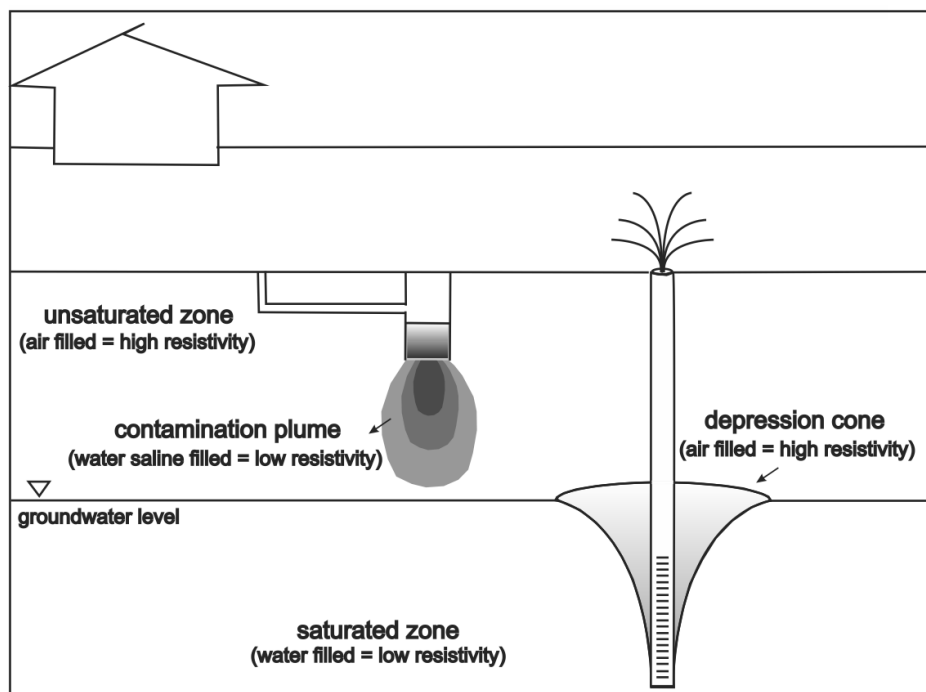


Figure 3. Model of gravitational dispersion of contamination plume arising from septic tank and depression cone in supply well (Based in Sara, 2003).

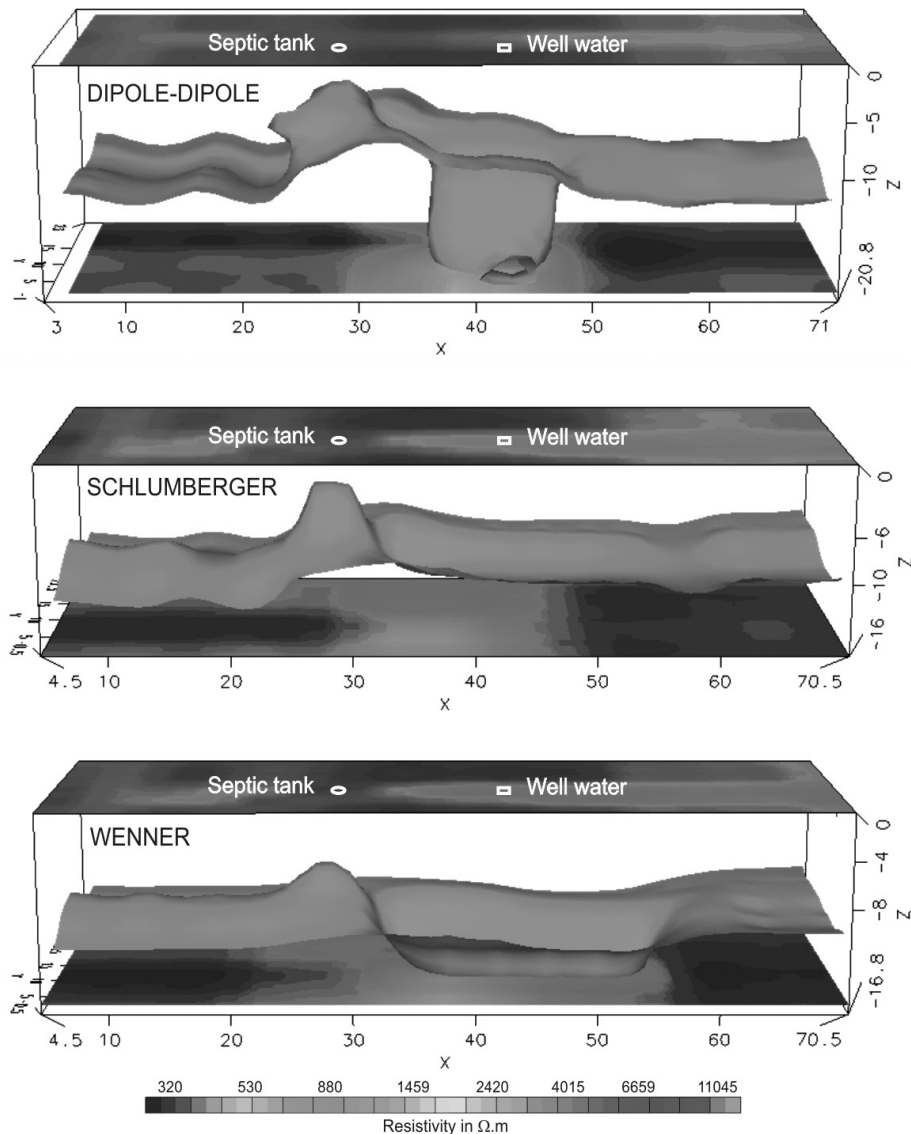


Figure 4. 3D Surfaces of isovalues of 620 W.m for the acquisition arrays in study, with position in the surface of the septic tank and of the supply well (distances in meters).

electrodes (shallow investigations). This tendency is attenuated as the spacing between dipoles increase, although at the same time there is a reduction in sensibility or signal/noise rate (deep investigations). In both cases, the main flow vector tends to be horizontal under small separations of electrodes, with gradual tendency to verticalization under large separation of electrodes (Figure 5).

About the depression cone around the supply well, lateral limits with the aquifer are sloped in high angle, in an inverted base cone with concave interface geometry, i.e., curve

in its central axis direction. The distorted field propagation shape of the Dipole-dipole array is effective in the detection of this kind of structure, at least about its shallowest portion. The tendency to horizontalization of the field vector in short spacing allows for a high incidence angle in the interface in the cone of depression.

This situation enables the field refraction, although resulting in a partial characterization of the structure, as it is expected a conic geometry structure to the detriment of the cylindrical structure of the modeling. The

concavity of the depression cone interface shall enable for low incidence angles in depth, allied to a reduction in resistivity contrast (increase in humidity content in the structure center). The beginning of the cylindrical structure at about 7m is very much far from the 14m depth of the aquifer level, because in this case the cone is started in the non-saturated zone, something far from reality.

The Schlumberger and Wenner arrays are characterized by current electrodes placed at the ends of the device, with potential electrodes fixed in the central position. The Schlumberger array enables for increasing and diverse readings of the current electrodes for the same opening of potential electrodes, whereas for the Wenner array increasing openings are needed in all electrodes at each reading (Mussetti & Khan, 2000). In the work of Furman *et al.* (2003), it is described the higher sensitiveness of these arrays for deep targets in relation to the Dipole-dipole array.

Regarding the Schlumberger array, the propagation of electrical field and potential for short spacing results in geometry of potential field similar to a drop, with main flow vector that has a tendency to verticalization with the increase in depth of investigation and incipient distortion in potential field (Figure 5). This array is very much applied in hydrogeological studies (Salem, H. S., 2001; Sequeira Gómez & Escolero Fuentes, 2010; Urrutia-Fucugauchi, 2014; Dena *et al.*, 2012).

The tendencies of equipotential isosurfaces, parallel and horizontal in relation to the main vector of potential field are coincident with the fronts of liquid percolation originated from the septic tank, condition that shall enable for the field refraction in high angle. The geometries of potential field and contamination plume in the non-saturated zone are also very similar, something that provides a modeling very close to reality. The upper end of the isosurface located at 3m depth coincides with

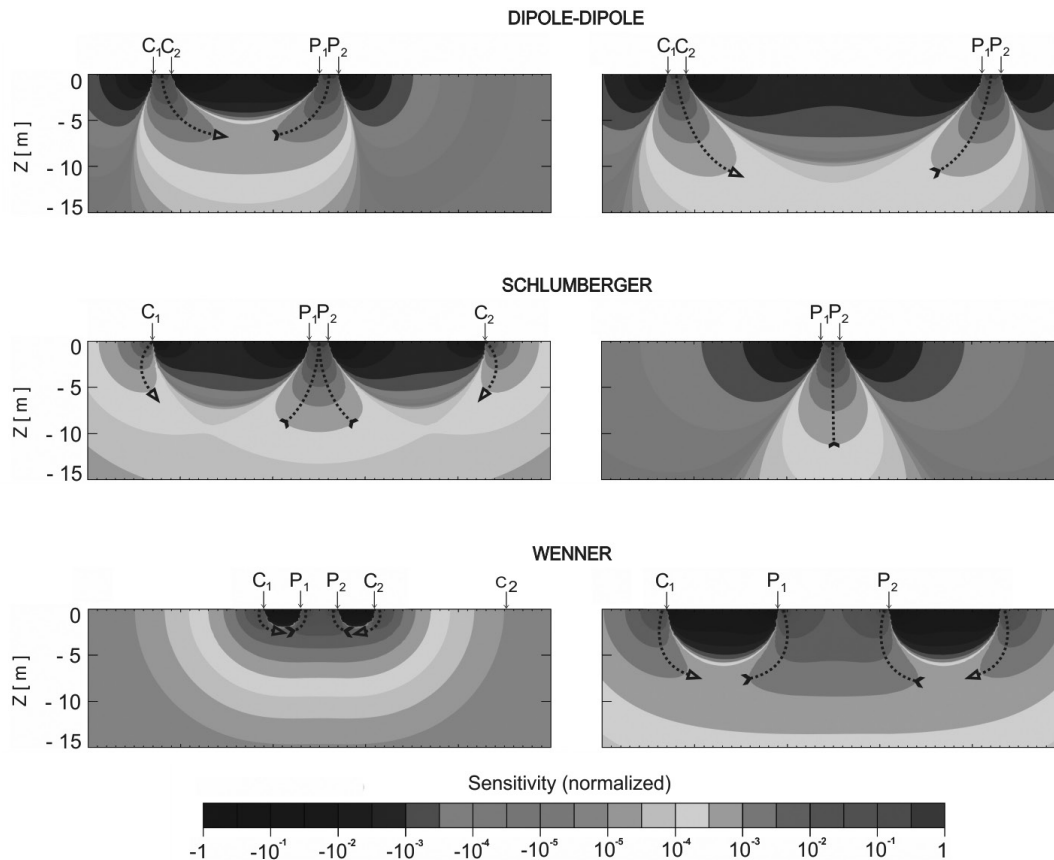


Figure 5. Sections of sensibility normalized for the arrays under study, with main vectors of electrical field propagation (Modified from Knödel *et al.*, 2007).

the base of the septic tank, proved in field, other factor that corroborates the veracity of the model (Figure 4).

However, the complex geometry of the depression cone, hollow and with lateral limit in the slope angle, results in an interface almost parallel to the main vector of field propagation, condition that apparently blocks the detection of this kind of structure by means of the Schlumberger array.

The Wenner array presents a verticalized propagation of the field vectors, i.e., horizontalization of the electrical field and potential isosurfaces, slightly attenuated under high spacing between electrodes (Figure 5). Based in this characteristic and similarly to the Schlumberger array, it is possible to recognize in the isosurface model for the Wenner array the existence of a conic structure below the septic tank. In this case, the accentuated tendency for horizontalization of the field isosurfaces in comparison to the Schlumberger array caused some flattening of the conic structure.

This array presents speed and versatility in tomographic acquisition (ERT) due to the relatively reduced quantity in readings (Dahlin 2000; Zhou *et al.*, 2001; Corwin & Lesch, 2003; Samouëlian *et al.*, 2003). In a comparative study between the Dipole-dipole, Schlumberger and Wenner arrays, Zhou *et al.* (2002) affirm that the Wenner array was the least sensible in the detection of reduction faces in karst terrain (hollow cavity).

The structure placed below the supply well with a keel shape elongated in the central line direction, shall be related to the depression cone. The tendency of horizontalization of the field propagation vectors in higher spacing of electrodes result in high incidence angles with the interface of the depression cone, similar to the Dipole-dipole array, with field refraction and definition of lateral contrast.

However, apparently such conditions do not occur in lateral lines to the supply well, where certainly the resistivity contrast shall be lower, attributed to a peripheral position to the center of the depression cone. The procedure for data acquisition by means of laterally parallel lines, followed by 2D inversion and interpolation in 3D isosurface, generated a processing artifact very distant from the real conic format. Although distorted, this isosurface is initiated in 11m, initial depth of the capillary fringe, horizon able to depression by pumping in the supply well.

Conclusions

A comparison of results among geoelectrical data acquisition revealed the complexity of the study of dynamics targets in the geological environment. The elements analyzed are contained in dry sandy soil (inorganic contamination plume) and saturated (depression cone), both characterized by contrasts of low and high resistivity in relation to the surrounding materials, respectively.

The results demonstrate that in spite of the contrast in electrical properties existent among the studied targets and the surrounding environment, in some cases there simply was no recognizing of the structure by means of any set array, while some geophysical models were simply unreal. Besides all the care required for planning, acquisition and treatment of data, the choice for the array is notoriously relevant to the recognizing and modeling of structures bound to coherent analysis and interpretations.

The versatility of the Dipole-dipole array in terms of data acquisition logistics makes its use attractive to field acquisitions. Under conditions of non-saturated zone, however, the results acquired in this work demonstrate that although possible the definition of contrasts by the presence of contamination plume in this environment, the modeling of isosurface resulted in a product totally disconnected to the structure generated by the propagation of liquids in this environment. The data acquired by means of this array yet enabled for the modeling of the depression cone in very reasonable terms.

The data acquired by means of the Schlumberger and Wenner arrays resulted in a structure with the shape of a drop, below the septic tank, very close to the shape of a contamination plume in vertical flow. The modeling in Schlumberger array enabled for positioning the upper end of the structure right below the septic tank, at 3m depth. However, this same array showed to be ineffective in the detection and consequent modeling of the depression cone, possibly due to issues of propagation of electrical field and potential.

Results referring to the Wenner array enabled for the recognition of a structure in the shape of a keel, elongated along the central line, associated to the depression cone. This shape is attributed to issues of lateral sensibility and procedure of acquisition/interpolation of data, quite far from the inverted cone shape.

In face of the results of this research, the Dipole-dipole array is recommended in works of modeling of verticalized three-dimensional structures of high resistivity. The Wenner and Schlumberger arrays are recommended to modeling of low resistivity verticalized three-dimensional structures, with emphasis to the Schlumberger array.

References

- Aizebeokhai A.P., Olayinka A.I., Singh V.S., Uhuegbu C.C. 2011. Effectiveness of 3D geoelectrical resistivity imaging using parallel 2D profiles. *International Journal of the Physical Sciences*, 6, 5623-5647.
- Arango-Galván C., Torre-González B., Chávez-Segura R.E., Tejero-Andrade A., Cifuentes-Nava G. Hernández-Quintero E. 2011. Structural pattern of subsidence in an urban area of the southeastern Mexico Basin inferred from electrical resistivity tomography. *Geofísica Internacional*, 50, 401-409.
- Balek J., 1989, Groundwater resources assessment – Developments in water, *Science*, 38. Elsevier, Praga, 251p.
- Belmonte-Jiménez S., Jimenez-Castañeda M.E., Pérez-Flores M.A., Campos-Enríquez J., Reyes-López J.A., Salazar-Peña L., 2012, Characterization of a leachate contaminated site integrating geophysical and hydrogeological information. *Geofísica Internacional*, 51, 4, 309-321.
- Chambers J.E., Kuras O., Meldrum P.I., Ogilvy R.D., Hollands J. 2006. Electrical resistivity tomography applied to geologic, hydrogeologic, and engineering investigations at a former waste-disposal site. *Geophysics*, 71:231-239.
- Corwin D.L., Lesch S.M., 2003, Application of soil electrical conductivity to precision agriculture: theory, principles, and guidelines. *Agronomy Journal*, 95: 455-471.
- Dahlin T., 2000, Short note on electrode charge-up effects in DC resistivity data acquisition using multi-electrode arrays. *Geophysical Prospecting*, 48, 181-187.
- Delgado-Rodríguez O, Flores-Hernández D., Amezcuca-Allieri M.A., Shevnev V., Rosas-Molina A., Marín-Córdova S., 2014, Joint interpretation of geoelectrical and volatile organic compounds data: a case study in a hydrocarbons contaminated urban site. *Geofísica Internacional*, 53,183-198
- Dena O.S., Griselda Obeso C., Doser D., Leyva J.E., Rascon E., Gómez, F., Domínguez M.A., 2012, Using subsurface geophysical methods in flood control: A resistivity survey to define underground storage capacity of a sand body in Ciudad Juárez, Mexico. *Geofísica Internacional*, 51, 225-249.
- Departamento de Águas e Energia Elétrica do Estado de São Paulo - DAEE. 1981. Estudos de águas subterrâneas, Região Administrativa 5 - Campinas. São Paulo, 607 p.
- Elgzeli Y.M., Ondovčín T., Zbyněk H., Jiří K., Jiří M., 2013, Impact of heavy groundwater pumping on hydrogeological conditions in Lybia: Past and present development and future prognosis on a regional scale. *Acta Geologica Polonica*, 63, 283-296.
- Fitts C.R., 2002, Groundwater Science. Academic Press, London, 450p.
- Furman A., Ferre T.P.A., Warrick A.W., 2003, A sensitivity analysis of electrical resistivity tomography array types using analytical element modeling. *Vadose Zone Journal*, 2, 416-423.
- Griffiths D.H., Baker R.D., 1993, Two-dimensional resistivity imaging and modeling in areas of complex geology. *Journal of Applied Geophysics*, 29, 211-226.
- Hernández-Soriano M.C., 2014, Environmental risk assessment of soil contamination. InTech, New York, 905p.
- Hiscock K.M., 2005, Hydrogeology: principles and practice. Blackwell Publishing, Oxford, 405 pp.
- König L., Weiss J.L., 2009, Groundwater: modelling, management, and contamination. Nova Science Publishers Inc., New York, 422 pp.
- Knödel K., Lange G., Voigt H., 2007, Environmental geology: handbook of field's methods and case studies. Springer, Hannover, 1374 pp.
- Lehr J., Hyman M., Gass T.S., Servers W.J., 2001, Handbook of complex environmental remediation problems. McGraw-Hill Handbooks, 606 pp.

- Loke M.H., Baker R.D. 1996. Rapid least-squares inversion of apparent resistivity pseudosections by quasi-Newton method. *Geophysical Prospecting*, 44, 131-152.
- Lowrie W., 2007, *Fundamentals of Geophysics*. Cambridge University Press, New York, 393 pp.
- Melo S.M., Coimbra M.A., Cuchierato G., 1997, Fácies Sedimentares da Formação Rio Claro, Neocenoico da Depressão Periférica Paulista. *Revista IG. São Paulo (SP)*, 18, 49-63.
- Ministry of Mines and Energy – MME. 2013. *Brazilian Energy Balance – final report*. Empresa de Pesquisas Energéticas, Brasília, 284 pp.
- Moreira C.A., Dourado J.C., Braga A.C.O., 2006, Aplicação da técnica de caminhamento elétrico em área contaminada por derivados de petróleo. *Brazilian Journal of Geophysics*, 24, 383-392.
- Moreira C.A., Lopes S.M., Schweig C., Seixas A.R., 2012, Geoelectrical prospection of disseminated sulfide mineral occurrences in Camaquã sedimentary basin, Rio Grande do Sul state, Brazil. *Brazilian Journal of Geophysics*, 30, 169-179.
- Moon C.J., Whateley M.K.G., Evans A.M., 2006, *Introduction of mineral exploration*. 2^oed., Blackwell Publishing, Malden, 499 pp.
- Mussett A.E., Khan M.A., 2000, *Looking into the Earth: an introduction to geological geophysics*. Cambridge University Press, New York, 493 pp.
- Nemerow N.L., Agardy F.J., Sullivan P., Salvato J.A., 2009, *Environmental Engineering: prevention and response to water, food, and air-borne disease and illness*. 6^oed., John Wiley & Sons, New Jersey, 394 pp.
- Nyquist J.E., Peake J.S., Roth M.J.S., 2007, Comparison of an optimized resistivity array with dipole-dipole soundings in karst terrain. *Geophysics*, 72, 139-144.
- Okpoli C.C., 2013, Sensitivity and resolution capacity of Electrode configurations. *International Journal of Geophysics*, 2013, 12p.
- Oliva A., Chang H.K., Caetano-Chang M.R., 2005, Determinação da condutividade hidráulica da Formação Rio Claro: análise comparativa através de análise granulométrica e ensaios com permeâmetro guelph e testes de slug. *Agua Subterrâneas*, 19, 1-17.
- Oliva A., Chang H.K., 2007, Mapeamento do Lençol Freático no Município de Rio Claro (SP) Empregando a Técnica de Sondagem Elétrica Vertical. *Revista Brasileira de Geociências*, 26, 27-34.
- Peirce J.J., Weiner R.F., Vesilind P.A., 1998, *Environmental pollution and control*. 4^oed., Butterworth-Heinemann, Woburn, 409 pp.
- Sara M., 2003, *Site assessment and remediation handbook*. 2^oed., Lewis Publishers, Florida, 1161 pp.
- Salem H.S., 2001, Modelling of lithology and hydraulic conductivity of shallow sediments from resistivity measurements using Schlumberger vertical electrical soundings. *Energy Sources*, 23, 599-618.
- Samouëlian A., Cousin I., Richard G., Tabbagh A., Bruand A., 2003, Electrical Resistivity Imaging for Detecting Soil Cracking at the Centimetric Scale. *Soil Science Society of America Journal*, 67, 1319-1326.
- Sequeira Gómez L., Escolero Fuentes O., 2010, The application of electrical methods in exploration for ground water resources in the River Malacatoya sub-basin, Nicaragua. *Geofísica Internacional*, 49, 27-41.
- Twardowska I., Allen H.E., Häggblom M.H., 2006, *Soil and water pollution: monitoring, protection and remediation*. Nato Science Series, Springer, Krakom, 662 pp.
- Urrutia-Fucugauchi J., Trigo-Huesca A., Téllez-García E., Pérez-Cruz L., Méndez-Rivero F. 2014. Volcano-sedimentary stratigraphy in the Valsequillo Basin, Central Mexico inferred from electrical resistivity soundings. *Geofísica Internacional*, 53, 87-94.
- Zhou Q.Y., Shimada J., Sato A., 2001, Three-dimensional spatial and temporal monitoring of soil water content using electrical resistivity tomography. *Water Resources Research*, 37:273-285.

Site Response of the NARS-Baja and RESBAN Broadband Networks of the Gulf of California, México

Lenin Ávila-Barrientos* and Raúl R. Castro

Received: May 21, 2015; accepted: January 13, 2016; published on line: April 01, 2016

Resumen

Estudiamos la respuesta sísmica de las estaciones de banda ancha localizadas en el Golfo de California, México, usando el método de cocientes espectrales entre las componentes horizontales y verticales (HVSR). Analizamos 92 sismos registrados por las redes NARS-Baja y RESBAN, operadas por el CICESE. La base de datos consiste de eventos registrados entre 2002 y 2006, con magnitudes que varían de 3.2 a 6.6. Los registros fueron rotados para encontrar las componentes radial y transversal del movimiento del terreno y calculamos los espectros de Fourier de las ventanas de la onda S para las tres componentes. Calculamos los cocientes espectrales HVSR para cada componente horizontal y el promedio de las dos componentes para cada evento. Analizamos los registros de 20 estaciones localizadas en sitios con diferentes características geológicas y encontramos que existe dependencia azimutal en seis de ellas, teniendo factores de amplificación que varían de 1.5 hasta 13 veces en los rangos estrechos de azimut. También encontramos que los sitios con factores de amplificación significantivos (arriba de tres) muestran un incremento con respecto al incremento de la magnitud.

Palabras clave: Efectos de sitio, dependencia azimutal, Golfo de California, método H/V, RESBAN, NARS-Baja.

Abstract

We studied the seismic response of broadband stations located around the Gulf of California, Mexico, using the horizontal to vertical component spectral ratio method (HVSR). We analyzed 92 earthquakes recorded by the NARS-Baja and RESBAN networks, operated by CICESE. The database consists of events recorded between 2002 and 2006, with magnitudes ranging from 3.2 to 6.6. We rotated the records to find radial and transversal ground-motion components and we calculated Fourier spectra of S-wave windows recorded for the three ground-motion components. Then, we calculated HVSR for the individual components and the average of both horizontal components for every event. We analyze records from 20 stations located on sites with different geologic characteristics and we find azimuthal dependence on six of them that have amplification factors varying from 1.5 to up to 13 times at narrow back-azimuth ranges. We also find that sites with significant amplification factors (above three) show increasing amplification with increasing source magnitude.

Key words: Site effects, azimuthal dependence, Gulf of California, H/V method, RESBAN, NARS-Baja.

L. Ávila-Barrientos*
CONACYT Research Fellow-CICESE
Centro de Investigación Científica
y de Educación Superior de Ensenada
División Ciencias de la Tierra
Departamento de Sismología
Carretera Ensenada-Tijuana 3918
C.P. 22860, Ensenada
Baja California, México
*Corresponding autor: lenavila@cicese.mx

R. R. Castro
Centro de Investigación Científica
y de Educación Superior de Ensenada
(CICESE)
División Ciencias de la Tierra
Departamento de Sismología
Carretera Ensenada-Tijuana 3918
C.P. 22860, Ensenada
Baja California, México

Introduction

The evaluation of amplification of seismic energy is very important because it is directly related to the damage that the structures can undergo. For this reason the analysis of the site response is an important goal in seismic hazard analysis. Site response functions are also useful to correct spectral records of ground motion generated by earthquakes, particularly for calculating accurate source parameters. The main aim of this study is to determine the site effects of the permanent stations located around the Gulf of California, Mexico and to analyze the effect of the azimuth and source magnitude of the incoming seismic energy on the site amplification. For this purpose we calculated spectral ratios between the horizontal to vertical ground-motion components (HVSr) using seismograms recorded in a wide range of azimuths. The HVSr technique was originally introduced by Nogoshi and Igarashi (1970) and was used

by Nakamura (1989) to evaluate sediment-induced amplifications from recordings of micro-tremors. Lermo and Chávez-García (1993) extended this method for *S* waves from earthquake records and since then the HVSr method has been used extensively to estimate site effects. More recently, Cultrera *et al.*, (2003) observed a strong dependence of amplification with the source azimuth; they studied earthquakes within a fault zone in the Nocera, Umbra region (Central Italy) and found that in three of the stations analyzed the amplification was bigger for events with an azimuth range between 150 and 180 degrees, suggesting that the geometry and orientation of the fault zone played an important role in the site response. Another similar study was carried on by Pedersen *et al.* (1995) to estimate site effects in alluvial valleys of the French Alps, finding a dependence of site amplifications with azimuth and with incidence of incoming waves.

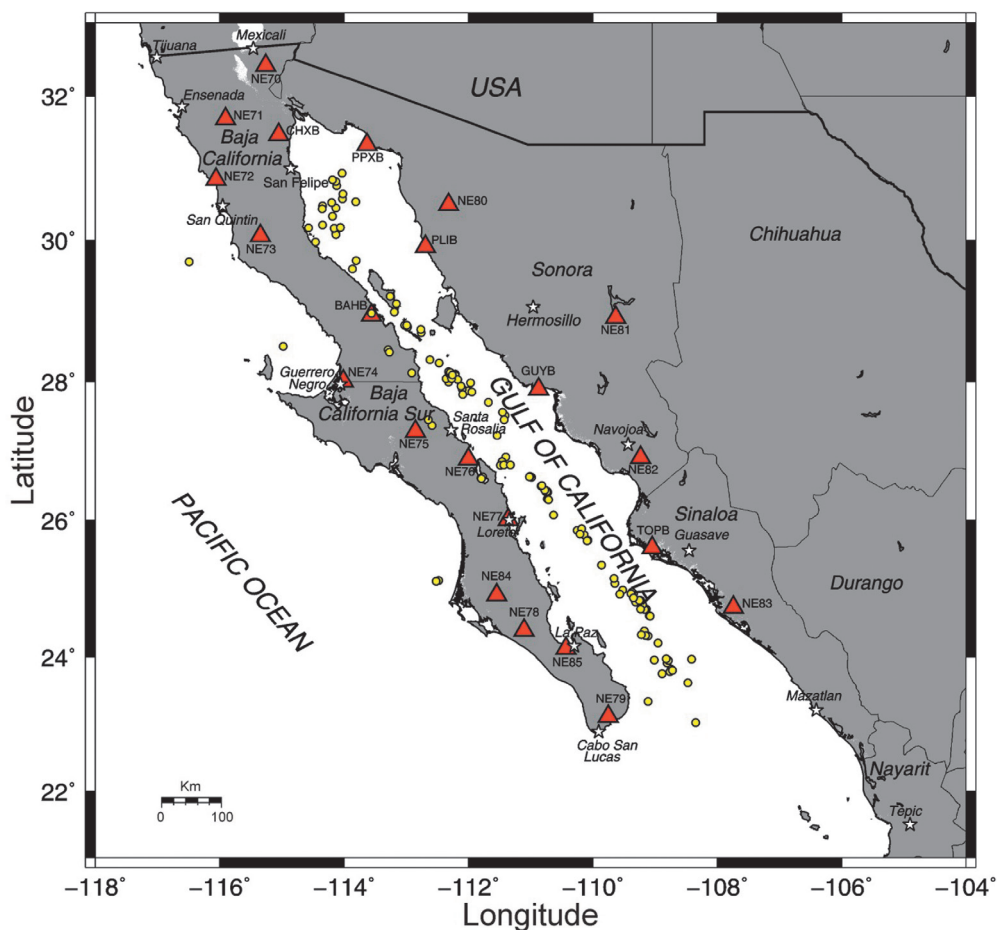


Figure 1. Stations used in this study. The triangles represent the NARS-Baja and RESBAN stations, and filled yellow circles, earthquakes used in this analysis for the period of 2002 to 2006.

We use seismograms recorded by broadband stations located in the Gulf of California, Mexico, region from the NARS-Baja (Network of Autonomously Recording Seismographs) and the RESBAN (*Red Sismológica de Banda Ancha del Golfo de California*) networks, both operated by the CICESE (*Centro de Investigación Científica y de Educación Superior de Ensenada, Baja California*) to determine site effects and analyze the azimuth and the magnitude dependence. Figure 1 shows the region of the study, the epicenters of the earthquakes selected and the distribution of the seismic stations used.

Data

We selected 92 earthquakes recorded by the seismic stations of NARS-Baja and RESBAN networks. Most of these events are located within the Gulf of California (Figure 1) and a few of them to the west and inside the Peninsula. We analyzed records from a total of 20 stations, 15 from the NARS-Baja and five from the RESBAN networks. The NARS-Baja network operated from 2002 to 2008 and consisted of broadband stations, owned by the Utrecht University, with STS2 sensors, a global positioning system (GPS) and a 24-bit data logger (Trampert *et al.*, 2003; Clayton *et al.*, 2004). The RESBAN network has been in operation since 1995 and consists of 24-bit Guralp digitizers with a CMG-SAM2 acquisition module, GPS for time control and CMG-40T or CMG-3ESP sensors (Castro *et al.*, 2011). Table 1 lists the coordinates of the

stations used and the geology characteristics of the sites where the stations were installed. We classified the stations in three groups according with the geological characterization of the sites. Group I corresponds to stations located on intrusive volcanic rocks with a low degree of weathering; Group II are stations located on extrusive igneous rocks with moderate weathering; Group III are stations located on poorly consolidated conglomerates or on soil.

The database used consists of 92 earthquakes with magnitudes ranging between 3.2 and 6.6 and recorded between 2002 and 2006. Figure 2 shows the magnitude distribution of the events analyzed; there are a larger number of low magnitude (3.3 to 4.4) events than those with larger magnitude ($M > 5.0$). The RESBAN network has good detection capability and because of the wide azimuthal distribution of the stations (Figure 1), it allows the location of relatively small events. The hypocenters were relocated by Castro *et al.* (2011) using regional data from the networks above mentioned. They found that the epicenters have a location difference of about 43 km, for m_b 3.2 to 5.0 events, respect to those reported by the Preliminary Determinations of Epicenters (PDE-National Earthquake Information Center). Events with M_w 5.0 to 6.7 show a difference of 25 km on average. We use in this paper the coordinates of the events relocated by Castro *et al.* (2011) and listed in Table 2.

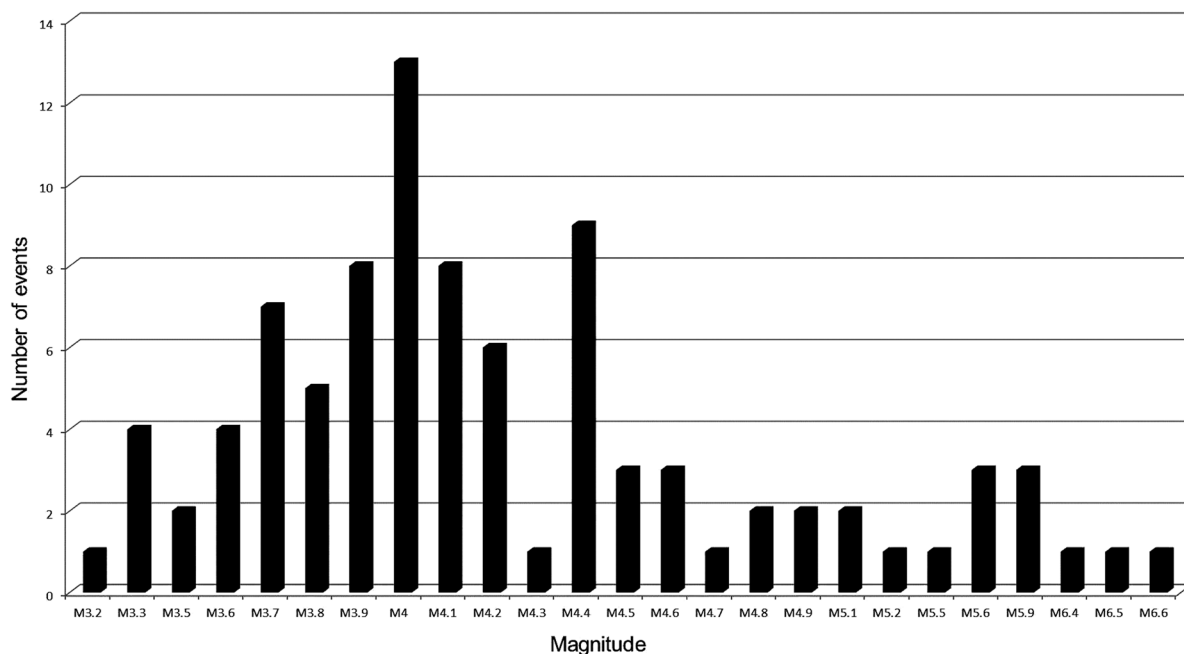


Figure 2. Histogram of magnitudes *versus* number of records.

Table 1. List of stations of NARS-Baja and RESBAN networks. Group I corresponds to stations located on intrusive volcanic rocks with a low degree of weathering; Group II are stations located on extrusive igneous rocks with moderate weathering; Group III are stations located on poorly consolidated conglomerates or soil.

Network	Location of station	Code	Latitude, °	Longitude, °	Elevation, m	Group Class	Site Geology
RESBAN	Bahía de los Ángeles, B. C.	BAHB	28.943	-113.561	-	I	Igneous intrusive: granodiorite-tonalite
RESBAN	El Chinero, B.C.	CHXB	31.472	-115.0513	-	II	Igneous extrusive: basalt
RESBAN	Puerto Peñasco, Sonora	PPXB	31.335	-113.632	-	I	Igneous intrusive: granite-granodiorite
RESBAN	Puerto Libertad, Sonora	PLIB	29.915	-112.694	-	I	Igneous intrusive: granodiorite
RESBAN	Guaymas, Sonora	GUYB	27.899	-110.871	-	II	Igneous breach with fractures filled with calcium carbonate
RESBAN	Topolobampo, Sinaloa	TOPB	25.605	-109.047	-	II	Igneous extrusive: basalt
NARS-Baja	Mexicali	NE70	32.421	-115.261	-23	III	Soil: sedimentary deposits of fine sand and alluvium
NARS-Baja	Agua Blanca	NE71	31.690	-115.905	1155	I	Igneous intrusive: granodiorite-tonalite
NARS-Baja	Camalu	NE72	30.848	-116.059	17	III	Soil: sedimentary deposits of fine sand and alluvium
NARS-Baja	Rosario	NE73	30.065	-115.348	489	I	Igneous intrusive: granodiorite-tonalite
NARS-Baja	Gro. Negro	NE74	28.008	-114.014	21	III	Eolian deposits unconsolidated composed of fine sands
NARS-Baja	San Ignacio	NE75	27.293	-112.856	137	II	Volcanic sandstone: conglomerates mixed with sand
NARS-Baja	Mulege	NE76	26.889	-111.999	35	II	Volcanic breach: dacite-andesite
NARS-Baja	Loreto	NE77	26.016	-111.361	40	II	Sedimentary deposits and conglomerates
NARS-Baja	Las Pocitas	NE78	24.398	-111.106	82	III	Sedimentary deposits unconsolidated
NARS-Baja	San José Del Viejo	NE79	23.119	-109.756	225	I	Igneous intrusive: granite-granodiorite
NARS-Baja	Caborca	NE80	30.500	-112.320	225	III	Unconsolidated sandstone
NARS-Baja	Novillo (Hermosillo)	NE81	28.918	-109.636	295	III	Unconsolidated conglomerate
NARS-Baja	Navojoa	NE82	26.916	-109.231	183	II	Consolidated conglomerate
NARS-Baja	Navolato (Culiacán)	NE83	24.731	-107.739	28	III	Sedimentary deposits of alluvium unconsolidated
NARS-Baja	El Toro	NE84	24.913	-111.545	21	III	Sedimentary deposits unconsolidated sand, clays and alluvium

For each station we selected well recorded events having a hypocentral distance of less than 500 km. For this reason, the number of events analyzed per station is not uniform. Figure 3 shows the distribution of earthquakes per station and Figure 4, the range of epicentral distance and magnitudes of the events used in this study. The stations CHBX and NE85 were excluded from the analysis because CHBX had records only for the north and vertical components and NE85 did not have any records available for the analyzed period.

Two examples of the distribution of events per azimuth range are shown on Figure 5, for stations NE74 (upper frame) and NE76 (lower frame). We can observe that for station NE74 most events are located on the azimuth range of 91° - 135° while for station NE76 most events are between 91° - 135° and 316° - 360° .

Method

The events selected were corrected for base line and instrument response. Then, we chose time windows containing the S wave, where most of the energy in the records is concentrated. Figure 6 shows an example of a seismogram recorded by station BAHB of event 084 (Table 2) with a magnitude of 5.9. The length of the windows selected for different stations tends to

increase with epicentral distance, varying from about 2 s for local events to 85 s for regional earthquakes (Table 3). The seismograms were rotated into radial and transversal components and the Fourier amplitudes computed for the three ground-motion components. The first and last 5% of the time window were cosine tapered and the spectra smoothed using a variable frequency band, selected to preserve the energy, of $\pm 25\%$ of 19 predefined central frequencies between 0.16 and 10.0 Hz. The spectral amplitudes at the selected central frequency are the average amplitude within the corresponding frequency band. For instance, the amplitude at 5 Hz corresponds to the average in the 3.75-6.25 Hz band. We did not use higher frequencies because the Nyquist frequency of the records is at 10 Hz. Figure 7 shows the Fourier acceleration spectral amplitudes calculated for event 084 recorded at BAHB.

We calculated spectral ratios between horizontal and vertical components of motion (radial/vertical and transversal/vertical) to obtain the site response, following the HVSR method proposed by Nakamura (1989) and extended by Lermo and Chávez-García (1993) to estimate the site amplification of the horizontal component of ground motion under the assumption that the vertical component is insensitive to site amplification. To corroborate

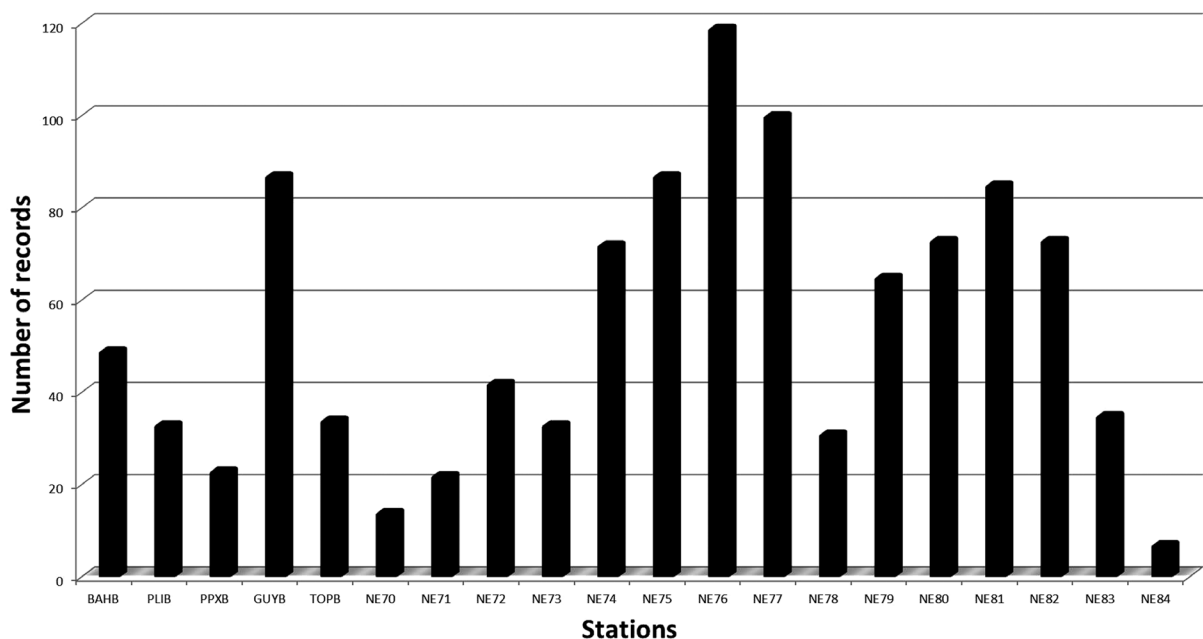


Figure 3. Histogram of stations versus number of records.

Table 2. List of events used for this analysis. The hypocentral coordinates were taken from Castro *et al.* (2011).

Number	Date	Origin time	Latitude, °	Longitude, °	Depth, km	Magnitude
2	2002-07-03	06:37:33.390	23.8202	-108.7391	19.82	3.8
4	2002-10-03	16:08:32.400	23.3420	-109.1160	10.00	6.5
5	2002-10-29	06:16:13.735	25.8584	-110.2509	----	4.2
6	2002-11-05	04:58:20.616	28.7788	-112.9769	4.01	4.4
7	2002-11-05	05:15:03.258	28.8039	-113.0273	0.00	4.4
8	2002-12-06	06:24:12.256	26.3152	-110.7364	8.61	4.0
9	2002-12-07	01:33:45.285	26.0794	-110.6330	9.77	4.1
10	2002-12-08	17:45:17.255	26.3010	-110.7148	13.58	3.6
12	2003-01-17	21:10:11.585	24.2047	-108.9501	----	4.0
13	2003-01-19	16:46:30.147	26.9204	-111.3973	1.97	4.2
16	2003-01-24	15:11:09.615	29.7168	-113.8043	5.98	4.0
18	2003-03-12	23:41:30.561	26.4994	-110.8355	2.02	6.4
19	2003-03-12	23:46:33.872	26.4254	-110.7600	9.02	4.8
20	2003-03-13	00:23:54.173	26.4218	-110.7322	6.94	3.3
21	2003-03-13	01:30:47.845	26.4252	-110.7495	4.51	3.6
22	2003-03-13	01:48:55.456	26.4171	-110.7549	5.02	4.1
23	2003-03-13	02:25:38.965	26.4135	-110.7284	4.69	3.8
24	2003-03-13	04:23:06.995	26.4206	-110.7417	5.01	4.0
25	2003-03-13	08:12:50.409	26.6255	-110.9865	6.07	3.7
26	2003-03-13	14:38:20.278	26.6414	-111.0135	12.99	4.1
27	2003-03-13	20:28:27.681	26.4492	-110.7764	9.53	3.6
28	2003-03-13	20:48:54.034	26.4402	-110.7719	9.86	3.5
29	2003-03-22	17:55:41.519	26.5048	-110.8193	5.27	4.8
30	2003-04-05	20:50:06.892	24.9304	-109.3442	6.45	3.5
31	2003-04-15	08:21:16.799	25.0809	-109.6490	1.33	5.5
32	2003-04-28	16:02:30.395	23.7497	-108.8893	----	3.7
34	2003-07-05	02:17:53.184	28.1282	-112.9112	20.02	3.7
35	2003-08-15	09:44:41.388	28.4596	-113.2922	5.66	4.9
36	2003-09-06	09:14:39.270	25.1547	-109.6612	----	3.7
39	2003-09-10	11:26:41.923	30.6502	-114.0170	8.30	3.7
40	2003-11-12	04:54:56.384	29.1098	-113.1616	----	5.6
43	2003-12-05	22:54:00.165	29.2136	-113.2594	3.97	4.7
46	2004-01-13	11:40:57.973	24.6070	-109.0929	3.43	4.2
47	2004-01-13	14:00:06.661	24.6044	-109.0794	2.87	4.0
48	2004-01-13	20:54:42.962	24.3837	-109.1738	1.89	4.4
49	2004-01-14	10:13:12.057	24.3183	-109.1394	1.84	3.9
50	2004-01-14	10:21:33.061	24.7042	-109.1408	----	4.0
51	2004-01-14	10:46:54.029	24.3079	-109.1101	23.39	3.8
52	2004-01-14	10:55:47.204	24.3161	-109.1561	----	4.4
53	2004-01-14	22:46:32.053	24.7750	-109.1999	2.49	4.4
54	2004-01-14	22:48:42.843	24.7006	-109.1669	5.87	4.5
55	2004-01-14	23:50:22.024	24.7757	-109.1996	9.29	4.0
56	2004-02-09	00:01:45.200	23.9112	-108.8061	8.56	5.1
59	2004-02-11	04:55:36.850	23.9681	-108.8121	0.41	4.5
60	2004-02-11	12:28:07.975	23.9501	-108.7839	1.21	4.4
61	2004-02-15	01:46:09.825	23.9532	-109.0141	----	3.8
62	2004-02-15	01:57:32.310	23.9712	-108.8167	23.62	3.9
63	2004-02-18	10:59:17.664	23.7845	-108.7600	1.33	5.9
64	2004-02-18	11:07:08.506	23.8015	-108.7167	9.88	4.1
65	2004-02-18	19:30:39.033	26.6345	-111.0169	7.23	3.9
67	2004-03-06	09:49:22.113	24.8109	-109.3111	0.26	4.2
68	2004-03-22	08:57:09.860	25.7894	-110.1400	16.36	4.0
70	2004-06-22	06:10:39.352	24.9881	-109.5224	19.60	4.6
71	2004-06-27	18:04:48.198	24.9551	-109.3730	6.26	4.0
72	2004-07-08	21:21:42.320	24.9242	-109.5665	19.27	4.4
73	2004-07-08	21:31:37.599	24.9329	-109.3874	3.76	4.1
74	2004-08-07	10:41:24.442	26.6103	-111.7947	6.21	3.2
75	2004-08-13	10:41:26.405	27.8557	-111.9452	----	3.9
77	2004-08-20	06:36:37.252	30.2132	-114.3451	13.17	4.1
78	2004-08-20	08:06:14.457	28.4243	-113.2712	3.00	4.6

Number	Date	Origin time	Latitude, °	Longitude, °	Depth, km	Magnitude
83	2004-09-15	10:18:33.836	30.1810	-114.0606	21.96	4.0
84	2004-09-24	14:43:08.689	28.7011	-112.7587	----	5.9
85	2004-09-24	15:27:13.862	28.7472	-112.7686	6.29	3.9
87	2004-10-24	23:26:11.240	30.5384	-113.8123	----	3.6
88	2004-12-01	18:51:06.048	24.7048	-109.2338	21.25	4.1
90	2005-02-22	19:15:47.975	25.8845	-110.1809	0.83	5.6
92	2005-04-19	15:37:43.471	30.4821	-114.3439	----	3.3
96	2005-06-05	08:28:46.353	23.6170	-108.4726	2.32	5.6
97	2005-07-04	02:24:41.159	29.5973	-113.8642	5.60	3.3
98	2005-07-09	08:55:10.780	24.8336	-109.2318	9.48	4.2
99	2005-07-10	17:56:46.314	24.8329	-109.2511	15.11	4.2
100	2005-07-18	17:26:24.392	24.3295	-109.2214	22.52	3.9
102	2005-10-31	13:41:22.454	30.9385	-114.0359	----	3.9
103	2005-11-27	18:56:00.163	25.7119	-110.0829	----	4.0
104	2005-11-27	23:58:11.825	25.7069	-110.0950	2.86	4.4
107	2005-12-24	05:38:24.541	25.8019	-110.2082	0.36	3.3
108	2005-12-26	19:26:18.195	24.8680	-109.3442	22.37	3.9
109	2006-01-03	08:21:17.646	28.0462	-112.3573	----	3.7
110	2006-01-03	21:58:19.455	28.1111	-112.2111	----	4.3
114	2006-01-04	08:30:39.713	28.1403	-112.3048	13.23	4.5
115	2006-01-04	08:32:30.394	28.0433	-112.2746	7.34	6.6
116	2006-01-04	09:05:51.803	28.3152	-112.6198	----	4.1
117	2006-01-04	09:17:55.235	28.2713	-112.4735	----	4.9
118	2006-01-04	10:27:23.004	28.1446	-112.3208	3.95	4.4
119	2006-01-05	03:55:53.306	28.1307	-112.2938	10.03	3.8
120	2006-01-07	07:55:16.754	28.1001	-112.2589	5.60	4.0
121	2006-01-15	21:32:24.412	28.8070	-112.9921	12.97	3.7
123	2006-04-23	07:51:28.994	28.9721	-113.5631	16.63	4.0
127	2006-05-28	14:00:56.368	26.8537	-111.4574	1.26	4.6
128	2006-05-28	14:02:52.685	26.8018	-111.4856	----	5.2
129	2006-05-28	14:18:01.386	26.8046	-111.4336	----	5.1
131	2006-07-30	01:20:56.966	26.8096	-111.3266	19.39	5.9

Table 3. Time windows containing S waves selected from earthquakes recorded on stations analyzed.

Station	Minimum window length (seconds)	Maximum window length (seconds)
BAHB	1.74	43.55
PPXB	3.53	44.14
PLIB	4.08	74.64
GUYB	2.91	63.05
TOPB	3.08	69.80
NE70	5.69	84.77
NE71	8.28	45.15
NE72	5.53	33.92
NE73	3.83	28.55
NE74	4.84	62.96
NE75	2.97	41.87
NE76	2.22	41.95
NE77	3.16	63.55
NE78	6.51	58.65
NE79	5.23	24.46
NE80	7.91	52.64
NE81	5.96	39.60
NE82	2.77	37.96
NE83	2.12	39.34
NE84	8.95	21.21

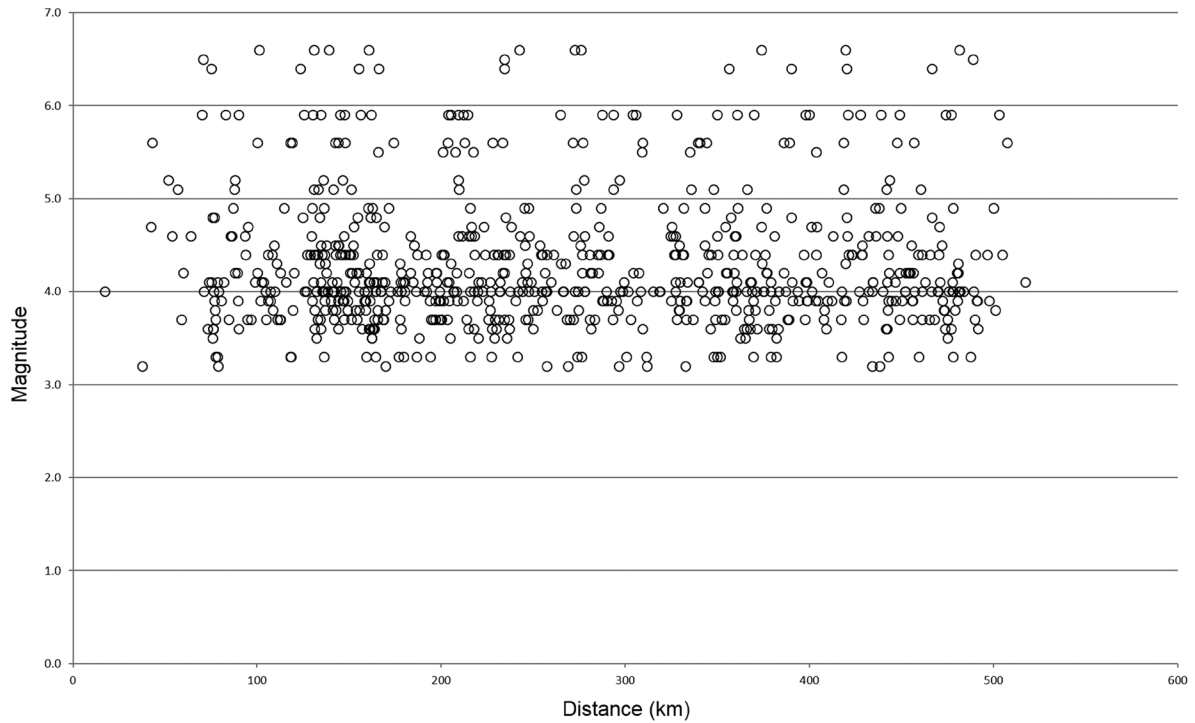


Figure 4. Spatial distribution of the events used.

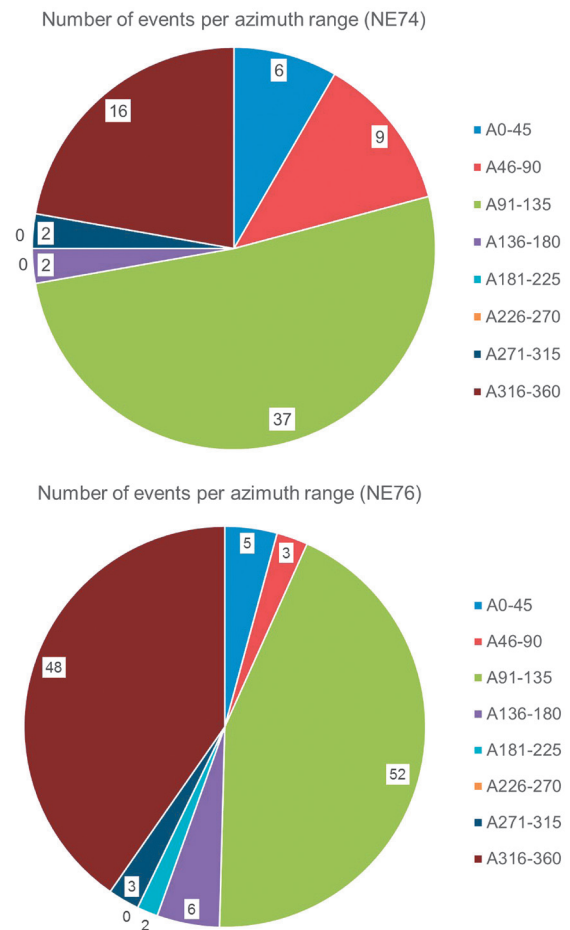


Figure 5. Number of events recorded per azimuth range for station NE74 (top) and station NE76 (bottom).

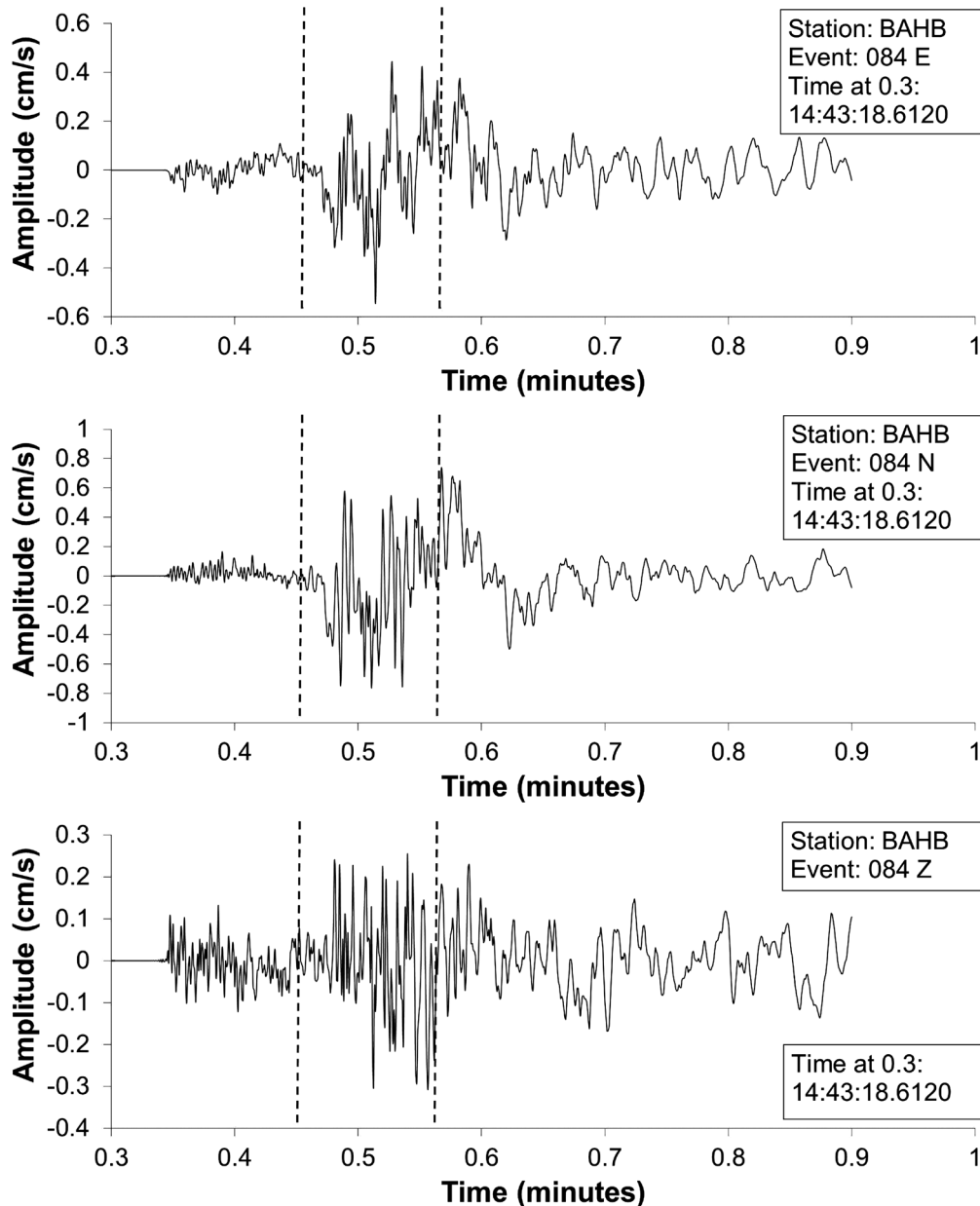


Figure 6- Seismogram for event 084, recorded at station BAHB, showing the S-wave window used to calculate the Fourier transform.

this assumption we calculate spectral ratios between vertical components from events recorded simultaneously on a reference site and a target site. We choose station NE79 (Figure 8) as the reference site because it is localized on a solid igneous outcrop (granite). To minimize source-station path effects we selected events recorded at both stations with similar epicentral distances (with a difference of less than 52 km). Figure 9 shows the vertical component spectral ratios, using station NE79

as the reference site, obtained for stations having records with similar hypocentral distances at both target and reference sites. We observe that events with large (> 52 km) differences between source-to-target and source-to-reference distances tend to have large spectral ratios. For those stations the large target/reference ratio must be due to different attenuation effects, since the paths are not the same. Nevertheless, there are few stations (NE81, NE82 and NE83) that show site

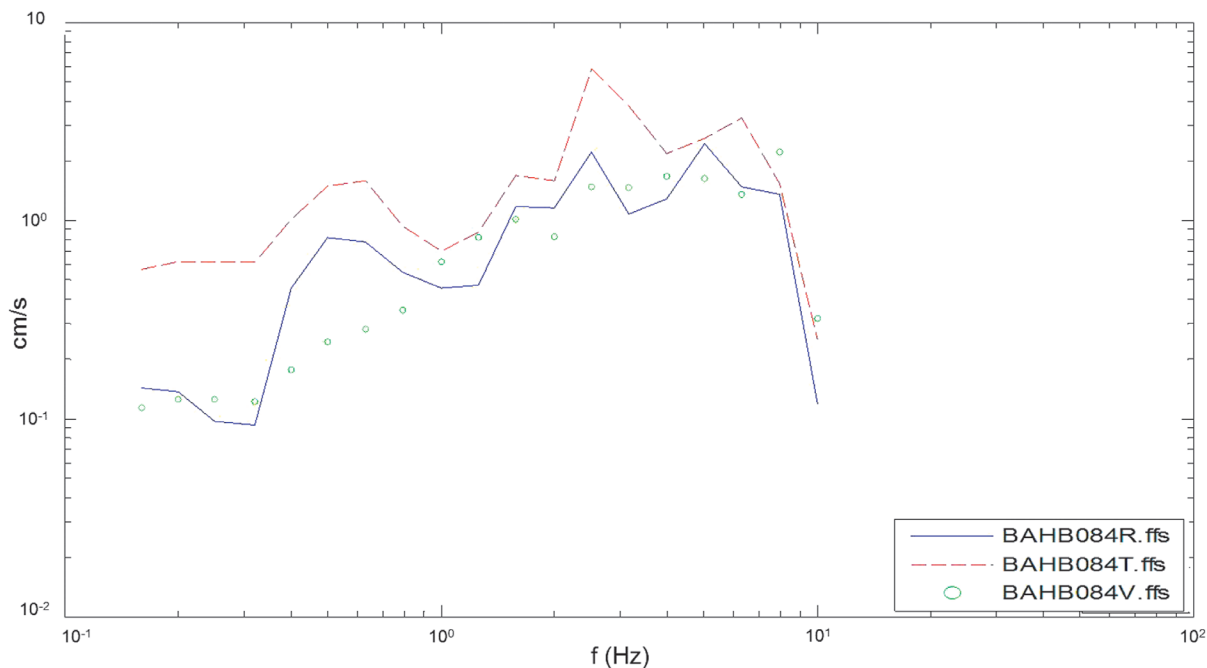


Figure 7. Sample of spectra calculated for station BAHB showing the three components for event 084. Solid line represents the radial component, dashed line, the transversal and circles, the vertical component.

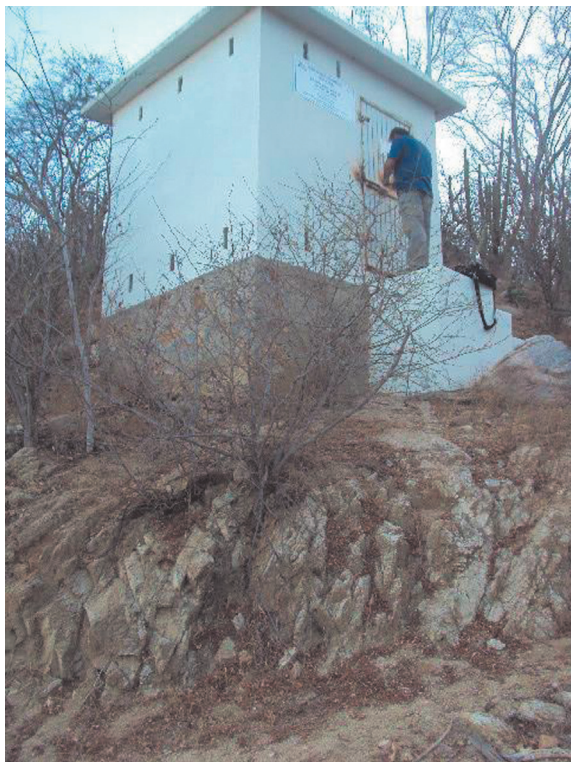


Figure 8. The picture shows the outcrop of granite where station NE79 is localized.

amplification on the vertical component (Figure 9) even for short differences in distance (less than 11 km). Thus, the site response estimated for those sites, based on the HVSR technique must be used with caution.

We also calculated signal to noise ratios for each station and both horizontal components (radial and transversal). We found that records with epicentral distance greater than 300 km tend to have signal/noise close to one for small to moderate earthquakes, and consequently we continue the analyses using only records with distances less than 300 km. Since all the records of station NE70 were at longer distances we did not use this site. Figure 10 shows signal to noise ratios calculated for all the sites using the closer and most distant events recorded at those stations. Station NE79, the reference site choose previously, is on solid rock and shows signal to noise ratio above one in the whole used frequency band. We found that in general, the signal to noise ratio is above 2 between 0.4 and 10 Hz for all stations.

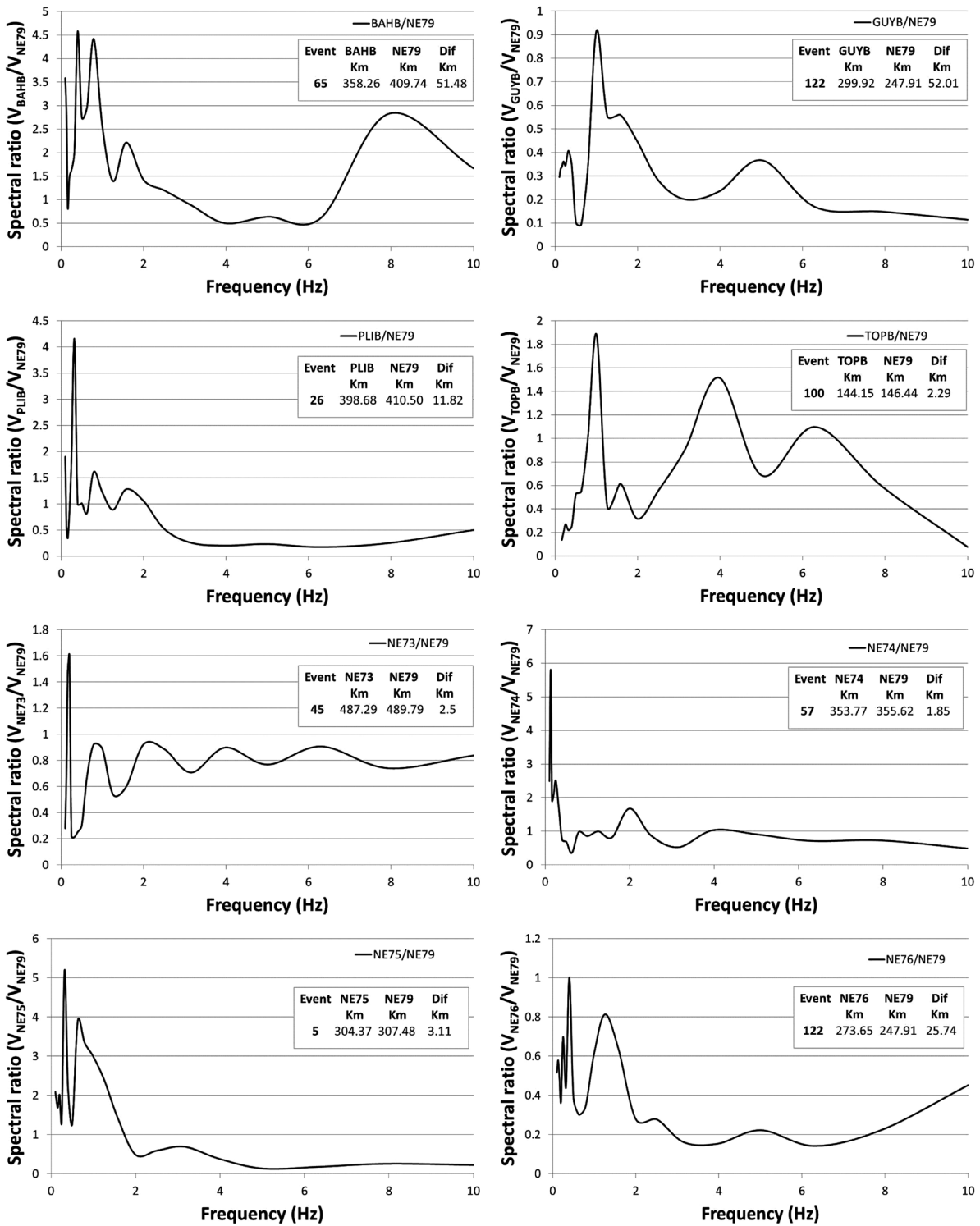


Figure 9. Vertical-component spectral ratios between the target stations and station NE79 (reference site), from events recorded simultaneously at both sites and with similar epicentral distances.

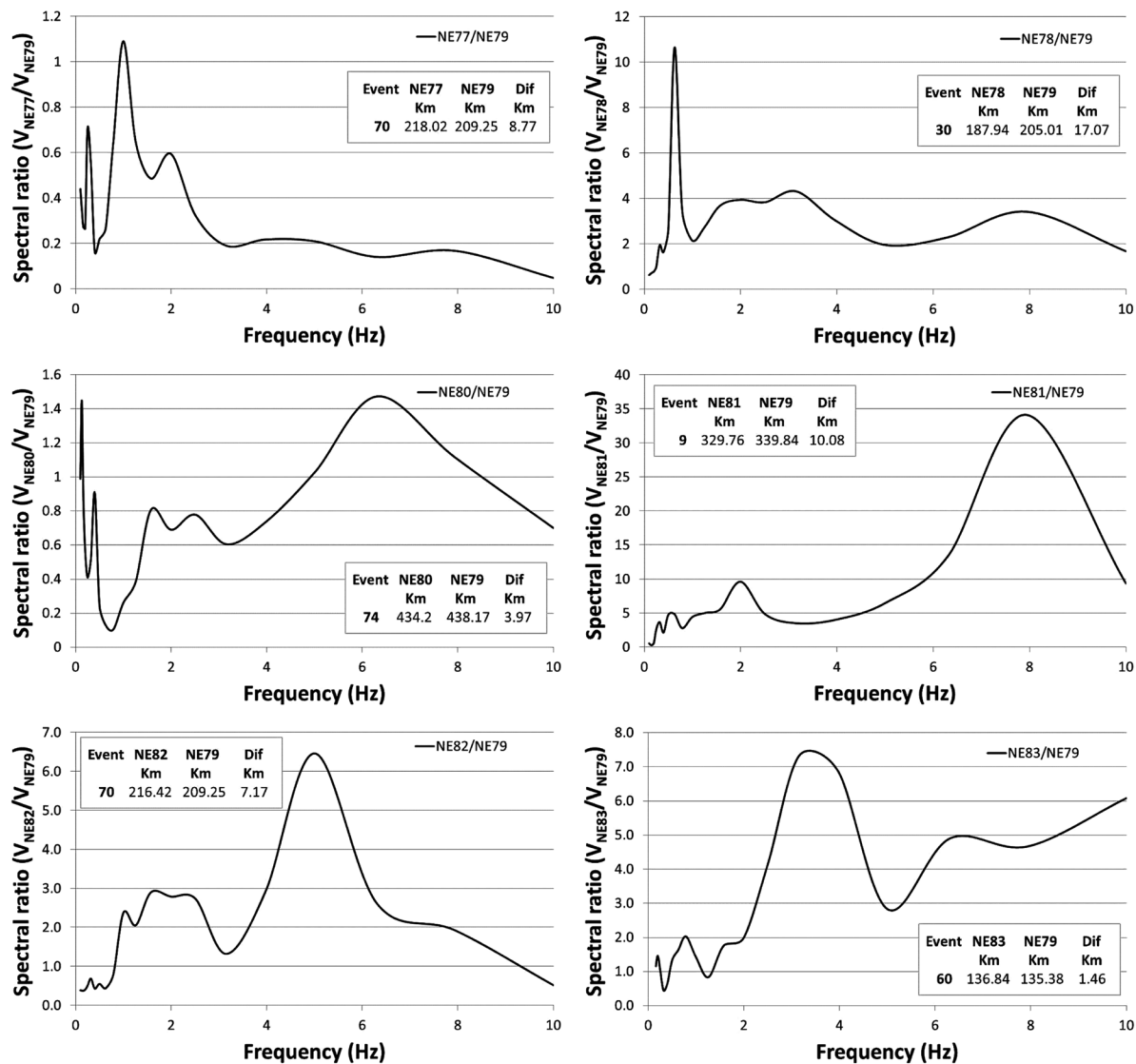


Figure 9. Continue.

Results

We estimated the site response of the stations of the NARS-Baja and RESBAN networks using the HVSR method. Figure 11 shows the average HVSR, for all stations, calculated using radial and transversal components. This figure shows that stations NE74, NE80, NE81 and NE84, all in group III (Table 1), present amplification factors above 4, while stations in groups I and II have amplification factors around 3 or less. There are several stations in group III (NE70, NE72, NE78, and NE83) with smaller amplification (less than 3.2) suggesting that the soil at those sites is better consolidated. These sites also tend to have a higher fundamental frequency (2.0-5.0 Hz) than other sites in group III which have a

natural resonance frequency less than 0.8 Hz. The reference site NE79 (group I) is mostly amplification free and it has a fundamental frequency close to 7.0 Hz, presenting a small amplification at that frequency (a factor of less than 2.5).

To verify these results we determined spectral ratios for two soil sites (stations NE74 and NE80) using the average site response of rock sites as reference. We can observe in Figure 12 that the amplification factors obtained for the soil sites are consistent with the previous results (Figure 9), indicating that the HVSR method provides reliable site amplifications. The peak amplifications are at the same frequencies and the shape of both functions is similar. However, the standard

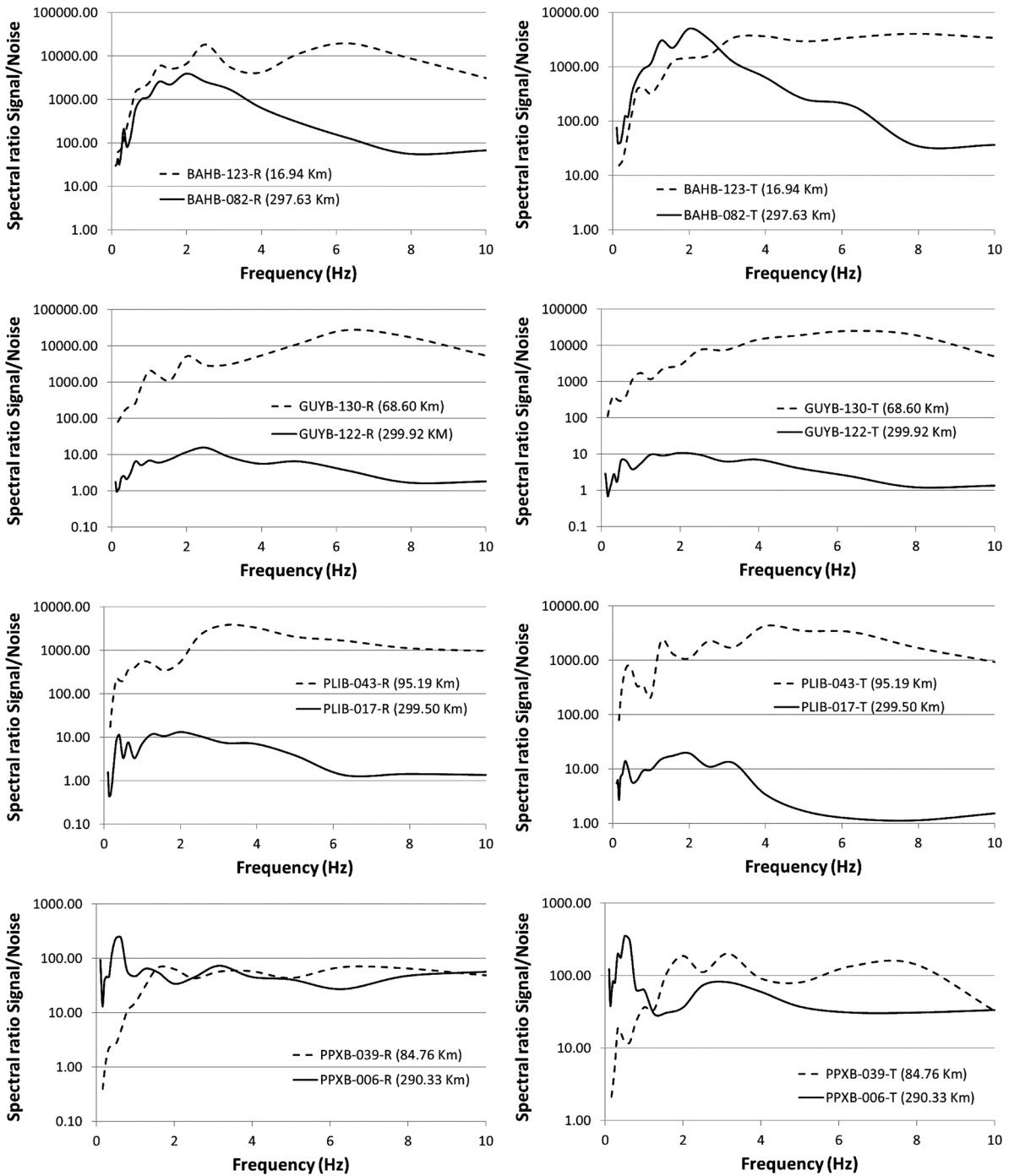


Figure 10. Signal to noise ratios. The plots on the right correspond to the radial component and those to the left, to the transversal component. The number in parenthesis indicates the epicentral distance.

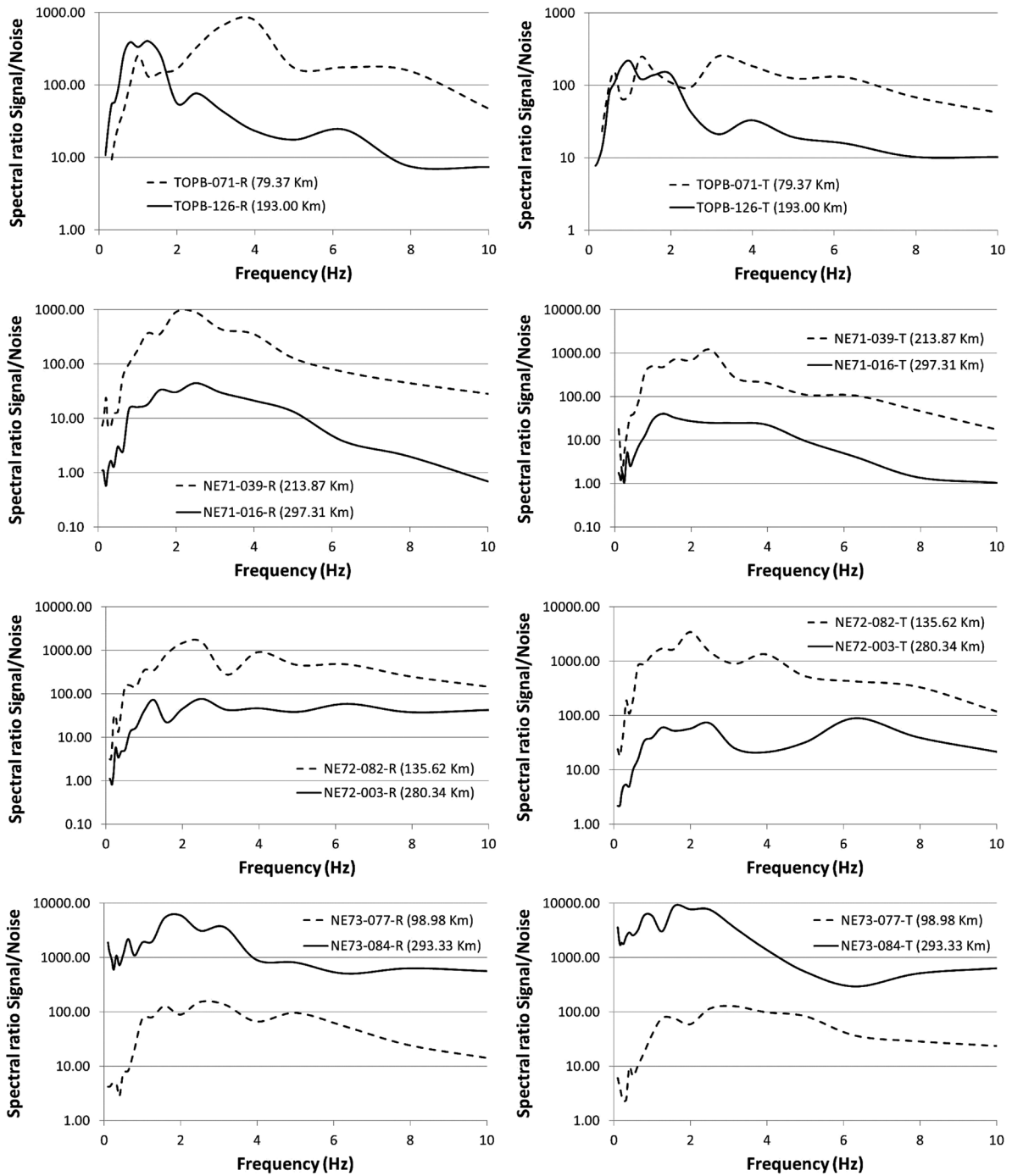


Figure 10. Continue.

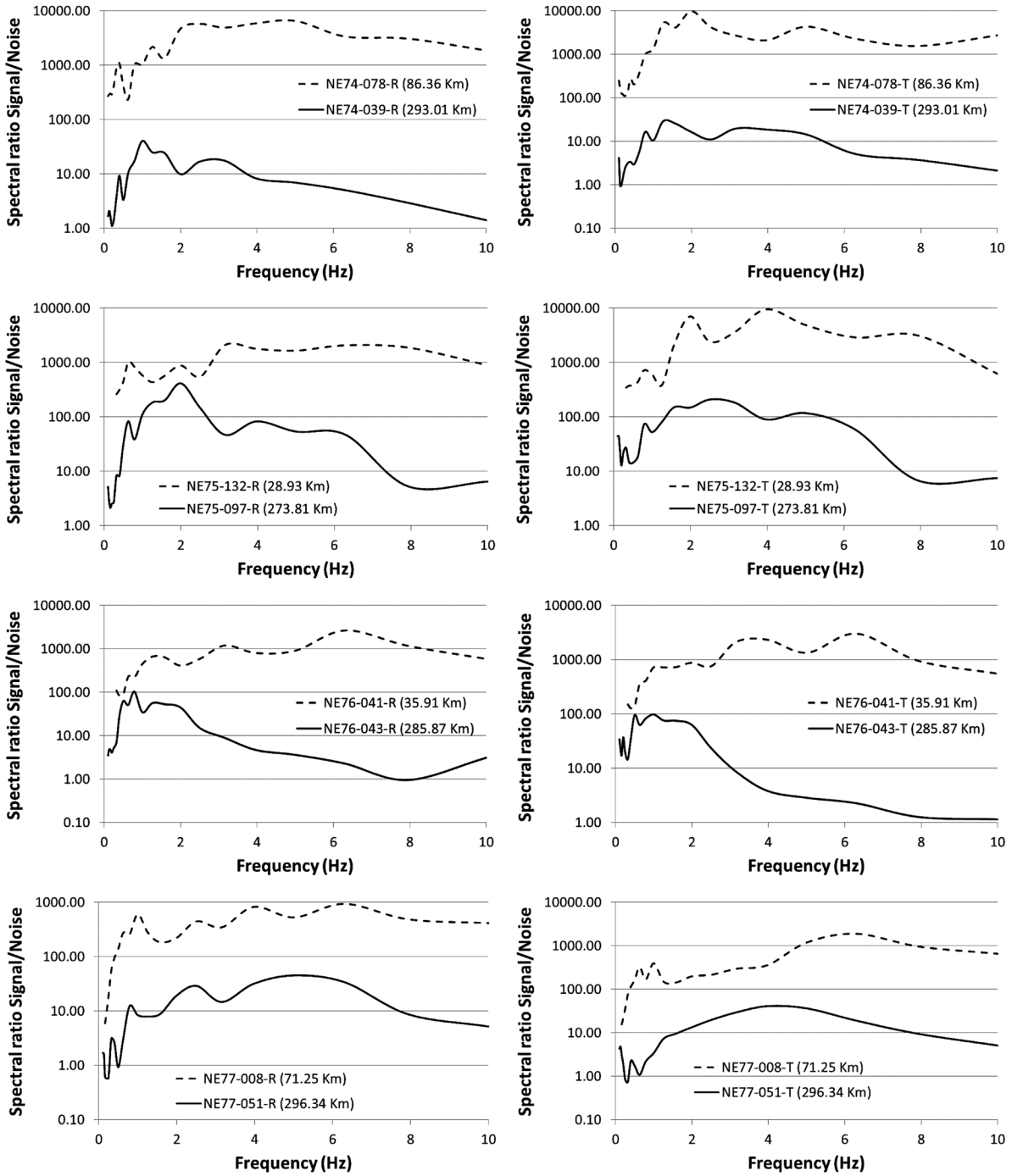


Figure 10. Continue.

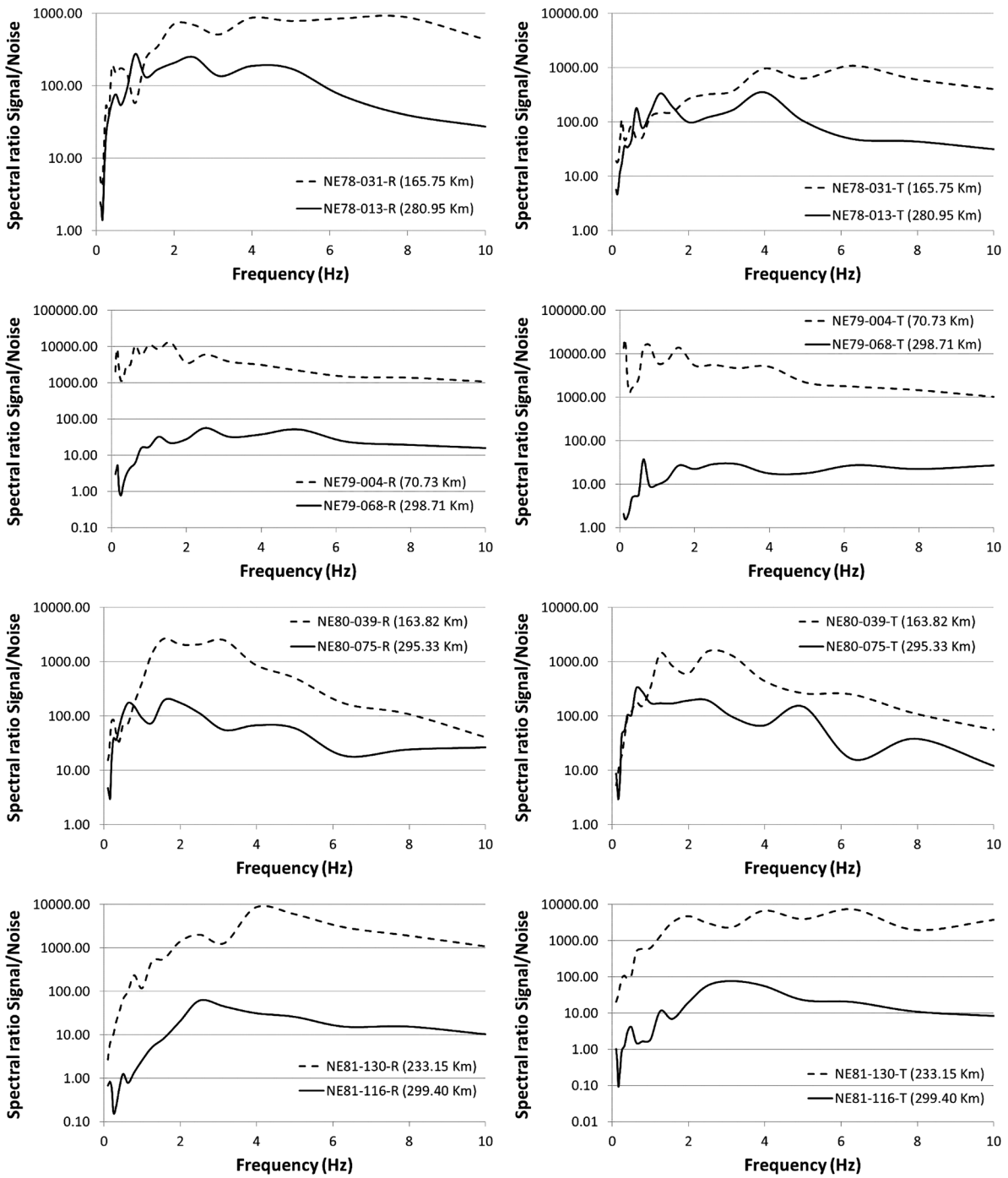


Figure 10. Continue.

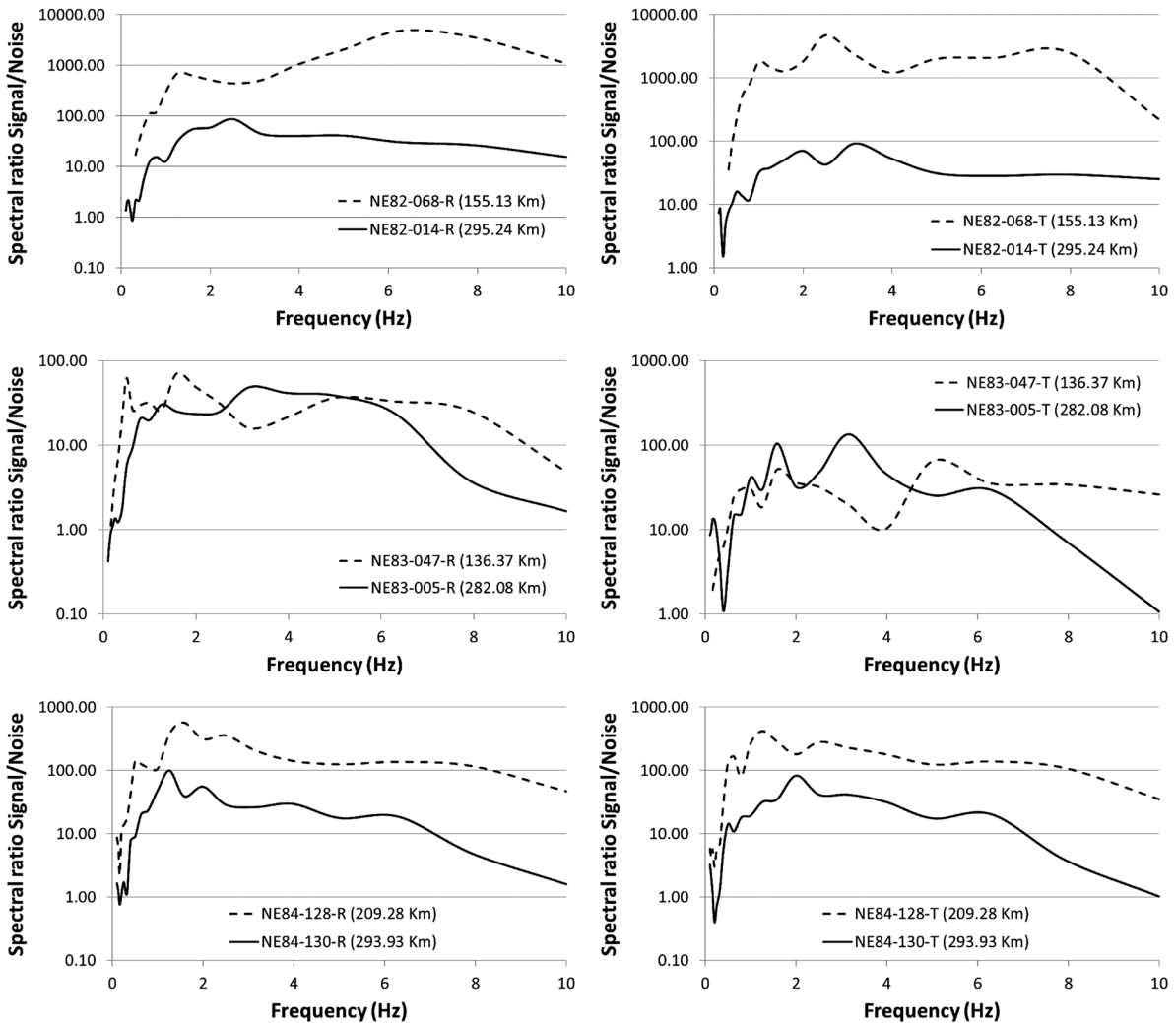


Figure 10. Continue.

spectral ratio technique tends to give slightly lower amplifications because the rock sites are not completely amplification free.

We also calculated the average HVSR for different azimuth ranges, finding that four (NE74, NE78, NE80, NE81) of the 20 stations analyzed present a dependence of site amplification with the azimuth and that this dependence varies from station to station. These four stations show larger amplification factors, larger than three, than the other sites. The small amplifications observed at the other stations made it unclear whether their site response has any azimuth dependence. Figure 13 shows an example of a site (station NE74) with clear azimuthal dependence on the transversal component. In the azimuth range from 46° to 89° , corresponding to ray-paths

from events located in the southern Gulf of California, the peak amplification (a factor above 8) occurs at 1.3 Hz at the transversal component and then the amplification factor decreases down to a factor of 2 for other azimuths at that frequency. Figure 14 shows the average HVSR of different azimuth ranges calculated for station NE82. This site of group II (Table 1) presents low amplifications and it seems to be invariant with azimuth. Station NE82 is one of the stations with low amplification and unclear or insignificant azimuthal dependence.

To evaluate if there is a persistent direction of amplification in the site response, we evaluate the amplification for rotated HVSR in the range of 20° to 180° . We selected station NE81 of group III because this station presents

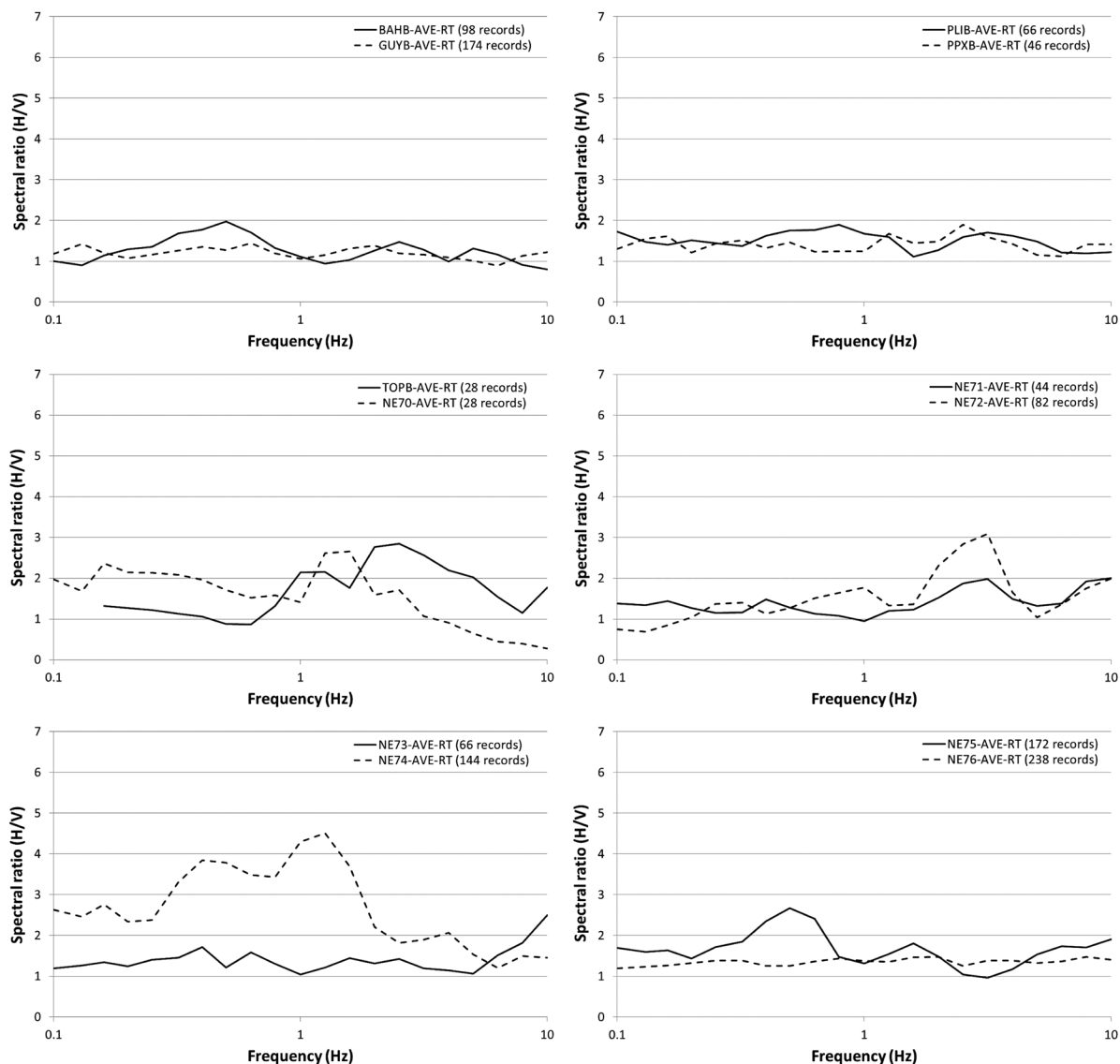


Figure 11. Average value of HVSR obtained using both horizontal components (radial and transversal).

important site amplification at the natural resonance frequency of the site (Figure 11 and 12). Figure 15 shows average rotated HVSR of both radial and transversal components calculated using events 40 and 101 (Table 2) recorded at station NE81. We calculated the average HVSR rotating the records every 20° from 20° to 180° (e.g., Pischiutta *et al.*, 2012). It is clear in Figure 15 that there is not a preferred average amplification direction related to angle of rotation and that the horizontal components (NS and EW) used give a single average rotated record. The dependence of the amplification with azimuth becomes evident when radial and transversal components are treated separately.

We also explore whether the site response depends on the magnitude of the earthquakes by comparing the average HVSR calculated from both horizontal components for small ($M < 3.7$) and larger magnitude ($M=5.9-6.6$) events (Figure 16). Since stations GUYB and PLIB (top and middle frames in Figure 16) are low-amplification sites (amplification factors below 2, Figure 11), these stations do not show magnitude dependence. For station GUYB (upper frame in Figure 16) at 0.63 Hz, the event with $M=6.4$ (dashed line) produced larger amplification than the other events but the amplification level is low (below a factor of 2.5). For station PLIB (middle plot in Figure 16) at 0.79 Hz, the amplification is also

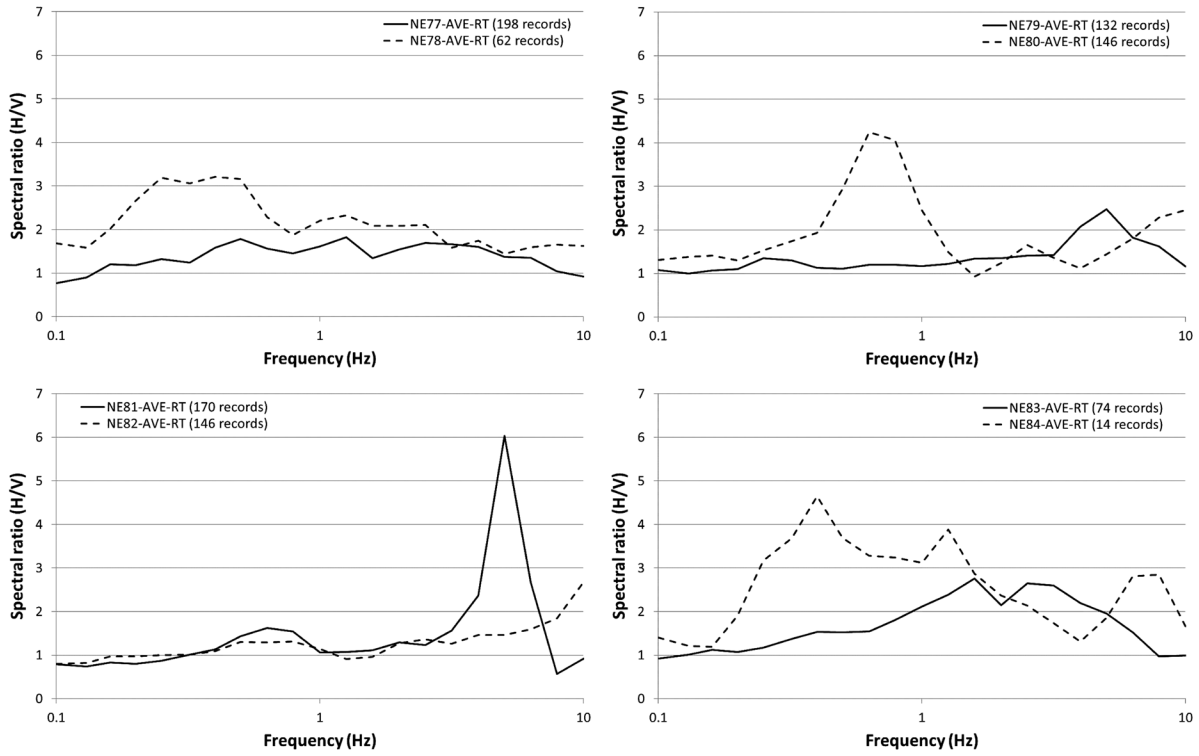


Figure 11. Continue.

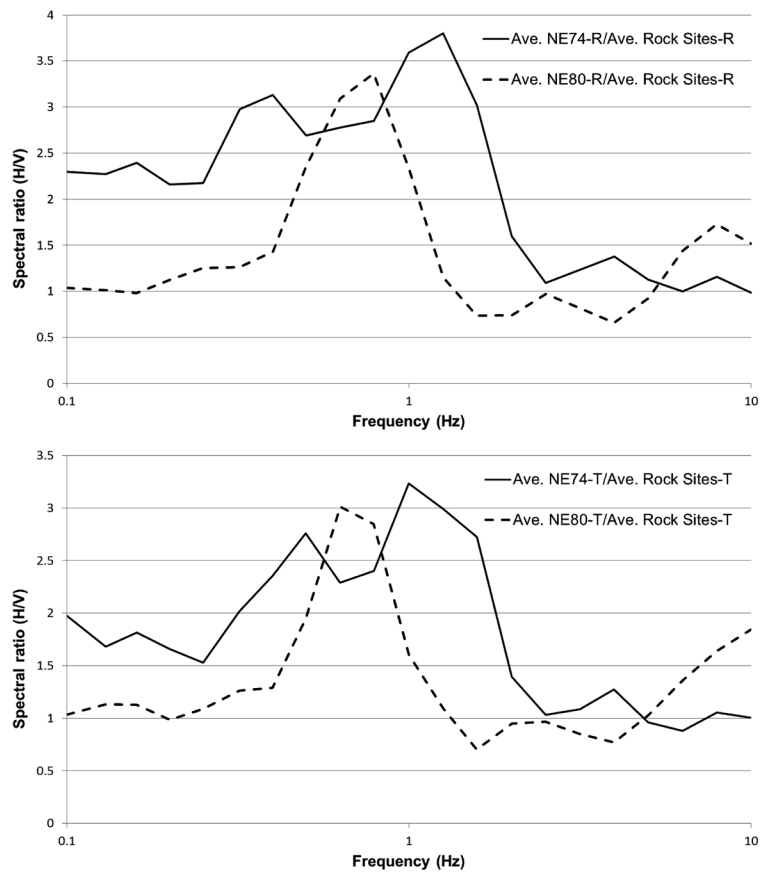


Figure 12. Average spectral ratios (HVSr) calculated for soil-sites NE74 (solid line) and NE80 (dashed lines), using the average response of rock sites as reference.

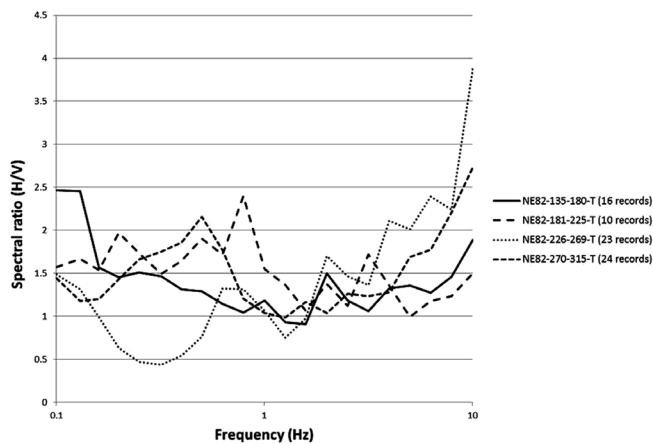
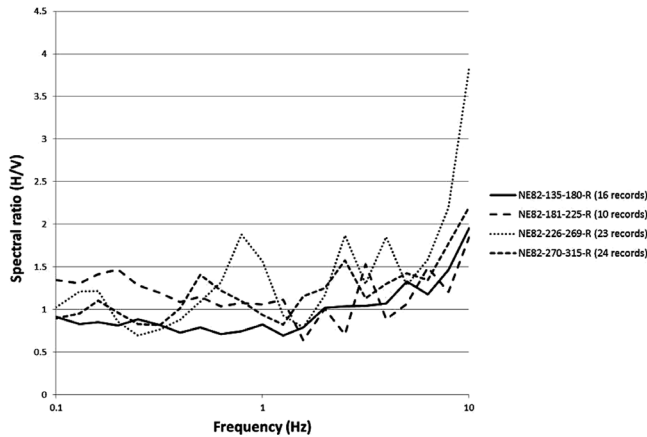
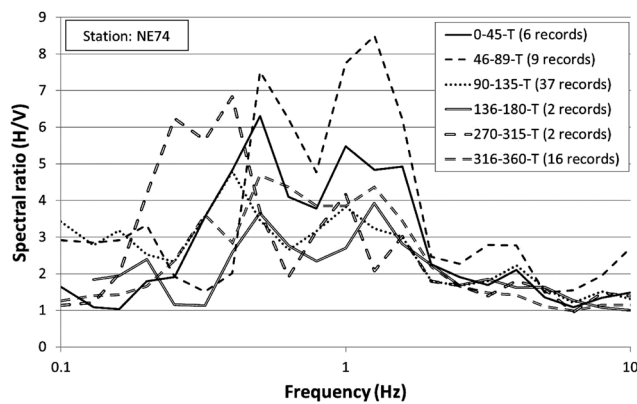
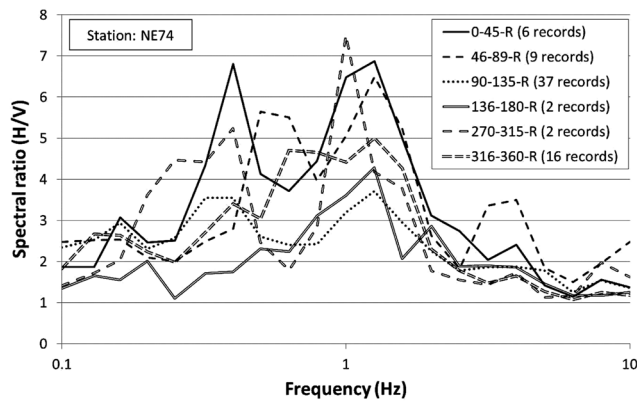


Figure 13. Average HVSR for different azimuth ranges for station NE74. Top frame displays radial component and bottom, transversal component.

Figure 14. Average HVSR of different azimuth ranges calculated for station NE82 for radial (upper frame) and transversal components (lower frame).

Figure 15. Average rotated HVSR components calculated using events 40 and 101 (Table 2) recorded at station NE81.

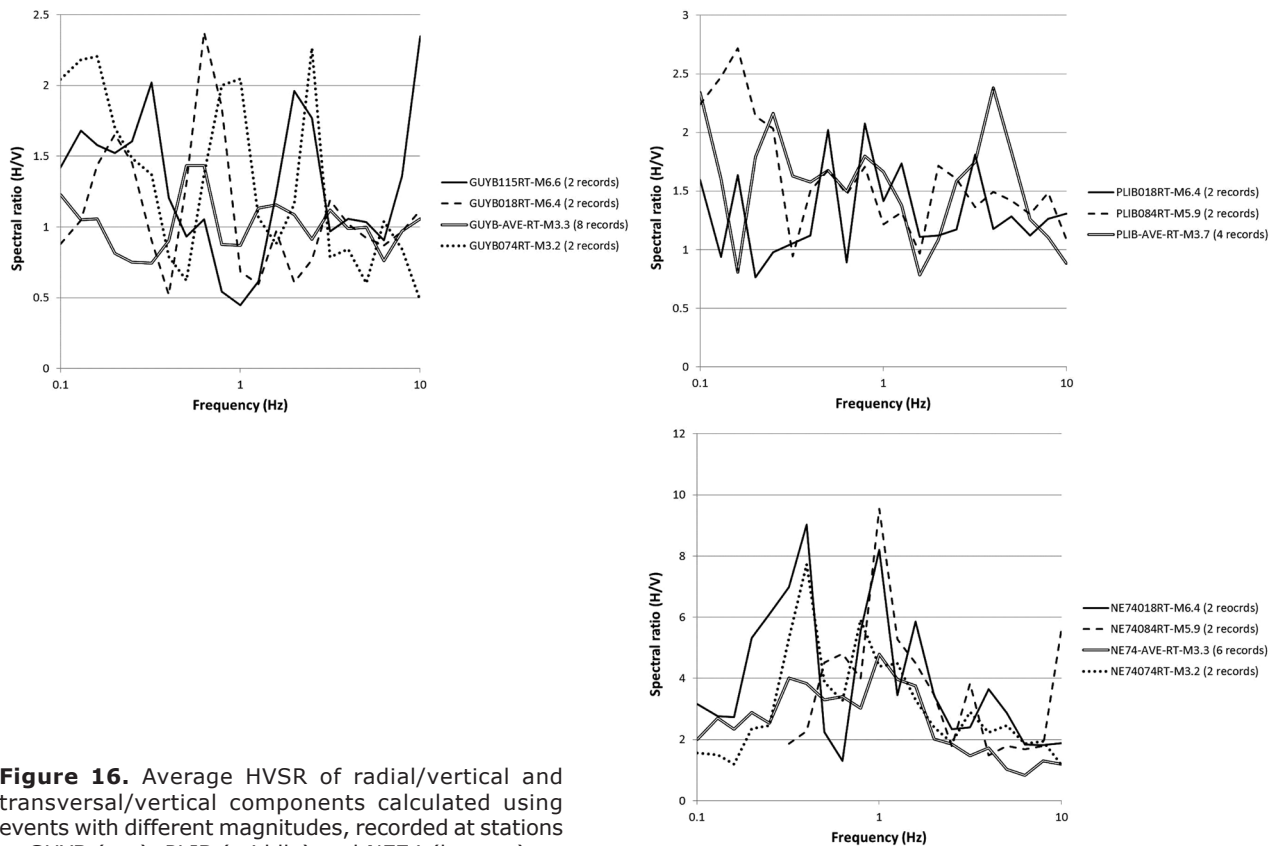
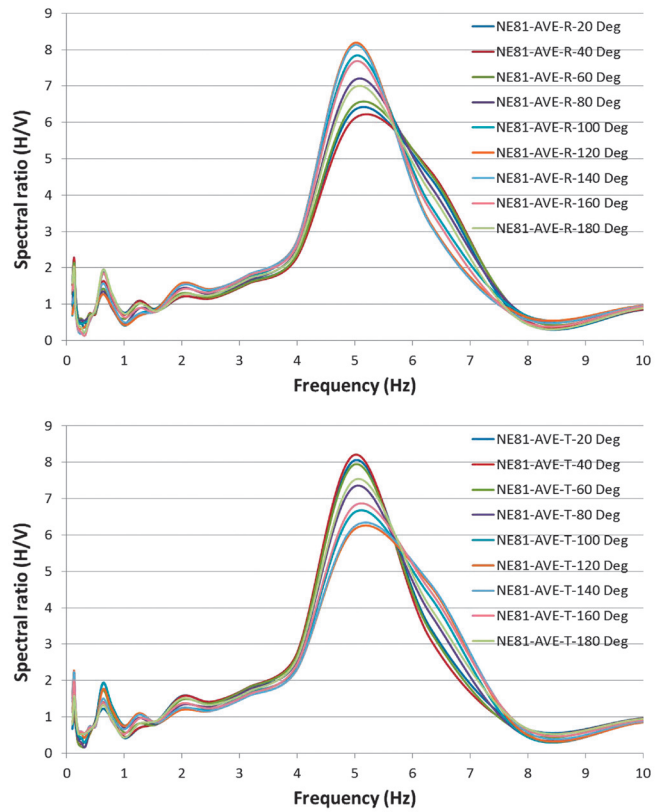


Figure 16. Average HVSR of radial/vertical and transversal/vertical components calculated using events with different magnitudes, recorded at stations GUYB (top), PLIB (middle) and NE74 (bottom).

insignificant for the three magnitudes ($M=3.7$, $M=5.9$ and $M=6.4$). However, station NE74, a site with higher amplification levels (group III), up to a factor of 4.5 (Figure 11), shows an important increase of the amplification factor with increasing earthquake magnitude (bottom frame in Figure 16). For instance, at 0.4 Hz the HVSR calculated with the $M=6.4$ event (solid line) has higher amplification than that calculated with the $M=3.3$ (double line) and the $M=3.2$ (dotted line) events. At 1 Hz the HVSR calculated with the $M=6.4$ (solid line) and $M=5.9$ (dashed line) events have amplification factors above 8, while for the $M \leq 3.3$ events the amplification factor is below 5. The HVSR calculated with the transversal component (Figure 17), where the SH waves are expected to be present, clearly shows that events with higher magnitude generate larger amplification than smaller magnitude events. At 0.4 Hz the $M=6.4$ event (solid line in Figure 17) generated an amplification factor of 14 while the $M=3.2$ (dotted line) event reached an amplification factor below eight. At 1 Hz the $M=5.9$ (dashed line in Figure 17) produced an amplification of 15 while the events with $M \leq 3.2$ generated amplifications below 7. The amplification at 1 Hz of the $M=6.4$ event (solid line) is smaller than that of the $M=5.9$ event, suggesting that the station NE74 possibly presented a non-linear response at 1 Hz for the $M=6.4$ event.

Discussion and conclusions

We determined site response functions of 20 stations to evaluate possible azimuth-dependent amplification. We found that stations NE74, NE78, NE80, NE81 and NE84, of site characterization group III, present the largest average ground motion amplification factors

(above 3) (Figure 11). The frequency range where the amplification is prominent varies from 0.25 to 2.0 Hz; with the exception of station NE81 where the maximum amplification factor (around 6) occurs in the frequency range from 5.0 to 6.3 Hz. We also observed that these five sites with larger average amplification present this feature in both radial and transversal components, and show a clear dependence on the source back-azimuth. This dependence of site amplification can be explained by the likely asymmetry of the geologic characteristics under the sites, including layer thickness and velocity variations with azimuth.

Most stations are located on hard rock (group I and II in Table 1) and have low site amplification, but those with amplification factors above 3 (sites in group III) seem to be strongly influenced by the earthquake back-azimuths. The range of frequencies and azimuths where the major site amplifications occur are different for each station. The stations that present the largest site amplifications on the transversal component are NE74, NE81 and NE83, with amplification factors above 5. NE74 (Figure 13) presents the largest amplifications for azimuths that vary from 270° to 315° (between 1 and 1.25 Hz) and for azimuths varying from 46° to 89° (between 0.5 and 2.0 Hz) for radial and transversal components, respectively. Figure 18 shows the average values of HVSR for station NE76 for different azimuths and horizontal components. Station NE76 (Figure 18) presents the largest amplifications, above 12, on the transversal component, from 270° to 315° and at frequencies from 0.79 to 3.16 Hz. This site is a clear example of the effect of the azimuth on the site response.

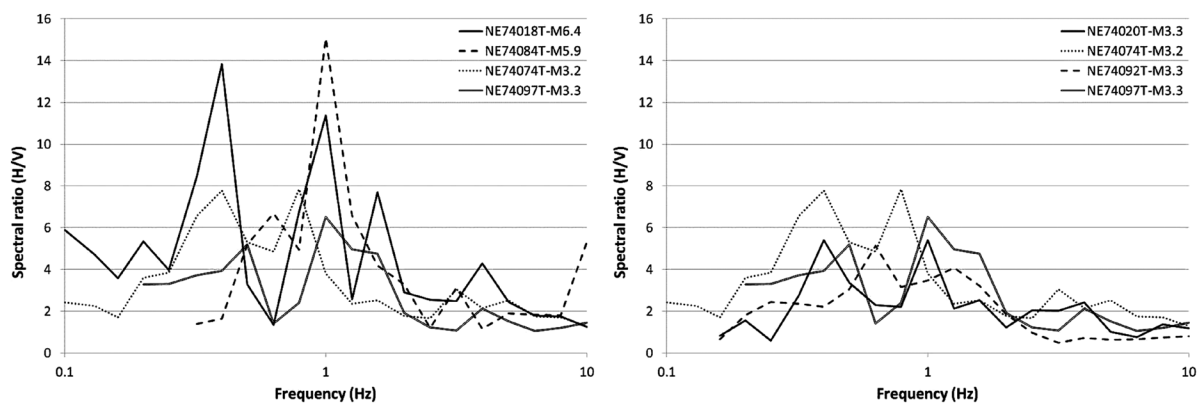


Figure 17. HVSR calculated with the transversal component showing dependence with magnitude at station NE74. Left frame compares HVSR from events with magnitudes from 3.3 to 6.4 and the right frame shows amplification levels estimated from small magnitude ($M=3.2-3.3$) events.

We analyzed the possible relation between average site amplification and source magnitude (average between radial and transversal components). We first determined the natural resonance frequency (f_n) of the sites, as a reference, selecting the frequency where the first peak of the average HVSR occurred (Figure 11). Then, we compared the average HVSR of the radial and transversal components, calculated from earthquakes with different magnitudes. Figure 16 shows an example for three stations: GUYB ($f_n = 0.63$ Hz), PLIB ($f_n = 0.79$ Hz) and NE74 ($f_n = 0.4$ Hz). We can see from this figure that there is not a clear relation between the amplification

factor and the event magnitude for the sites with low amplification (stations GUYB and PLIB). However, for site NE74 (lower plot in Figure 16), the amplification generated by the $M=6.4$ earthquake is larger than that produced by the lower magnitude events. In general, the softer the soil, the higher the amplification is. Attenuation studies in the Gulf of California (Vidales-Basurto *et al.*, 2014) indicate that P waves attenuate considerably more than S waves. Thus, P waves from small magnitude earthquakes disturb the geotechnical characteristics of the soils less than moderate and large magnitude events. For the regional events that we analyzed, most of the source-

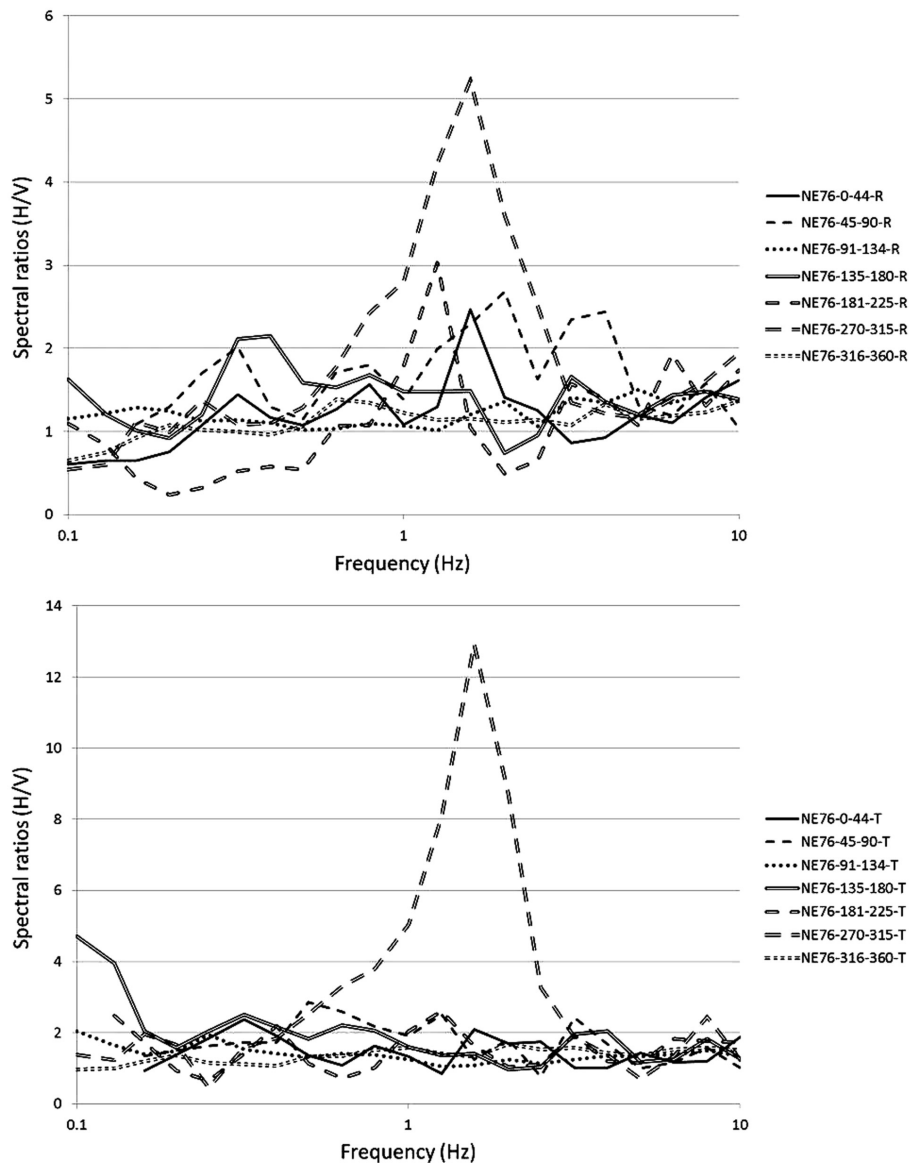


Figure 18. HVSR calculated for station NE76 for different azimuth ranges. Radial (upper frame) and transversal components (lower frame).

station distances are above 200 km and the time between the first *P* arrival and the first *S*-wave arrival is larger than 25 s. This gives time to the *P* wave to shake the soil-site enough to decrease the rigidity so that when the *S* waves arrive to the site, the shear waves find a softer soil and thus the amplification tends to increase. Thus, to explain the observed increase of site amplification with increasing magnitude, we propose that the compressional waves arriving previous to the shear waves change the geotechnical characteristics of the soils. The disturbance will depend of the shaking intensity generated by the *P* waves and this will increase with the magnitude of the earthquakes.

In conclusion, we find that stations of the NARS-Baja and RESBAN networks in the group site III (Table 1) present site effects with average horizontal amplifications factors above 3. We also observe that these stations show important azimuthal dependence. The natural resonance frequency and the azimuth of incoming waves that generate the largest site effects observed vary for each station. Station sites with significant amplification factors (above 3) also show increasing amplification with increasing source magnitude.

Acknowledgments

The operation of the RESBAN network has been possible thanks to the financial support of the Mexican National Council for Science and Technology (CONACYT) by means of the project CB-2011-01-165401(COC059). Funding for the first author comes from the postdoctoral program of CONACYT. We are also grateful for the technical assistance given by Antonio Mendoza and Arturo Pérez Vertti. Sergio Mayer and Arturo Pérez Vertti made the field survey to determine the geologic characteristics of the sites. We thank the two anonymous reviewers for their comments and suggestions.

References

- Castro R.R., Pérez-Vertti A., Mendez I., Mendoza A., Inzunza L., 2011, Location of moderate size earthquakes recorded by the NARS-Baja array in the Gulf of California region between 2002 and 2006. *Pure Appl. Geophys.*, 168, 1279-1292, DOI 10.1007/s00024-010-0177-y.
- Clayton R.W., Trampert J., Rebollar C.J., Ritsema J., Persaud P., Paulssen H., Pérez-Campos X., van Wettum A., Pérez-Vertti A., diLuccio F., 2004, The NARS-Baja array in the Gulf of California Rift Zone. *Margins Newsletter*, 13, 1-4.
- Cultrera G., Rovelli A., Mele G., Azzara R., Caserta A., Marra F., 2003, Azimuth-dependent amplification of weak and strong motions within a fault zone (Nocera Umbra, central Italy). *J. Geophys. Res.*, 108, No. B3, 2156, doi: 10.1029/2002JB001929
- Lermo J., Chávez-García F.J., 1993, Site effect evaluation using spectral ratios with only one station. *Bull. Seismol. Soc. Am.*, 83, 1574-1594.
- Nakamura Y., 1989, A Method for dynamic characteristics estimation of subsurface using microtremor on the ground surface. *Quarterly Report of Railway Technical Research Institute (RTRI)*, 30, 1.
- Nogoshi M., Igarashi T., 1970, On the propagation characteristics of microtremor, *J. Seismol. Soc. Japan*, 23, 264-280.
- Pedersen H.A., Campillo M., Sánchez-Sesma F.J., 1995, Azimuth dependent wave amplification in alluvial valleys. *Soil Dynamics and Earthquake Engineering*, 14, 289-300.
- Pischiutta M., Salvini F., Fletcher J., Rovelli A., Ben-Zion Y., 2012, Horizontal polarization of ground motion in the Hayward fault zone at Fremont, California: dominant fault-high-angle polarization and fault-induced cracks. *Geophys. J. International*, 188, 3, 1255-1272, doi:10.1111/j.1365-246X.2011.05319.x.
- Trampert J., Paulsen H., Van Wettum A., Ritsema J., Clayton R., Castro R., Rebollar C., Pérez-Vertti A., 2003, New Array Monitors Seismic Activity Near the Gulf of California in México, *EOS, Trans. Am. Geophys. Union*, 84, 29-32.
- Vidales-Basurto C.A., Castro R.R., Huerta C.I., Sumy D.F., Gaherty J.B., Collins J.A., 2014, An attenuation Study Body Waves in the South-Central Region of the Gulf of California, México. *Bull. Seismol. Soc. Am.*, 104, 4, doi: 10.1785/0120140015.

Relationship between the minima of the horizontal magnetic component measured in Mexico and the Dst and SYM-H indices for geomagnetic storms with $Dst \leq -100nT$ during the descending phase of solar cycle 23

Julia Lénica Martínez-Bretón*, Blanca Mendoza Ortega and Esteban Hernández-Quintero

Received: October 19, 2015; accepted: January 13, 2016; published on line: April 01, 2016

Resumen

En este trabajo se analizan las diferencias en aparición de mínimos entre los índices Dst, SYM-H y la componente horizontal H medida en el Observatorio Magnético Teoloyucan (TEO) ubicado en México. Se calculó esta diferencia en tiempo universal para 15 tormentas geomagnéticas ($Dst \leq -100nT$) que ocurrieron durante la fase descendente del ciclo solar 23. Notamos que cuando TEO se encontraba en el lado día, amanecer y atardecer, la diferencia horaria fue negativa, indicando que el mínimo apareció por primera vez en el Dst y SYM-H reportado por Kyoto y después en H medido por TEO. Por otra parte, cuando TEO se encontraba cercano a la medianoche la diferencia es positiva, lo que indica que el mínimo se reportó antes en TEO y después en Dst. Notamos que 14 de las 15 tormentas geomagnéticas siguieron este comportamiento, excepto la más intensa de la muestra. Para las 14 restantes el tiempo de desfase en los mínimos no parece depender de la intensidad de la tormenta geomagnética, sino de la intensidad de los sistemas de corrientes presentes.

Palabras clave: corrientes de la Ionosfera, DST, SYM-H, tormentas geomagnéticas intensas, relaciones solar-terrestres.

Abstract

In this paper, we analyze the time delay between the occurrence of the minima in the geomagnetic Dst, SYM-H indices and the horizontal magnetic component (H) measured in the Teoloyucan Magnetic Observatory (TEO) of Mexico. This difference was calculated in Universal Time for 15 geomagnetic storms ($Dst \leq -100nT$) occurred during the descending phase of solar cycle 23. We found that, when the TEO was at the dayside, dawn and dusk, the time difference was negative, indicating that the minimum appeared first in the Dst, SYM-H reported by Kyoto, and afterwards in the H reported by TEO. On the other hand, when the TEO was close to midnight the difference was positive, indicating that the minimum occurred first at TEO and afterwards in Dst. We noticed that 14 out of 15 geomagnetic storms followed this behavior, except the most intense one of the sample. For the rest of the storms, it seems that the cause of the delay is not the intensity of the magnetic field at minimum but the intensity of the current systems present during the storm occurrences.

Key words: ionosphere currents, Dst, SYM-H, intense geomagnetic storms, solar-terrestrial relations.

J.L. Martínez-Bretón*
Posgrado en Ciencias de la Tierra
Universidad Nacional Autónoma de México
Ciudad Universitaria, 04510
México D.F., México
*Corresponding autor: lenica@geofisica.unam.mx
lenica_nube@yahoo.com.mx

B. Mendoza
E. Hernández-Quintero²
Instituto de Geofísica
Universidad Nacional Autónoma de México
Ciudad Universitaria, 04510
México D.F., México

Introduction

Geomagnetic activity in general and geomagnetic storms (GS) in particular, are manifested through a series of processes involving current systems that induce magnetic fields, measured by several geomagnetic ground observatories.

The intensity of the GS is given by the geomagnetic Dst (Disturbance storm time) (Sugiura, 1964) index. During the GS, there are several current systems at play. The storm starts with the momentum and plasma transfer from the solar wind to the magnetosphere (Dessler and Parker, 1959), which produces an intensification of the magnetopause currents, the field aligned currents and the ring currents; the latter produce the characteristic decrease in the Dst index. There is also the partial ring current that is one of the current systems located in the Northern and Southern Hemispheres at the geomagnetic equatorial plane, and closed through the ionospheric field aligned currents (Kalegaev, *et al.*, 2008; Li, *et al.*, 2011; Lockwood, 2013) and the magnetotail current system (Alexeev, *et al.*, 1996). The intensity of each current system is a consequence of the energy injected to the magnetosphere by the solar wind (Clúa *et al.*, 2013; Patra *et al.*, 2011).

The Dst index was created 50 years ago (Hamilton *et al.*, 1988), in order to have a quantitative measurement of the ring current. Four observatories monitor the Dst: Honolulu (Longitude (E) 201.98°, Latitude 21.32°), San Juan (Longitude (E) 293.88°, Latitude 18.11°), Hermanus (Longitude (E) 19.22°, Latitude -34.40°) and Kakioka (Longitude (E) 140.18°, Latitude 36.23°) located at mid and low latitudes (see Figure 1) where the influence of the equatorial electrojet is minimum. Each observatory reports the horizontal magnetic field intensity (H), and the Dst is constructed from these four reports. The Dst minimum indicates the moment of occurrence of the GS in universal time (UT) (Mandea and Korte, 2011; Campbell 2004; Mayaud 1980; Sugiura, 1964).

The SYM-H index describes the geomagnetic disturbance field at mid-latitudes with a 1 min resolution. Dst and SYM-H are argued to be essentially the same (e.g., Sugiura and Poros, 1971) as their numerical differences are small. However, a recent work (Katus and Liemhon, 2013) shows that, although their correlation is 0.9, they are inherently different, because each index applies different methods to remove irrelevant fluctuations.

The derivation procedure for both the Dst and the SYM-H essentially consists for the following four steps: (1) Subtraction of the geomagnetic main field and the Sq (solar quiet daily variation) field to calculate the disturbance field component. (2) Coordinate transformation to a dipole coordinate system. (3) Calculation of the longitudinally symmetric component (i.e. six-station average for SYM-H and four stations average for Dst) and the asymmetric component (i.e. disturbance field minus the symmetric component). (4) Derivation of the asymmetric indices (i.e. the range between the maximum and the minimum asymmetric fields), <http://wdc.kugi.kyoto-u.ac.jp/aeasy/asy.pdf>

As a first approximation, the ring current is a toroidal westward current system centered at the equatorial plane, at a geocentric distance between 2 and 9 terrestrial radii (Bogdanova *et al.*, 2014). It is formed mainly by positive ions and ~25% electrons (Liu *et al.*, 2005), with energies between tens and hundreds keV and subjected to an azimuthal drift. The ring current increases its density during the GS main phase, decreasing during the recovery phase. The loss mechanisms are more efficient near dawn and dusk (Le, 2013), which explains why the ring current and the ionosphere control the electric fields in the interior of the magnetosphere at dawn and dusk (Bogdanova *et al.*, 2014). These effects are due to the electric fields that appear during the dusk near the equatorial ionosphere (Tsurutani *et al.*, 2012). The magnetotail currents are also systems that strongly contribute to the Dst decrease during a GS. The ring current is very important for the ionosphere/magnetosphere dynamics (Hamilton *et al.*, 1988). It has been shown that the O⁺ ions, of ionospheric origin, contribute significantly to the plasma pressure of the inner magnetosphere during a GS (Keika *et al.*, 2013; Daglis *et al.*, 1999; Welling *et al.*, 2011). Also, strong ionospheric effects associated with a GS have been reported. The ionospheric local currents affect the H, thus the measurements of the geomagnetic observatories depend on the latitude, and the Magnetic Local Time (MLT) (Shinbori *et al.*, 2012; Ahn *et al.*, 2002).

There is a strong dependence of the ionospheric conductivity and the decrease of H. Also, there is a seasonal dependence of the sudden storm commencement amplitude and the MLT, according to the current systems involved (Shinbori *et al.*, 2012).

The purpose of the present work was to determine, and evaluate the difference in time during a GS between the occurrence of

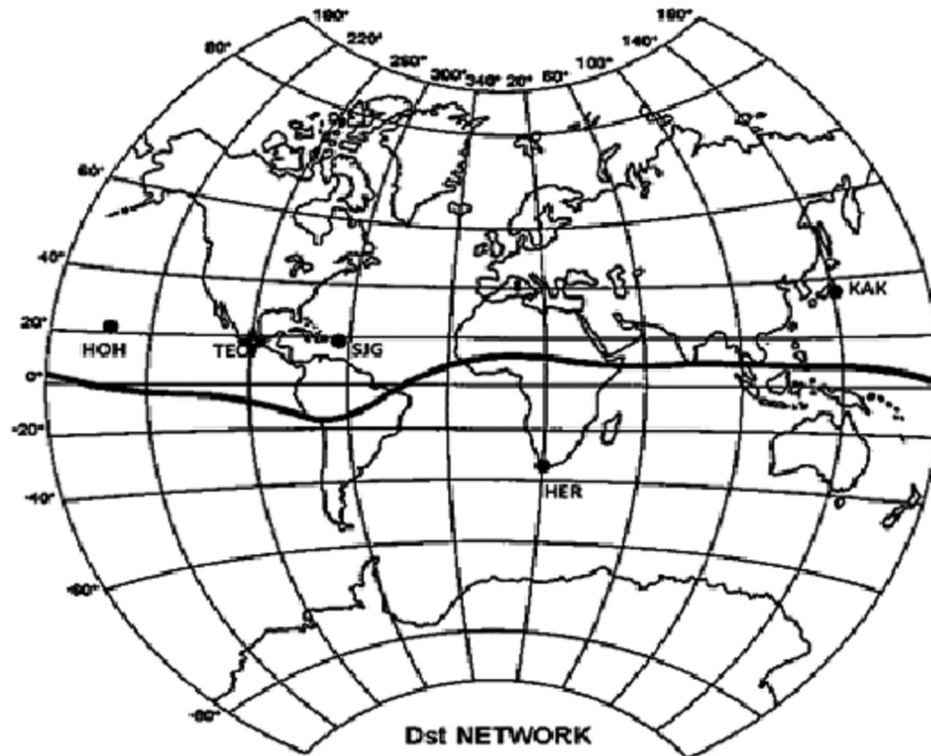


Figure 1. Map showing the location with circle of the four stations that are used to construct the Dst index: Honolulu (Longitude (E) 201.98°, Latitude 21.32°), San Juan (Longitude (E) 293.88°, Latitude 18.11°), Hermanus (Longitude (E) 19.22°, Latitude -34.40°) and Kakioka (Longitude (E) 140.18°, Latitude 36.23°). The star indicates the location of the Teoloyucan Magnetic Observatory (Longitude (E) 260.81°, Latitude 19.74°) (<http://wdc.kugi.kyoto-u.ac.jp/dst/dir/dst2/onDstindex.html>).

the minima in Dst, SYM-H and H measured in the Teoloyucan Magnetic Observatory (TEO) of Mexico. Knowing these differences is important for research concerning local geomagnetic phenomena.

Methods

TEO is located in Mexico at Longitude (E) 260.81°, Latitude 19.74° (see Figure 1). The vector of the magnetic field has been continuously monitoring since 1914, being one in a worldwide network of magnetic observatories and belonging to the international INTERMAGNET project. Besides, TEO is the backbone of the Magnetic Service of the Geophysics Institute of the National Autonomous University of Mexico (Instituto de Geofísica de la Universidad Nacional Autónoma de México) and the hub of a broad range of geophysical and magnetic field research in Mexico.

The data base we use corresponds to the TEO H component (TEO-H) from January 2003 to December 2006 corresponding to the descending phase of solar cycle 23 (<http://>

www.intermagnet.org/data-donnee/download-eng.php and <http://geomaglinux.geofisica.unam.mx/>). We also used the Dst data for GS with $Dst \leq -100$ nT (There are reports of effects on biological systems) from the World Data Center for Geomagnetism Kyoto, (<http://wdc.kugi.kyoto-z.ac.jp/index.html>) for the same time period. We processed 113 976 Kyoto hourly data, and 1,721,820 TEO-H and SYM-H data reported each minute. For SYM-H the data were taken from (http://omniweb.gsfc.nasa.gov/form/omni_min.html).

To calculate the time differences (Δ) between the GS minima reported by the Dst and the TEO-H, we proceeded as follows.

We located the TEO-H data within a window of two days, before and three days after the day of the Dst minimum. We identified 15 GS within this window with $Dst \leq -100$ nT.

They were organized according to the time of occurrence in UT; then TEO-H local time was calculated for each GS (Table 1).

Table 1. The 15 geomagnetic storm with $Dst \leq -100nT$ corresponding to solar cycle 23.

Event	Date	UT hours	TEO MLT hours	Dst minimum nT	Δ minutes	Δ_{SYM-H}
GS 1	04/04/2004	1:00	19:00	-117	-23	-1
GS 2	30/08/2004	23:00	17:00	-129	-25	-3
GS 3	20/11/2003	22:00	16:00	-422	114	-2
GS 4	31/08/2005	20:00	14:00	-122	-122	-153
GS 5	08/05/2005	19:00	13:00	-110	-87	-1
GS 6	18/08/2003	16:00	10:00	-148	-176	-472
GS 7	22/01/2004	14:00	08:00	-130	-385	-636
GS 8	27/07/2004	14:00	08:00	-170	-94	-82
GS 9	30/05/2005	14:00	08:00	-113	-240	-126
GS 10	11/09/2005	11:00	05:00	-139	-179	-215
GS 11	18/06/2003	10:00	04:00	-141	-63	-60
GS 12	18/01/2005	9:00	03:00	-103	52	312
GS 13	15/05/2005	9:00	03:00	-247	14	1
GS 14	08/11/2004	7:00	01:00	-374	116	84
GS 15	12/07/2003	6:00	00:00	-105	234	262

Δ = time difference between the Dst minimum and the TEO-H minimum occurrence; Δ_{SYM-H} = time difference between the SYM-H minimum and the TEO-H minimum occurrence.

Besides, as the other hand, as the geomagnetic index Dst is hourly, it was necessary to carry out an interpolation with resolution of one minute. In order to do this, Hermite interpolating polynomials were used the interpolation was performed based on a group of data pairs $\{(t_1, f(t_1)), (t_2, f(t_2)), \dots, (t_k, f(t_k)), \dots\}$. Two successive values of time t_k differ in one hour, that is $t_{k+1} - t_k = 1h$, where $f(t_k)$ is the data that corresponds to the time t_k . The interpolating polynomial $P_k(t)$ was obtained starting from the points $\{(t_k, f(t_k)), (t_{k+1}, f(t_{k+1}))\}$. These polynomials are built in such a way that the derivative is continuous in the node points $(t_k, f(t_k))$, that is to say, two adjacent interpolating polynomials $P_k(t)$ and $P_{k+1}(t)$ are smoothly united. This limits the function formed by the union of the polynomials $P_k(t)$ in such a way that it does not become too disperse, and allows it to present less variations if the data are not smooth.

Once we located the minimum for each of the obtained functions, related to each GS (using either the Dst_{min} or SYM-H), we calculated Δ and Δ_{SYM-H} according to the following expressions (1a) and (1b):

$$\Delta = Dst_{min} - TEO-H \quad (1a)$$

or

$$\Delta_{SYM-H} = SYM-H - TEO-H \quad (1b)$$

Δ differences are given in minutes.

Results and discussion

In order to distinguish relevant magnetospheric current systems, we have sketched several figures. They represent the Earth from the North Pole; the inner circle represents the universal time (UT) and the outer circle represents the MLT.

Thick lines are at the night side and thin lines at the day side. Regions of currents are: the magnetotail electrojet in the night side, the dawn, the dusk and the day side.

To obtain Δ and Δ_{SYM-H} we compare directly the plots of Dst or SYM-H and TEO-H. According to expressions 1a or 1b, a negative (positive) Δ or Δ_{SYM-H} means that the minimum appears first (afterwards) in the Dst or SYM-H indices (Dst_{min} or $SYM-H_{min}$) and afterwards (first) in

the TEO-H. Figure 2 shows GS 1, GS 2 and 4 to 11, and Table 1 indicates that, for these storms, Δ or Δ_{SYM-H} is negative. Figure 3 shows GS 12 to 15, and Table 1 shows that for these storms Δ is positive. Figure 4 presents GS 3, as Table 1 indicates that it has a positive Δ or Δ_{SYM-H} . In the next section, we will discuss in the next section this storm in particular.

Figures 5, 6 and 7 show the plots of GS 6, 12 and 3 respectively. The GS_6 (Figure 5) is an example of a GS, with negative Δ , and occurred on the 18th of August 2003 with Dst = -148nT. The GS_12 in Figure 6 is an example of a storm with positive Δ , occurred on the 18th of January 2005 with Dst = -103nT. Finally, GS_3 Figure 4 occurred on the 20th of November, 2003 with Dst = -422 nT, being the most intense of the whole sample.

Figure 2 and Table 1 show that all TEO-H minima that occur in the day side, dawn and dusk have a negative Δ (GS 1, GS 2 and 4 to 11), except GS 3, which has positive Δ . Figure 3 shows that all TEO-H minima that occur in the night side have a positive Δ (GS 12 to 15).

From Figure 2, and Δ , we see that when the TEO is under the influence of the ionospheric currents associated to the day side, down

and dusk, the minimum occurs first in the Dst minimum and afterwards in TEO, so Δ is negative. Furthermore, we notice that GS 2, 4, 5 and 6 are influenced by the equatorial electrojet, which is very strong during the daytime [Kalegaev *et al.*, 2008]. Also, in the day side dawn and/or dusk, the GS 7, 8 and 9, occurred at the same time in different dates, that is 14:00UT and in local time at 8:00hrs in the morning. The values of the deltas do not seem to depend on the intensity of the GS expressed in the value of Dst, hence we assume that they are caused by ionospheric currents.

The GS 10 presents a minimum in TEO at 5:00 MLT, then it is under the influence of the dawn current systems. For GS 11 (Figure 2) and 12 (Figure 3), according to Table 1, we notice a change of sign in Δ ; we propose that this happens because they occur in the border of influence of the dawn currents.

These results agree with Li *et al.* (2011), who found that during the ring current injection of a magnetic storm, ions are mostly present in the dusk and pre-midnight sectors of the Earth, because of duskward drifting, producing a highly asymmetric geomagnetic disturbance with MLT.

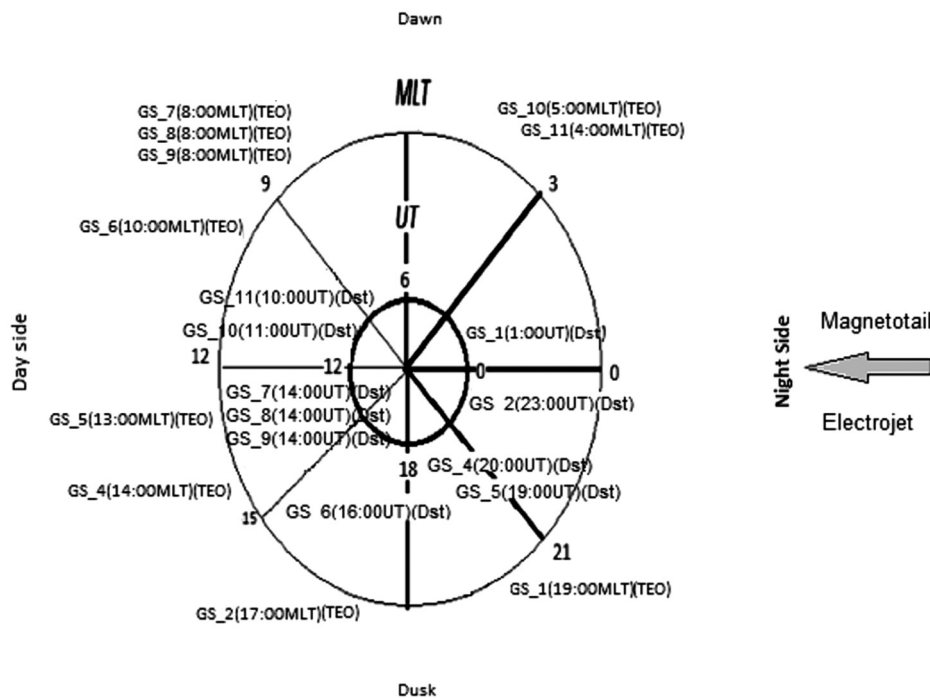


Figure 2. The Earth as seen from the North Pole. The inner circle corresponds to Universal Time (UT) and the outer circle to Magnetic Local Time (MLT). Also are shown the locations of geomagnetic storms (GS) at the moment of occurrence of the storms. The figure shows those GS with negative Δ (GS 1, GS 2 and 4 to 11 according to Table 1).

The GS 12 and 13 have positive Δ and Δ_{SYM-H} (Figure 3 and Table 1), and are located in the zones of the night side current systems. The GS 14 and 15 are located near the magnetotail electrojet zone. In these cases, the electrojet injects directly the ring current when TEO is nearby it, recording first the minimum in TEO-H.

Finally, we noticed that the magnitude of Δ and Δ_{SYM-H} is not related to the GS intensity for all the GS studied except GS 3 (Table 1). Concerning GS 3, we propose that somehow its great intensity ($Dst = -422nT$) would increase the complexity of all the involved phenomena. Also, the difference in Δ would depend on the intensity of the ionospheric currents that are present at the moment of the GS. Then, it seems that these currents would be capable of locally delay or forward the appearance of the minimum in TEO.

According to Cid *et al.*, (2014) GS have a significant local variation, which agrees with GS 14 and 15, that present large Dst minima. However GS_3, having a $Dst = -422nT$, has a very small local variation.

It has been argued that the presences of currents affect the local measurements of the geomagnetic observatories [Shinbori *et al.*, 2012]. Knowing the difference in time for the

occurrence of the minima in Dst and local is important to better quantify the local impacts of GS, that is why a direct correlation between local measurements and Dst should be analyzed.

Conclusions

We analyzed the differences in time (Δ and Δ_{SYM-H}) between the occurrence of the minima in Dst , Δ_{SYM-H} and TEO-H, calculated in UT for 15 GS, $Dst \leq -100nT$, during the descending phase of the solar cycle 23 (January 2003 to December 2006).

We found that when TEO is in the day side, dawn or dusk, the minimum appears first in Dst and afterwards in TEO (negative Δ , Δ_{SYM-H}). However, GS 3 did not follow this behavior, perhaps due to its great intensity; however we cannot explain yet why. We suppose that the day side, dawn and dusk ionospheric currents are the reason of the delay. When TEO is near midnight the minimum is found first in TEO and afterwards in Dst (positive Δ , Δ_{SYM-H}); again we suppose that the magnetotail currents are the cause of this delay.

The differences between Sym-H and Dst , may be because one is an average time and Sym-H is per minute, and that data can come from different observatories.

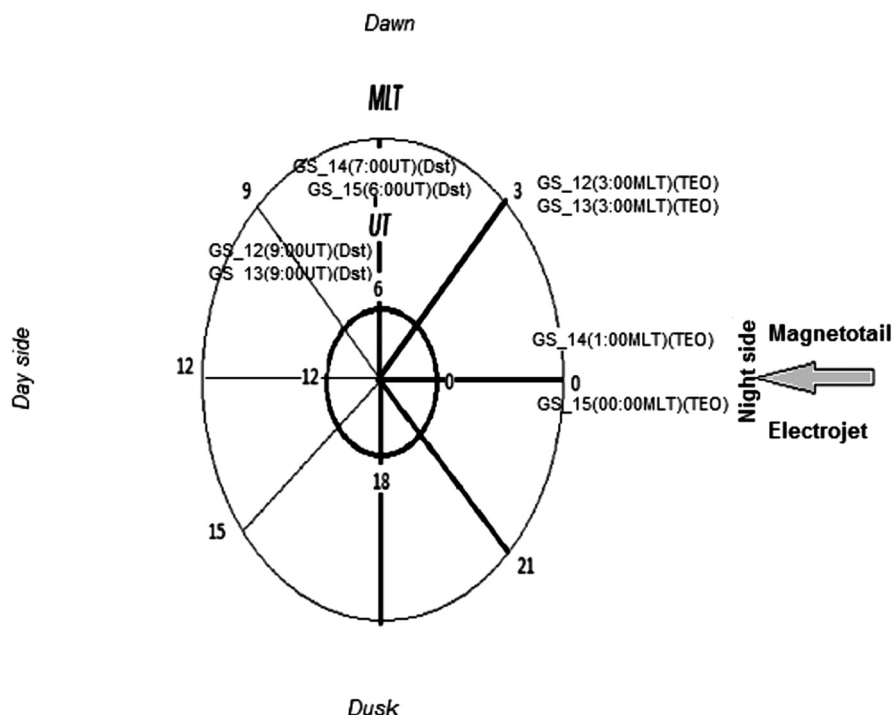


Figure 3. As Figure 2 but showing those GS with positive Δ (GS 12 to 15 according to Table 1).

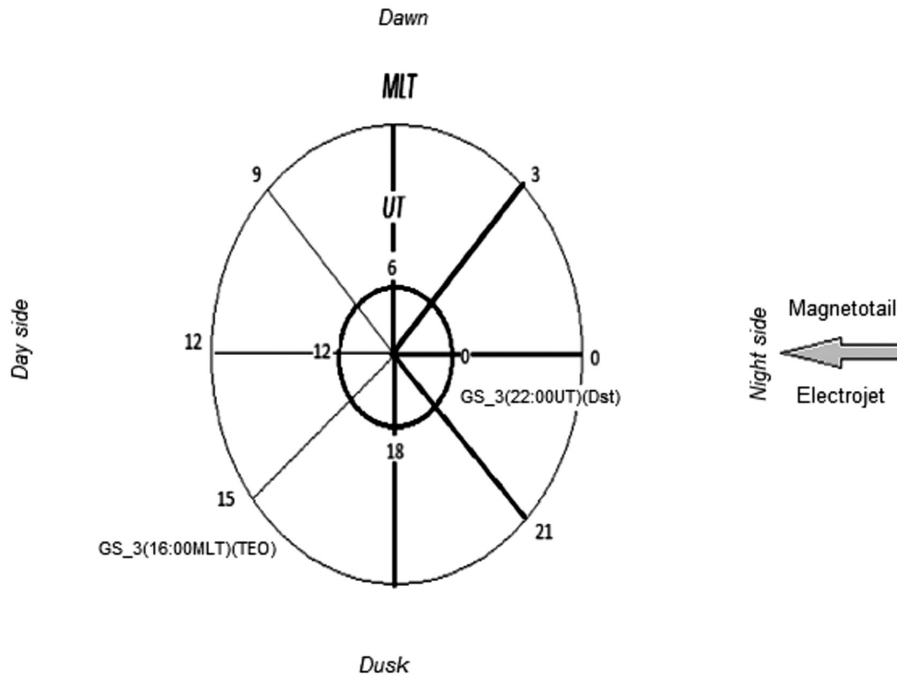


Figure 4. As Figure 2 but showing the location of the GS 3 (according to Table 1) at the moment of occurrence of the storm.

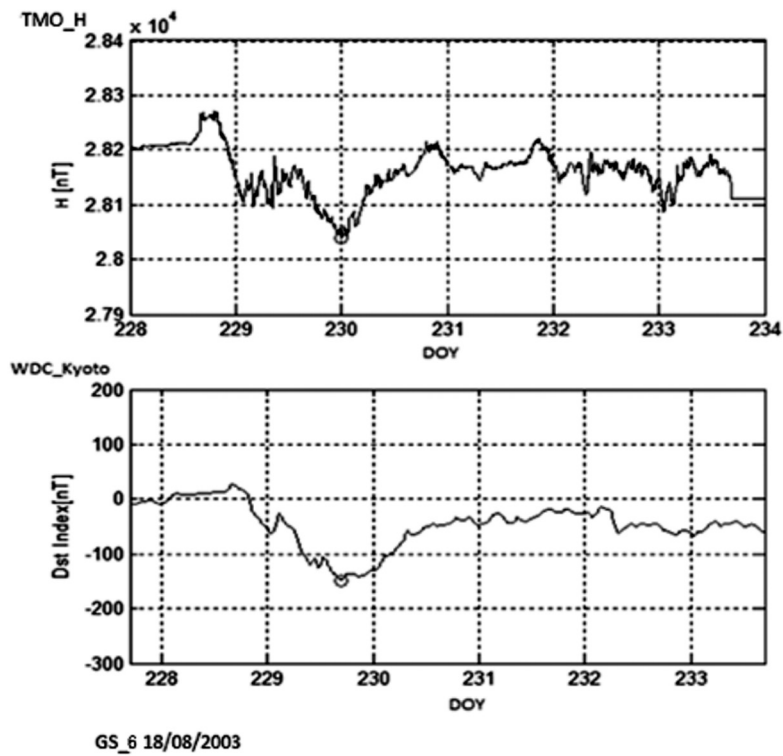


Figure 5. Example of a storm with a negative Δ . GS 6 (see Table 1) shows at the top the TEO-H and at the bottom the Dst. The small empty circle marks the minimum. The minimum presents first in Dst and afterwards in TEO-H.

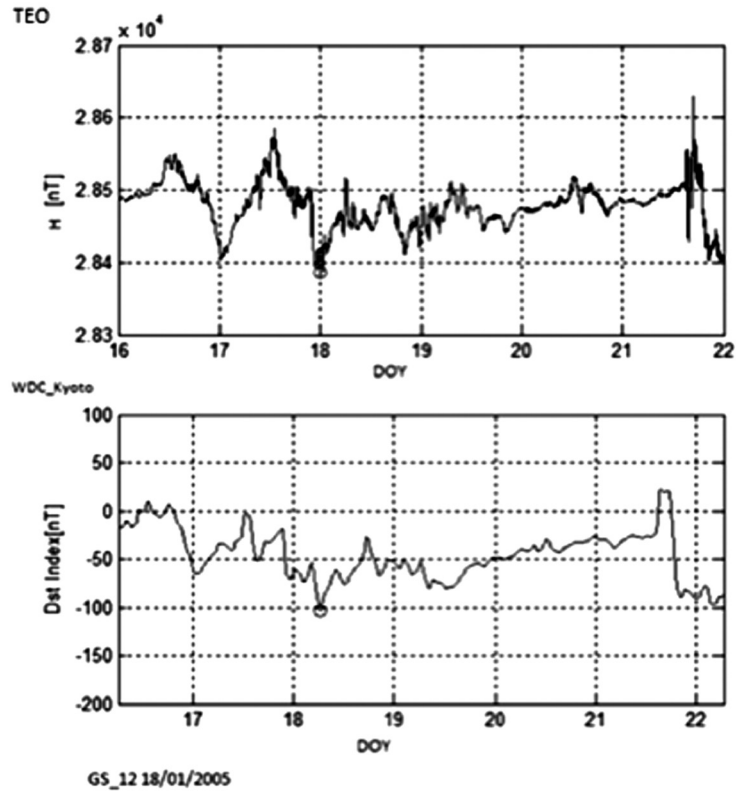


Figure 6. Example of a storm with a positive Δ . GS 12 (see Table 1) shows at the top the TEO-H and at the bottom the Dst. The small empty circle marks the minimum. The minimum presents first in TEO-H and afterwards in Dst.

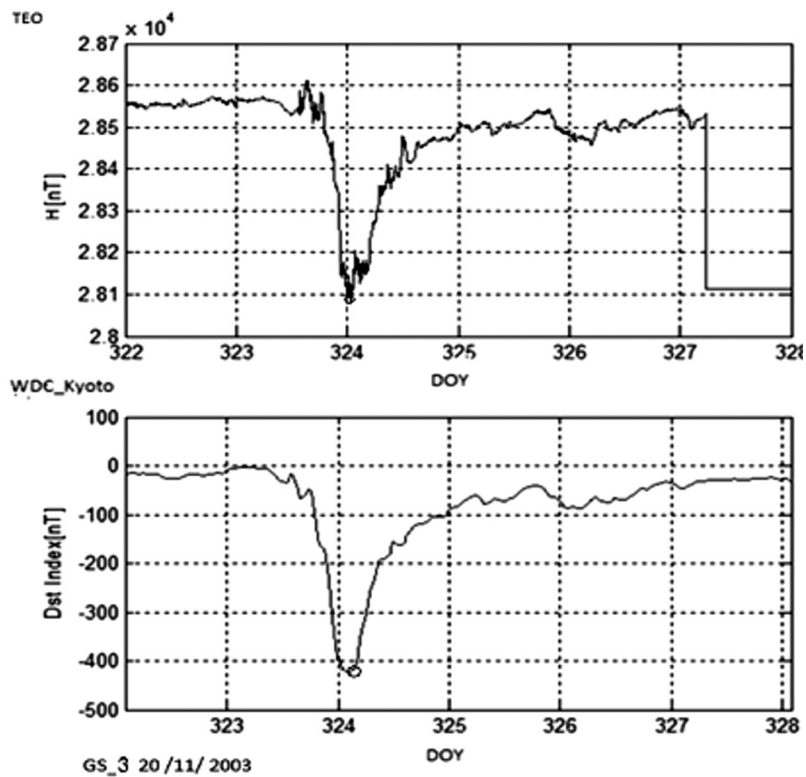


Figure 7. GS 3 (see Table 1) presents a positive Δ . At the top is the TEO-H and at the bottom the Dst. The small empty circle marks the minimum. The minimum presents first in TEO-H and afterwards in Dst. This storm has the largest intensity of the sample (Dst=-422nT).

Acknowledgements

We acknowledge the CONACYT PhD 235167 and PAPIIT-UNAM- IN103415 grants of the Consejo Nacional de Ciencia y Tecnología de México (CONACYT). Finally, we also acknowledge the Kyoto World Data Center, OMNIWeb and the Teoloyucan observatory-UNAM.

References

- Ahn B.H., Moon G.H., Sun W., Akasofu S.I., Chen G.X., Park Y.D., 2002, Universal time variation of the Dst index and the relationship between the cumulative AL and Dst indices during geomagnetic storms. *Journal of Geophysical Research*, 107, doi: 10.1029/2002JA009257.
- Alexeev I.I., Belenkaya E.S., Kalegaev V.V., Feldstein Y.I., Grafe A., 1996, Magnetic storms and magnetotail currents. *Journal of Geophysical Research*, 101, doi: 10.1029/95JA03509.
- Bogdanova Y., Dunlop M., Zhang Q., Perry Ch., Shen Ch., 2014, Ring Current Morphology and Properties: Statistic from Cluster. *Geophysical Research Abstracts*, 16, EGU2014-6591,
- Campbell W.H., 2004, Failure of Dst index field to Represent a Ring Current. *Space Weather*, 2, doi:10.1029/2003SW000041.
- Cid C., Palacios J., Saiz E., Guerrero A., Cerrato Y., 2014, On extreme geomagnetic storms, 4 (A28), doi: 10.1051/swsc/201402.
- Clúa de Gonzalez A.L., González W.D., 2013, Local-time variations of geomagnetic disturbances during intense geomagnetic storms and possible association with their interplanetary causes. *Advances in Space Research*, 51, 1924-1933.
- Daglis I.A., Thorne R.M., Baumjohann W., Orsini S., 1999, The Terrestrial Ring Current: Origin, Formation, and Decay, *Reviews of Geophysics*, 37, 407-438.
- Dessler A.J., Parker E.N., 1959, Hydromagnetic Theory of Geomagnetic Storms, *Journal of Geomagnetic Research*, 64, 12, 2239-2252.
- Hamilton D.C., Gloeckler G., Ipavich F.M., 1988, Ring current development during the great geomagnetic storms of February 1986, *Journal of Geophysical Research*, 93(A12), 14343-14355.
- Kalegaev V.V., Bakhmina K.Y., Alexeev I.I., Belenkaya E.S., Feldstein Y.I., Ganuskina N. V., 2008, Ring Current Asymmetry during a Magnetic Storm, *Geomagnetism and Aeronomy*, 48, 6, 747-758.
- Katus R.M., Liemohn M.W., 2013, Similarities and differences in low-latitude to middle-latitudes geomagnetic indices, *Journal of Geophysical Research Space Physics*, 118, 5149-5156, doi: 10.1002/jgra.50501.
- Keika K.L., Kistler L.M., Brandt P.C., 2013, Energization of O⁺ ions in the Earth's inner magnetosphere and the effects on ring current buildup: A review of previous observations and possible mechanisms, *Journal of Geophysical Research. Space Physics*, 118, 7, 4441-4464, doi:10.1002/jgra.50371.
- Le G., 2013, Magnetic Field Observations of the Ring Current in the inner Magnetosphere and Ionosphere. *American Geophysical Union, Spring Meeting*, abstract SM33A-01.
- Li H., Wong C., Kan J.R., 2011, Contribution of the partial ring current to the SYMH index during magnetic storms, *Journal of Geophysical Research*, 116(A11222), doi: 10.1029/2011JA016886,
- Liu S., Chen M.W., Roeder J.L., Lyons L.R., Schulz M., 2005, Relative contribution of electrons to the storm time total ring current energy content, *Geophysical Research Letters*, 32, L03110, doi: 10.1029/2004GL021672.
- Lockwood M., 2013, Reconstruction and Prediction of Variations in the Open Solar Magnetic Flux and Interplanetary Conditions, *Living Rev. Solar Phys.*, 10, 4, doi: 10.12942/lrsp-2013-4, <http://www.livingreviews.org/lrsp-2013-4>
- Mandea M., Korte M., 2011, Geomagnetic Observations and Models IAGA Special Sopron Book Series 5, Editores Université Paris.
- Mayaud P.N., 1980, Derivation Meaning, and Use of Geomagnetic Indices, *Geophys. Monogr. Ser. AGU*, Washington, D.C., 22, 154, doi: 10.1029/GM022.
- Patra S., Spencer E., Horton W., Sojka J., 2011, Study of Dst/ring current recovery times using the WINDMI model. *Journal of Geophysical Research*, 116(A02212), doi:10.1029/2010JA015824.

Shinbori A., Tsuji Y., Kikuchi T., Araki T., Ikeda A., Uozumi T., Baishev D., Shevtsov B.M., Nagatsma T., Yumoto K., 2012, Magnetic local time and latitude dependence of amplitude of the main impulse (MI) of geomagnetic sudden commencements and its seasonal variation, *Journal Geomagnetic Research*, 117(A08322), doi:10.1029/2012JA018006.

Sugiura M., 1964, Hourly values of equatorial Dst for the IGY, *Ann. Int. Geophys.* 35, 9-45.

Sugiura M., Poros D.J., 1971, Hourly values of equatorial Dst for the years 1957 to 197. Goddard Space Flight Center, Greenbelt, Md. , GSFC Doc. X-645-71-278.

Tsurutani B.T., Verkhoglyadova O.P., Mannuci A.J., Lakhina G.S., Huba J.D., 2012, Extreme changes in the dayside ionosphere during a Carrington-type magnetic storm, *J. Space Weather Space Clim.*, 2 (A05), doi: 10.1051/swsc/2012004.

Welling D.T., Jordanova V.F., Zaharia G., 2011, The effects of dynamic ionospheric outflow on the ring current. *Journal of Geophysical Research*, 116(A00J19), doi: 10.1029/2010JA0115642.